THE CELL: STRONG, SOFT MATTER

Yuval Mulla

This thesis was reviewed by:

Prof. dr. J. van der Gucht	Wageningen Universiteit
Dr. W.G. Ellenbroek	Technische Universiteit Eindhoven
Prof. dr. R.P. Sijbesema	Technische Universiteit Eindhoven
Prof. dr. G. Wuite	Vrije Universiteit
Prof. dr. B. Fabry	University of Erlangen-Nuremberg

The work described in this thesis was performed at AMOLF, Science Park 104, 1098 XG Amsterdam, The Netherlands. This work is part of the research program of the Netherlands Organisation for Scientific Research (NWO). We gratefully acknowledge financial support from an ERC Starting Grant (335672-MINICELL).

Cover design Ricardo Struik
Printed by Ipskamp, Amsterdam, The Netherlands

MIX
Paper from
responsible sources
FSC® C128610
FSC
www.fsc.org

ISBN 978-94-92323-23-1

A digital version of this thesis can be obtained from `http://www.amolf.nl` and from `www.ub.vu.nl`. Printed copies can be obtained by request via `library@amolf.nl`.

VRIJE UNIVERSITEIT

THE CELL: STRONG, SOFT MATTER

ACADEMISCH PROEFSCHRIFT

ter verkrijging van de graad Doctor
aan de Vrije Universiteit Amsterdam,
op gezag van de rector magnificus
prof.dr. V. Subramaniam,
in het openbaar te verdedigen
ten overstaan van de promotiecommissie
van de Faculteit der Bètawetenschappen
op vrijdag 8 februari 2019 om 9.45 uur
in de aula van de universiteit,
De Boelelaan 1105.

door

Yuval Mulla

geboren te Kfar Saba, Israël.

promotor:	prof.dr. G.H. Koenderink

I have never tried, so I think I should definitely be able to do it.

Pippi Longstocking

CONTENTS

1

INTRODUCTION

1.1. DEFORMABILITY AND STRENGTH OF CELLS

Cells in our body are deformable, as can be seen when they are subject to external forces and when they actively deform themselves [1]. For example, immune cells and metastatic cancer cells migrate through dense extracellular matrices [2]. On the length scale of a cell, the extracellular matrix is highly non-uniform [3]. Cellular migration therefore requires continuous shape adaptation [4]. Similarly, the cell shape changes dramatically during division [5] and differentiation [6]. Clearly, cells are highly deformable.

The same cell has a very stressful life mechanically. For example, the cell is under continuous osmotic pressure created by the large concentration of biomolecules inside [7]. Furthermore, large forces are exerted on cells and their surrounding tissues, for example during embryonic development [8] or in cartilage during the movement of joints [9]. The high forces exerted on cells can cause fracturing of the cytoskeleton, for example when exposed to large hydraulic pressure during epithelial stretching [10]. Furthermore the speed of cell migration in extracellular matrices is compromised as high stress rate triggers fracturing of the cytoskeleton [11]. Mechanical failure of cells is known to cause developmental defects in fly embryos [12] and can lead to pathologies such as the kidney disease FSGS1 [13]. Therefore, apart from being highly deformable, a cell also needs to be strong [1].

Typically, materials are either deformable or strong [19]. For example, a pudding is readily deformable but can easily be broken by hand, whereas the opposite is for a brick which has a high rupture force, but still breaks at small deformations due to its high stiffness. In contrast to these synthetic materials, a cell combines strength with deformability. Which material design principles allow the cell to meet these seemingly

---

[1] For completeness, we should mention that there are exceptions to this rule. Fracturing of cytoskeletal networks can also have a beneficial role, for example in cell polarization [14–16], during cell division [17], and in bleb formation during migration [18]. In any case, the strength of cytoskeletal networks needs to be tightly controlled.

contradictory demands? Answering this question will not only increase our understanding of biology, but can also inspire the design of new synthetic materials and possibly give insight into diseases where the mechanical properties of a cell are compromised.

1.2. CYTOSKELETON

The mechanical properties of an animal cell arise from interactions between the cell's plasma membrane and the cytoskeleton, a composite dynamic biopolymer network comprising three interconnected subsystems: filamentous (F-) actin, microtubules, and intermediate filaments (IFs). Furthermore, the cytoskeleton consists of accessory proteins such as crosslinks and molecular motors that walk along filaments to transport cargo or connect pairs of filaments and slide them [20]. These three biopolymers each have their own characteristic mechanical properties and are able to interact with each other and with the plasma membrane to define the cell's mechanical properties and shape (figure 1.1).

1.2.1. ACTIN

Actin networks are the focus of this PhD thesis as actin is the main cytoskeletal player in cell shape processes like (de-)adhesion [22], resisting osmotic pressure [23] and force production during division [24] and migration [25]. Actin is typically the most abundant protein in vertebrate cells, accounting for $1-5\%$ of the total cytosolic protein mass in most cell types and an astonishing 22% in muscle cells [26]. Furthermore, actin is one of the most highly conserved proteins: even species as diverse as cows and slime molds differ less than 2% in their amino acid sequence [27].

The high degree of conservation combined with the high expression levels suggest exceptional functionality for actin cortices. Indeed the actin cortex meet the seemingly contradictory demands of resisting mechanical stresses, yet allowing for large deformations. The actin cortex has to withstand tensile, compressive, shear and hydrostatic loads, depending on the tissue type. For example, endothelial cells in blood vessels are stretched and exposed to shear flow [28], whereas cells in cartilage are subject to compresive and hydrostatic loads [9]. The actin cytoskeleton plays a key role in bearing such mechanical load, but also is able to undergo large deformations without fracturing during e.g. cell division and migration. What makes the actin cytoskeleton strong and deformable at the same time? In order to be able to address this question, we first review the structure and dynamics of actin cortices on different length scales.

ACTIN MONOMERS

An actin monomers is a 42-kDa globular protein with a diameter of approximately $5\,nm$. The crystal structure of actin reveals a barbed (+) and pointed (-) end, connected by an ATPase domain [29]. The pointed end contains a cleft which can either be in a closed or open conformation. Close to the ATPase domain there is a divalent cation binding site which controls whether the cleft is closed or open. The ATPase domain is, as the name suggests, capable of hydrolyzing ATP into ADP, which is used to fuel reactions as explained below.

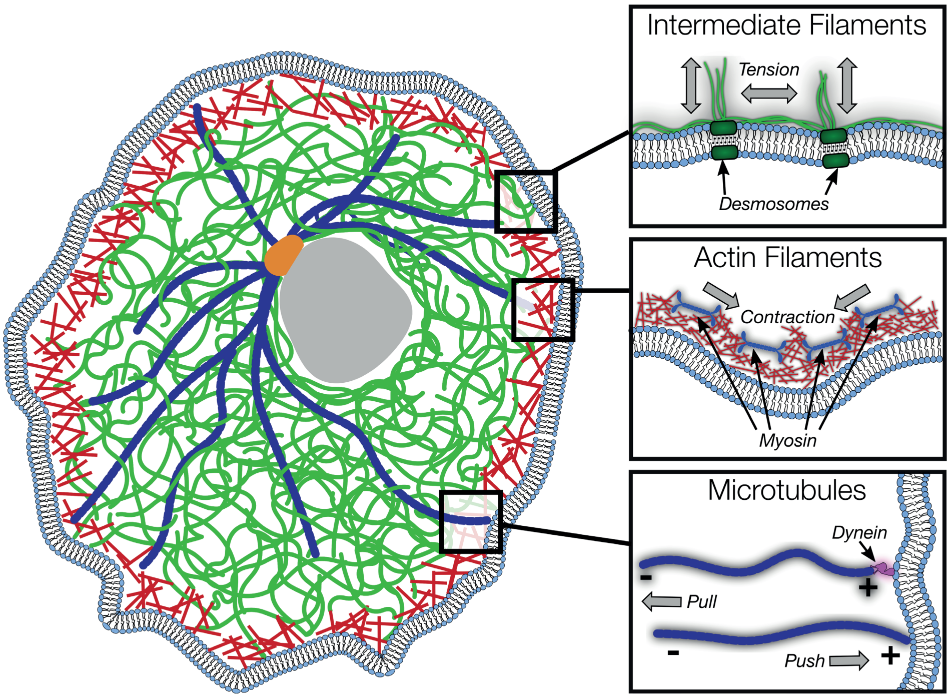

Figure 1.1: Schematic of the cytoskeletal organization of an interphase cell adhered to an underlying substrate. Intermediate filaments (green) form a dense network that provides mechanical resistance against large deformations and connects the cell nucleus to the cell periphery. The actin cortex (red) is anchored to the membrane by numerous interactions such as the ERM (Ezrin, Radixin and Moesin) family of proteins, which is mediated by anionic lipids. Active contraction is caused by filament sliding, driven by myosin motor proteins, thus regulating cell surface stiffness and creating high hydrostatic pressure inside the cell. Microtubules (blue) exert pushing and pulling forces on the cell membrane, crucial for separating the chromosomes during cell division, which is driven by polymerization, depolymerization and motor proteins such as dynein which induce sliding forces and act as membrane anchors. The schematic is drawn by Anders Aufderhorst and reproduced from Ref. [21].

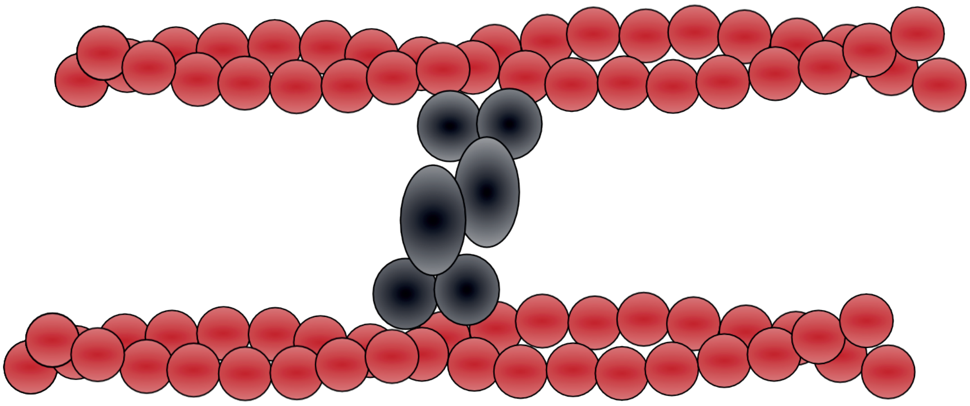

Figure 1.2: Schematic of two actin filaments (red) crosslinked by an actin crosslinker (grey). The schematic is drawn by Anders Aufderhorst.

ACTIN FILAMENTS

After bonding with divalent ions, actin monomers can polymerize into double-stranded, helical actin filaments [30]. The actin monomers stack with the barbed ends to the pointed ends, causing polarity in the actin filaments. The monomer binding and unbinding rate are faster on the barbed end than on the pointed end. However, detailed balance requires that the equilibrium constants are identical on both ends, meaning that net growth of one filament end necessitates growing of the filament on the other end as well. Interestingly, the polymerization equilibrium constant of ATP-actin is higher than of ADP-actin [31]. This difference in equilibrium constant allows cells to break detailed balance and have treadmilling filaments which polymerize on one end and depolymerize on the other: due to the higher growth rate, filaments incorporate ATP-actin predominantly at the barbed end [32]. In the filament, monomers hydrolyse ATP and thereby decrease the equilibrium constant. As a result, filaments depolymerize on their pointed ends (which predominantly consist of ’old’, ADP-bound actin monomers) whilst polymerizing on the barbed end (which predominantly consist of ’fresh’, ATP-bound actin). In the cytosol, ADP is actively regenerated back into ATP.

Apart from an energy consuming ATP regeneration system, actin treadmilling also requires a range of actin binding proteins to prevent ADP-actin filament formation. Firstly, spontaneous nucleation of (both ADP- and ATP-) actin filaments is suppressed by profilin, a protein that sequesters actin filaments. With spontaneous nucleation suppressed, actin filaments exclusively polymerize from either ARP2/3 or formins, proteins which respectively branch or nucleate actin filaments and typically reside close to the plasma membrane [30]. Furthermore, actin filaments are continuously broken down by the actin depolymerizing and severing protein cofilin [31]. Together, these actin polymerizing and depolymerizing proteins cause filament treadmilling, which is a source of force production that facilitates the formation of membrane protrusions or invaginations [31]. In the absence of profilin, cofilin, formin and/or ARP2/3, actin filaments can spontaneously nucleate and grow, but do not depolymerize on timescales discussed within this thesis.

Actin filaments are semiflexible, which means that, unlike stiff rods, they significantly bend due to thermal fluctuations, but not to the extent that they coil up like fully flexible filaments. More formally, filament stiffness can be characterized by the persistence length, the length scale at which correlations in the direction of the tangent are lost due to thermal bending fluctuations. Actin filaments have a persistence length of about $10\,\mu m$ [30], which is roughly the length of reconstituted actin filaments under typical experimental conditions [33], about an order of magnitude longer than typical actin filaments in the actin cortex of live cells [34] and 1-2 orders of magnitude longer than typical mesh sizes of both reconstituted [35] and in vivo actin cortices [34].

HIGHER ORDER ACTIN STRUCTURES

Actin filaments form multiple types of structures depending on the cell type. For example, actin filaments bundle into stress fibers in adherent cells and in protrusions such as filopodia and stereocilia. Furthermore, crosslinked actin forms a filamentous cortex close to the plasma membrane that is able to exert contractile forces on the membrane through the action of myosin motor proteins that pull on the actin filaments [36]. Actin networks and bundles are crosslinked by a wide range of actin binding proteins such as filamin, alpha-actinin, fascin, and fimbrin [30]. Typically, these proteins reversibly crosslink two actin filaments, with a typical crosslinking lifetime of a few seconds [37, 38]. These crosslinker dynamics uniquely confer mechanical resistance on short timescales with the ability to flow on timescales longer than the crosslinker lifetime [37]. Myosins are a special type of actin binding protein, as myosin hydrolyses ATP in order to slide actin filaments [36]. Myosins are called molecular motors as they convert chemical into mechanical energy [36]. This active sliding is, together with active polymerization/depolymerization [31], the source of force production by the actin cortex of the cell [36].

1.2.2. MICROTUBULES AND INTERMEDIATE FILAMENTS

Whilst the focus of this work is on the actin cytoskeleton, we should briefly mention the two other cytoskeletal biopolymers: microtubules and intermediate filaments. Microtubules have a persistence length on the order of several millimeters, which is much longer than the diameter of cells (typically $5-50\,\mu m$ depending on the cell type) [39]. These highly rigid filaments exert forces active polymerization and de-polymerization triggered by dynamics instabilities [40] and through motor-driven sliding [41]. These forces are the main driver for establishing cell polarity and separating the chromosomes in dividing cells.

Intermediate filaments are softer than actin filaments and microtubules, with a persistence length of about a micrometer [39]. These flexible filaments form dense networks between the cell nucleus and the membrane with much slower turnover rates [42]. They serve a vital scaffolding role by providing resilience against large deformations, a phenomenon facilitated by their ability to withstand high tensile strains [43, 44].

1.3. RECONSTITUTED ACTIN NETWORK MECHANICS

Clearly, the actin cortex has unique microscopic properties which lead to interesting mechanics. However, it is difficult to understand the mechanical properties of actin cortices from experiments on live cells as actin cortices are tightly regulated biochemically [45]. Furthermore, the actin cortex is strongly coupled to the plasma membrane and to the other two cytoskeletal subsystems, microtubules and intermediate filaments [20, 21]. All filamentous systems are able to tether to the membrane [46] and interact with each other both through physical interactions mediated by crosslinkers and motors and through joint biochemical regulation [20]. To dissect the contribution of the actin cortex, we utilize a so-called 'bottom-up' approach to elucidate the complex mechanics of actin cortices. In this approach, actin is purified and studied in isolation or together with a limited set of actin binding proteins in order to, step-by-step, build up understanding of how the actin cortex controls cell shape and mechanics [21]. This approach has proven highly successful: for example, polymerizing an actin cortex on spherical beads has given insight into how stress release drives symmetry breaking for actin-based movement [47], and encapsulating actomyosin networks inside spherical membranes has revealed how cortical tension drives shape change [15].

1.4. STATE OF THE ART

We are interested in how actin networks combine the ability to withstand mechanical stresses with a high degree of deformability without fracturing. Gaining insight into the mechanics of actin networks is non-trivial due to their complex dynamics. Most materials are either solids, like rubber and iron, or liquids such as water and oil. Solids deform elastically, which means that the force required for a deformation is proportional to the amount of deformation. In contrast, liquids deform viscously, which means that the force required for a deformation is proportional to the *rate* of deformation. However, actin networks are somewhere in between the two extreme cases of solids and liquids, and instead deform viscoelastically upon mechanical perturbation. Furthermore, rheological experiments on actin networks have revealed multiple sources of nonlinearity, depending on the duration and amplitude of the applied stress.

1.4.1. ACTIN RHEOLOGY

When actin filaments are reconstituted at sufficiently high concentrations, such that the filaments sterically interact, a network is obtained with a non-zero storage modulus [48]. This storage modulus increases with the concentration of actin, and is significantly higher than that of flexible polymers at the same volume fraction. The relatively high stiffness of actin networks is attributed to the semiflexible backbone of the polymer [48]. Whereas entangled actin networks are relatively weak and can sustain little stress [49], actin filaments crosslinked by actin binding proteins are significantly stronger [50]. Furthermore, such networks have a highly nonlinear elastic response, in which the shear rigidity can increase by orders of magnitude when deformed by only a few percent [51]. For permanently cross-linked semi-flexible polymer networks, this is well accounted for by the compliance due to transverse bending fluctuations that become suppressed under a load [48, 50].

Transient linking maintains mechanical rigidity whilst allowing for the cytoskeleton to remodel over time [37]. The resulting viscoelastic flow follows power law dynamics beyond the typical crosslinker unbinding time [37, 52]. The crosslinker unbinding time depends on the applied stress as force-induced unbinding of the transient linkers reduces the typical crosslinker lifetime [53–55]. Perhaps surprisingly, an increase of the typical relaxation time of actin networks upon force also has been observed for certain types of actin cross linkers [56, 57], suggesting force-induced binding. Indeed, single molecule force spectroscopy has shown that certain types of actin binding proteins increase their bound lifetime upon force [58, 59], a process known as catch bonding.

All above-mentioned work has focused on isotropically crosslinked actin networks. However, for high degrees of crosslinking and/or molecular crowding, the actin filaments organize into bundles [60]. When an extensile force is exerted on a single bundle, the bundle extends due to filament-filament sliding [61]. However, once the force is released, the bundle contracts to maximize filament-filament overlap. For networks of bundles, the application of shear stress can lead to formation of new contacts between bundles [62]. As the macroscopic stress is relaxed, these newly made contacts lead to internal stress [63] and thereby stiffen the network [62].

The active processes in the actin cortex, namely actin treadmilling and the processive movement of myosin motors, affect the cortex mechanics in various ways. A recent pioneering work has measured the rheological properties of a network of treadmilling filaments and has found that this form of activity greatly speeds up stress relaxation [64]. Similarly, myosin motors fluidize uncrosslinked networks via filament-filament sliding [65]. In contrast, crosslinked actin networks stiffen due to internal stresses, as myosin motors cause contractile forces. How motor-induced filament sliding leads to actomyosin contractility is not obvious a priori as filaments can either slide away or towards each other, enabling both resp. extension and contraction. The microscopic origins of symmetry breaking between expansive and contractile contributions are reviewed in detail elsewhere [36]. Briefly, possible microscopic origins for macroscopic contractility include sliding-induced buckling [66], tension in myosin minifilaments [67] and myosin motors residing on filament ends [68, 69].

1.4.2. THEORETICAL MODELS

The rich mechanics of actin networks has prompted the development of a range of complementary theoretical approaches. Earlier models of semiflexible polymer networks have focused on the limit of permanently crosslinked networks and, more recently, phenomenological and microscopic models have been developed to understand the importance of transient crosslinking. In the limit of permanently crosslinked networks, the elasticity of semiflexible polymer networks depends on the degree of thermal fluctuations in the filament [48]. For small stresses, this elasticity is constant and depends on the crosslinker distance which confines filament fluctuations [48]. For larger stresses, individual filaments are pulled taut, reducing transverse filament fluctuations [51]. On a single filament level, the worm-like chain model predicts the length scale beyond which fluctuations get suppressed. Using mean field arguments, this length scale can then be used to predict the nonlinear elasticity of semiflexible polymers [50]. The mean field model has also been extended to address the effect of stretchable filaments [50, 70], which is particularly relevant for intermediate filaments [71].

The effect of transient crosslinking adds significant complexity to the mechanical properties of semiflexible polymer networks. Whereas time-dependent mechanics of transiently crosslinked *flexible* polymer networks are well-described by a simple Maxwell model with only a single timescale [72], the cytoskeleton exhibits power law behavior [73–79]. To explain this behavior, the so-called glassy worm-like chain model has been developed [76]. This model is inspired by the framework of soft glassy rheology, which explains power law dynamics in materials close to the glass transition [80]. In the glassy worm-like chain framework, fluctuations of biopolymers are slowed by a complex environment with a broad distribution of relaxation times. Due to this complex environment, the relaxation spectrum of the wormlike chain follows a stretched exponent [76]. Whilst this phenomenological model can reproduce the power law dynamics as observed in mechanical measurements on cells [73–79], the microscopic interpretation of this complex environment, and therefore of the glassy dynamics, remains unclear.

A more microscopic model for transiently connected semiflexible polymer networks has also been developed on basis of the crosslinker dynamics [37]. This dynamics model describes the structural relaxation of semiflexible filaments that results from many independent unbinding or rebinding events . For timescales longer than the crosslinker unbinding rate, power-law rheology arises from a broad spectrum of relaxation rates. Specifically, a universal $\omega^{1/2}$ power law was predicted for the storage and loss moduli of transiently crosslinked semiflexible filaments [37] - as has indeed been observed experimentally [37, 52, 57].

1.5. KEY OPEN QUESTIONS

- **Which timescale sets the power law dynamics of transiently connected actin networks?** The crosslink-governed dynamics model predicts that actin networks only exhibit power law dynamics beyond the timescale of crosslinker unbinding. However, direct verification of this claim is lacking. Intriguingly, timescale as extracted from rheology [37, 81] is more than an order of magnitude faster than the crosslinker remodeling timescale as measured by fluorescent recovery after photobleaching on the same crosslinker [38, 82–84] - suggesting significantly more complex dynamics than assumed so far [37, 85].

- **Why do actin cortices exhibit more glassy dynamics than reconstituted actin networks?** The cross-link governed dynamics model predicts a universal $\omega^{1/2}$ power law dependence of the storage and loss moduli of transiently crosslinked semiflexible filaments [37]. However, the cell cortex exhibits glassy dynamics with significantly smaller exponents [73] than the $\omega^{1/2}$ power law as predicted [37] and measured [52, 81] for reconstituted actin networks. The microscopic origin of this discrepancy remains unclear.

- **What determines the strength of transiently connected semiflexible polymer networks?** Whereas the viscoelasticity of actin networks is intensively investigated, it is entirely unclear what determines the strength of these networks. Experiments on reconstituted cytoskeletal networks have shown that the network strength depends on the filament length [86] and on the crosslinker length [87], crosslinker density [35] and crosslinker flexibility [88]. However, these results are rather anecdotal as no models with any predictive power exist on what governs crack initiation in transient networks. As a result, design strategies which improve network strength remain largely obscured.

1.6. THESIS GOAL AND OUTLINE

The overarching goal of this thesis is to understand how the actin cortex allows cells to be soft yet strong. To this end, we perform experiments on reconstituted actin networks and develop new theoretical models to understand the nonlinear dynamics and fracturing behavior of these networks.

In chapter 2 we investigate in detail the linker dynamics through a combination of theoretical modeling and several experimental techniques. We find that stress relaxation in an actin network occurs on a faster timescale than crosslinker redistribution. We rationalize this discrepancy, using a three-state model where crosslinkers are either bound to 0, 1 or 2 filaments. In this model, stress relaxation occurs as soon as a a doubly bound crosslinker unbinds one of two filament, whereas crosslinker redistribution requires unbinding from both filaments. Surprisingly, we find that the unbinding rate of a singly bound crosslinker is more than an order of magnitude slower than when two filaments are attached. We attribute the increased unbinding rate of doubly bound crosslinkers to the stiff nature of biopolymers which frustrates crosslinkers bound to two filaments. This chapter provides quantitative insight into the crosslinker dynamics in biopolymer networks.

In chapter 3 we examine how the linker dynamics affect the nonlinear mechanical properties of dynamically crosslinked actin networks. We find unexpectedly slow stress relaxation, similar to disordered systems close to the glass transition. We explain our experimental results using a theoretical model that the transient nature of the crosslinkers with the nonlinear force-extension behavior of the actin filaments. This chapter offers a microscopic mechanism for the universal glassy dynamics as frequently observed in cellular mechanics

In **chapters 4 & 5** we propose a theoretical model that describes how fracturing occurs in transient networks such as the actin network. In chapter 3, we use stochastic modeling to investigate a collection of reversible bonds under load, and find a microscopic mechanism by which cracks emerge from the nonlinear local bond dynamics. We provide and numerically verify analytical equations for the dependence of the critical crack length on the bond kinetics and applied stress. In chapter 4, we extend the stochastic model to consider the effect of bond mobility after unbinding on the strength of a transient network. We find that bond mobility weakens the strength of transient networks. This is remarkable as bond mobility is common in biological transient networks such as the actin cortex, and in systems responsible for cellular adhesion. These chapters reveal governing principles of the fracturing of transient networks such as the actin cortex.

In **chapter 6** we study the effect of catch bonding on network strength. Catch bonds are proteins whose bond lifetime increases when moderate forces are applied via exposure of hidden binding sites. After full exposure at high force, catch bonds behave like normal (slip) bonds whose bond lifetime monotonically decreases with force. Using the stochastic model developed in chapter 3 & 4, we show that catch bonds provide vastly more long-lived networks than slip bonds. Surprisingly, we find that catch bond networks are stronger than slip bond networks even when the individual bonds are weaker. We verify our conclusion experimentally by combining single molecule and network experiments on actin crosslinked by either wild type α-actinin 4 or a K255E mutant. We attribute the increased strength of catch bond networks to a self-assembly mechanism against force inhomogeneity, which requires bond mobility. This chapter reveals the importance of catch bonds in preventing fracturing in highly deformable transient networks such as the actin cortex.

In the **Outlook** we create a model cell system of an actin cortex transiently connected to and confined by a spherical, cell-sized lipid membrane and develop mechanical tools to mechanically investigate these minimal cells. This outlook provides an important step in bridging the gap between rheology on simplified reconstituted networks and cellular mechanics.

2

FRUSTRATED BINDING OF BIOPOLYMER CROSSLINKERS

Transiently crosslinked actin filament networks allow cells to combine elastic rigidity with the ability to deform viscoelastically. Theoretical models of semiflexible polymer networks predict that the crosslinker unbinding rate governs the timescale beyond which viscoelastic flow occurs. However a direct comparison between network and crosslinker dynamics is lacking. Here we measure the network's stress relaxation timescale using rheology and the lifetime of bound crosslinkers using fluorescence recovery after photobleaching. Intriguingly, we find that the crosslinker unbinding rate measured by FRAP is more than an order of magnitude slower than the rate measured by rheology. We rationalize this difference with a three-state model where crosslinkers are bound to either 0, 1 or 2 filaments, and we extract crosslinker transition rates that are otherwise difficult to access. Interestingly, we find that the unbinding rate of singly bound crosslinker is nearly two orders of magnitude slower than when two filaments are attached. We attribute the increased unbinding rate of doubly bound crosslinkers to the stiff nature of biopolymers, which frustrates crosslinkers bound to two filaments.

2.1. INTRODUCTION

Cell shape and mechanics are largely governed by the actin cortex, a thin biopolymer meshwork underneath the cell membrane. The actin cortex needs to be readily deformable for processes like division and migration [4]. However the same material should resist mechanical stresses to protect the cell nucleus and plasma membrane against external stresses [11, 23]. This extraordinary combination of deformability and mechanical resistance is achieved by dynamic crosslinking proteins which stochastically bind and unbind actin filaments [32]. This design principle yields mechanical resistance as the bonds form a percolated network, whilst allowing for viscoelastic flows on timescales longer than the crosslinker unbinding timescale as the network remodels via the linker dynamics.

Rheological measurements on reconstituted actin filaments together with actin crosslinking proteins have shown that the microscopic crosslinker dynamics determine the macroscopic network mechanics [56, 89–91] and mutations affecting single molecule crosslinker dynamics also change the network mechanics [55, 81, 92]. Different from most synthetic polymers, which are flexible and coil up due to thermal fluctuations, actin filaments are semiflexible polymers with a persistence length close to 10 μm, on the order of the filament length [93]. The elasticity of semiflexible polymer networks is inversely proportional to the length scale of transverse filament fluctuations. Crosslinkers confine such fluctuations and thereby increase network stiffness of semiflexible polymer networks [48].

Whereas time-dependent mechanics of transiently crosslinked *flexible* polymer networks are well-described by a simple Maxwell model with a single stress relaxation rate [72], measurements on reconstituted actin networks [52, 81] and on living cells [73, 94, 95] have revealed power law dynamics in the storage and loss modulus as a function of frequency. Theoretical modeling [37] and simulations [85] have revealed that these power law dynamics result from the superposition of multiple relaxation times of the many cross linkers on a distance shorter than the persistence length that crosslink a single filament to the surrounding network [37, 85].

Current models predict that this regime characterized by power-law dynamics occurs on timescales longer than the crosslinker unbinding time [37, 85]. Previous studies have used the onset frequency of power law dynamics to characterize the actin crosslinker α-actinin 4 (ACTN4) via rheological measurements and have found a crosslinker unbinding timescale on the order of 2 s [37, 81, 96]. In contrast, direct measurements of the ACTN4 binding kinetics within actin networks using Fluorescence Recovery After Photobleaching (FRAP) have found a typical unbinding time of $30-100$ s [38, 82–84]. Although it should be noted that these experiments have been performed under different conditions (reconstituted actin networks [37, 81] versus live cells [38, 82–84]) the difference of more than an order of magnitude between the two measurements [37, 38, 81–84] suggests significantly more complex dynamics than assumed so far [37, 85].

Here we perform both FRAP and rheology experiments on reconstituted actin networks crosslinked by ACTN4. We find that the crosslinker unbinding rate measured by FRAP is an order of magnitude slower than the onset frequency of power law dynamics in the rheology even when measured on identical samples. We rationalize this difference with a three-state crosslinker model. We are able to extract quantitative information on the crosslinker (un)binding kinetics which is only accessible through a combination of techniques, and has not been reported before. Interestingly, we have found that the unbinding rate of a crosslinker attached to one filament is more than an order of magnitude slower than when two filaments are attached. We attribute this strongly enhanced unbinding rate of doubly bound crosslinkers to the large bending rigidity of the actin filaments, which frustrates doubly bound crosslinkers. Our new kinetic data allow for more precise computational modeling of actin networks [69, 85], and give insight into the dynamics of the cell cortex [4, 97]. Lastly, we expect that our work will help to design synthetic materials with programmed timescales of relaxation [72].

2.2. METHODS

2.2.1. PROTEIN PURIFICATION AND NETWORK FORMATION.

The actin crosslinker human α-actinin 4 (ACTN4) was purified as described in reference [98]: Rosetta E. Coli cells were transformed to express recombinant crosslinkers with a 6xhis-tag. Induction was performed with 500 μM isopropyl β-D-1-thiogalactopyranoside for eight hours at 25^{o}C. After centrifugation at 6000 g for 15 minutes, cells were resuspended in 20 mM NaCl, 5 mg/ml lysozyme and 20 mM Hepes, pH 7.8. The cells were lysed by a freeze-thaw cycle, and centrifuged at 20,000 g for 30 min. The recombinant protein was purified from the supernatant using a QIAGEN nickel column. Next, the column was washed with 20-bed columns of 500 mM NaCl, 25 mM imidazole, and 20 mM Hepes, pH 7.8. The recombinant proteins were eluted with 10-bed volumes of 500 mM NaCl, 500 mM imidazole, and 20 mM Hepes, pH 7.8. The proteins were concentrated using a Centricon filtration device (Millipore) and purified by gel filtration in 150 mM NaCl, 20 mM Hepes pH 7.8, and 10 mM dithiothreitol (DTT) using an AKTA purifier (GE Healthcare) with a Sephadex 200 column. ACTN4 was labeled on cysteine using maleimide-activated Oregon Green at a ratio of five fluorophores for every crosslinker at room temperature for 1 h. Labeled ACTN4 was separated from free dyes by gel filtration using Superdex 200 (GE Healthcare) [98].

All chemicals were bought from Sigma Aldrich unless otherwise mentioned. Actin was purified from rabbit psoas skeletal muscle as described in reference [99] and stored at -80^oC in G-buffer (2 mM tris-hydrochloride pH 8.0, 0.2 mM disodium adenosine triphosphate, 0.2 mM calcium chloride, 0.2 mM dithiothreitol) to prevent polymerization. Unless otherwise mentioned, we used a concentration of 48 μM, corresponding to 2 mg/ml, for all our experiments and actin was polymerized in a buffer consisting of 50 mM KCl, 20 mM imidazole pH 7.4, 2 mM $MgCl_2$, 1 mM DTT and 0.5 mM MgATP (F-buffer). For both rheology and FRAP, all networks were allowed to polymerize at 298 K for two hours before measurements were performed. Unless otherwise mentioned, we used a crosslinker concentration of 0.48 μM to obtain a molar ratio of 1/100 crosslinker/actin and on average about 1 crosslinker per 0.5 μm of actin filament; under these conditions, networks are unbundled and isotropic as verified by confocal fluorescence microscopy [Fig. S4].

2.2.2. SPIN-DOWN ASSAY

A volume of 25 μl monomeric (G-)actin at increasing concentrations was co-polymerized with actin binding proteins in F-buffer at room temperature, keeping the actin binding protein concentration constant (0.1 μM). After two hours of polymerization the actin network together with the bound crosslinkers was spun down at 120 000 g. Afterwards, 20 μl was gently pipetted from the supernatant, mixed with 20 μl InstantBlue and boiled at 95 ^{o}C for 5 minutes in a closed Eppendorf vial. 30 μl of this solution was loaded onto a 4–15 % Mini-PROTEAN TGX™ Precast Protein Gel with 10 wells of 30 µl. Gels were run for 30 minutes at 200 V, washed with Mili-q water, stained overnight with InstantBlue and washed three times with tap water. Band intensities of the ACTN4 in the supernatant were quantified using ImageJ. The fraction of bound linkers ϕ_{bound} was determined by subtracting and normalizing the ACTN4 band intensity at a particular actin concentration by the band intensity in the absence of actin: $\phi_{\text{bound}} = \frac{I - I_0}{I_0}$. Background correction was applied to all band intensities by subtracting the average intensity of a region adjacent to the band of interest.

2.2.3. FLUORESCENCE RECOVERY AFTER PHOTOBLEACHING

The bound crosslinker lifetime within actin networks was measured via Fluorescence Recovery After Photobleaching (FRAP) using a Nikon A1 confocal microscope with a perfect focus system, a 100x oil immersion objective, and a 100-mW 488 nm argon ion laser. The temperature was controlled by a home-built temperature regulator. The regulator consisted of a temperature-controlled water bath connected to a home-made objective heater and a sample glass slide heater. The temperature of the water was measured inside the objective heater via a P1000 temperature sensor. We calibrated the temperature inside the sample, measured by inserting a 0.025 mm thermocouple in a glow channel filled with deionized water, against the temperature inside the objective heater. Using this set-up, temperatures between 285 – 333 K can be achieved.

The FRAP protocol started with 10 images to determine baseline fluorescence. Next, bleaching was performed by using a high intensity laser power such that 50 – 70 % of the fluorescence intensity was bleached in 0.5 seconds. The fluorescence recovery was tracked during a period of approximately 5x the typical recovery time, with a sampling rate that halved every 10 frames, starting with 10 frames per second. Unless otherwise mentioned, a circular area was bleached of 2 μm radius and an equally sized area was used as a reference. The laser intensity during imaging was chosen such that the reference intensity dropped less than 5 % during the recovery phase. To extract a recovery rate, the normalized intensity during recovery I/I_{ref} was fitted with a single exponent $I/I_{\text{ref}} = 1 - I_0/I_{\text{ref}} \cdot \exp(-t \cdot k_{\text{FRAP}})$, where I_0 is the intensity directly after bleaching and k_{FRAP} the recovery rate. The timescale of recovery is governed by the typical crosslinker diffusion time, which scales quadratically with the bleach radius, and the typical crosslinker unbinding time, which is independent of the bleach radius. To dissect these two contributions, we compared the recovery time for different bleach radii, 2 μm and 4 μm. We did not find a statistically significant difference [Fig. 6.17]. This result is consistent with a calculation where we estimate that the typical diffusion distance in the timescale of FRAP recovery time is significantly is much larger than the FRAP radius (40 μm vs. 2 μm). We used a diffusion constant based on the Stokes-Einstein relationship, assuming a crosslinker radius of 3 nm on basis of the crystal structure [100].

2.2.4. RHEOLOGY

Rheology was performed using a stress-controlled Kinexus Malvern Pro rheometer with a stainless steel 20 mm radius cone plate geometry with a 1^o degree angle. We loaded 40 μl G-actin mixed with ACTN4 directly after mixing the proteins into the polymerization buffer (F-buffer). A thin layer of Fluka mineral oil Type A was added around the geometry to prevent evaporation, and the sample was closed off with a hood to minimize effects of air flow. Polymerization of the network was followed by applying a small oscillatory shear with a strain amplitude of 0.5 % and a frequency of 0.5 Hz for 2 h. After 2 h of polymerization, a frequency sweep was performed between 0.01 – 10 Hz, using 10 data points per decade. Frequencies above 10 Hz could not be measured as inertial effects from the rheometer dominated the rheological response of the actin network at high frequencies. After characterization at $25\,^o$C ($298\,K$), the temperature was adjusted and equilibrated for 10 minutes. The typical frequency was extracted from the frequency dependent storage and loss moduli (G' and G'') by fitting a previously published model which considers the multi-relaxation times due to many crosslinks unbinding per filament [37]. The model is based on the nonlinear-force extension curve of a semiflexble filament, and uses mean-field arguments to extract mechanical properties of the network from the single filament fluctuations:

$$G' = y \cdot (\chi' + \alpha'(\omega))/[(\chi' + \alpha'(\omega))^2 + (\chi'' + \alpha''(\omega))^2], \tag{2.1}$$

$$G'' = y \cdot (\chi'' + \alpha''(\omega))/[(\chi' + \alpha'(\omega))^2 + (\chi'' + \alpha''(\omega))^2]. \tag{2.2}$$

y is a prefactor to allow for direct comparison between the semi-quantitative model and experimental data, while χ describes the viscous drag limiting transverse filament fluctuations:

$$\begin{aligned}\chi' = \quad & \tfrac{0.0072}{4\cdot\sqrt{2}} \cdot [-2\arctan(1 - \tfrac{\sqrt{2}}{\sqrt{\omega/\omega_{\text{fluid}}}}) + \\ & 2\arctan(1 + \tfrac{\sqrt{2}}{\omega/\omega_{\text{fluid}}}) + \\ & \log(1 + \tfrac{1}{\omega/\omega_{\text{fluid}}} - \tfrac{\sqrt{2}}{\sqrt{\omega/\omega_{\text{fluid}}}}) - \\ & \log(1 + \tfrac{1}{\omega/\omega_{\text{fluid}}} + \tfrac{\sqrt{2}}{\sqrt{\omega/\omega_{\text{fluid}}}})]/\sqrt{\omega/\omega_{\text{fluid}}},\end{aligned} \tag{2.3}$$

$$\begin{aligned}\chi'' = \quad & \tfrac{0.0072}{4\cdot\sqrt{2}} \cdot [-2\arctan(1 - \tfrac{\sqrt{2}}{\sqrt{\omega/\omega_{\text{fluid}}}}) + \\ & 2\arctan(1 + \tfrac{\sqrt{2}}{\omega/\omega_{\text{fluid}}}) - \\ & \log(1 + \tfrac{1}{\omega/\omega_{\text{fluid}}} - \tfrac{\sqrt{2}}{\sqrt{\omega/\omega_{\text{fluid}}}}) + \\ & \log(1 + \tfrac{1}{\omega/\omega_{\text{fluid}}} + \tfrac{\sqrt{2}}{\sqrt{\omega/\omega_{\text{fluid}}}})]/\sqrt{\omega/\omega_{\text{fluid}}}.\end{aligned} \tag{2.4}$$

Here ω_{fluid} is the timescale of the fluid drag which depends on the fluid viscosity and the mesh size [101] and is typically on the order of 100 Hz for actin networks [102]. Lastly, α describes the effect of the crosslinkers limiting transverse filament fluctuations:

$$\alpha' = \frac{1}{\pi^4}\Sigma_{n=1}^{N}\frac{n^4}{n^8+(\omega/\omega_{\mathrm{off}})^2}, \tag{2.5}$$

$$\alpha'' = \frac{1}{\pi^4}\Sigma_{n=1}^{N}\frac{\omega/\omega_{\mathrm{off}}}{n^8+(\omega/\omega_{\mathrm{off}})^2}. \tag{2.6}$$

Here N is the number of crosslinkers per filament and ω_{off} is the off-rate of the crosslinker. In this work, we refer to this rate as the rheology rate, k_{Rheo}, to prevent confusion with the FRAP rate k_{FRAP}, which is also governed by crosslinker unbinding. The $G' \sim G'' \sim \omega^{-1/2}$ power law extends down to lower frequencies (i.e. larger time scales) for higher numbers of crosslinkers per filament. In line with previous research [37], we arbitrarily assume the number of crosslinkers to be 10, which is likely smaller than the actual number of crosslinkers per filament but still large enough to observe power law behavior of the shear moduli over the full experimental regime. The supplementary information contains the frequency sweeps over the full range of measured temperatures.

2.3. RESULTS

We measure the crosslinker unbinding rate in actin networks using Fluorescence Recovery After Photobleaching (FRAP) by bleaching a circle of 2 μm radius using a high intensity laser power. Afterwards, we track the recovery of fluorescent intensity within this circle and use a reference area to correct for any photobleaching during imaging of the recovery phase. We find that the fluorescent intensity recovery is well-described with a single exponential function with a rate of 0.036 ± 0.001 s^{-1}, and that the intensity asymptotically approaches the fluorescent intensity before bleaching, indicating that all crosslinkers are mobile [Fig. 2.1a].

Next, we measure network mechanics using small amplitude oscillatory shear rheology: we apply an oscillatory strain of 0.5 % amplitude and measure the stress required for this deformation. We analyze the in-phase and out-of-phase contributions (storage and loss component respectively) as a function of the applied frequency. Consistent with earlier observations on transiently cross linked actin networks [52, 56, 81], we observe that the mechanical response can be divided into three frequency regimes [Fig. 2.1b]. Firstly, at low frequencies we observe power law dynamics, consistent with a recent crosslink-governed network dynamics model [37]. Secondly, at intermediate frequencies, the storage modulus increases less steeply while the loss modulus decreases as crosslinker unbinding becomes increasingly unlikely [37, 48]. Lastly, at high frequencies the storage and loss modulus increase again as transverse filament fluctuations are hampered by viscous drag of the surrounding fluid [102]. We note that there is in principle also a fourth regime at very low frequencies, where filaments exhibit terminal relaxation on timescales long enough to allow for filament relaxation of its full length. However, the termination of the $G' \sim G'' \sim \omega^{-1/2}$ power law does not occur within experimentally accessible timescales.

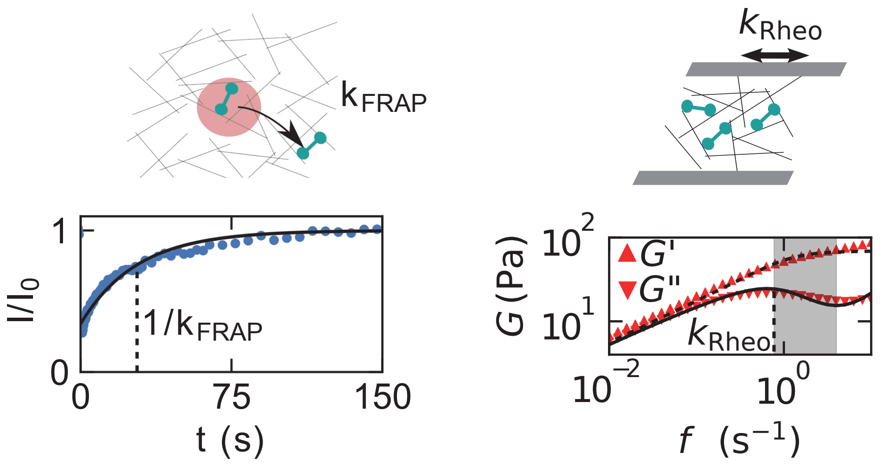

(a) **(b)**

Figure 2.1: Measurements of the FRAP and rheology rates. a) FRAP curve of the fluorescence intensity as function of time after photobleaching (blue dots) together with a fit to a mono-exponential recovery (black line) with a rate of $k_{\mathrm{FRAP}} = 0.036 \pm 0.001\ \mathrm{s}^{-1}$ (dashed line, standard error on basis of 4 repeats). b) Frequency dependence of the storage and loss moduli (upward and downward pointing triangles) together with a fit to the crosslink governed networks dynamics model (dashed and solid lines, Eq. 2.1 and 2.2) . G'' peaks at $k_{\mathrm{Rheo}} = 0.77 \pm 0.03\ \mathrm{s}^{-1}$ (vertical dashed line, standard error on basis of fit). Both FRAP and rheology data are obtained at 283 K. The shading highlights the intermediate regime. The actin filaments (black), crosslinkers (green) and FRAP area (red) in the schematics are not drawn to scale.

We fit our experimental data over all three regimes using the cross-link governed network dynamics model [37], giving a rate k_{Rheo} of $0.77 \pm 0.03\ \mathrm{s}^{-1}$ (indicated by the vertical line in Fig. 2.1b). The only other fit parameters are the timescale of fluid drag ($45\ \mathrm{s}^{-1}$) and a pre-factor to scale the y-axis (0.02 Pa). According to the model [37], this timescale should be equal to the crosslinker unbinding timescale the FRAP rate is more than an order of magnitude slower at the same temperature.

To test the robustness of this difference in rates, we perform FRAP and rheology measurements as a function of temperature (280 – 298 K). As shown in Fig. 2.2, the FRAP and rheology rates both increase with temperature in accordance with the Arrhenius equation for thermally activated processes, $k(T) \sim \exp(-E_A/T)$, where k is the rate, T is the temperature. We can therefore extract activation energies E_A for the FRAP rate of $33 \pm 4\, k_B$T and for the rheology rate of $75 \pm 3\, k_B$T [Fig. 2.2]. Interestingly, this implies that the onset frequency for stress relaxation as measured by rheology is significantly more temperature-dependent than the crosslinker unbinding rate as measured by FRAP. Furthermore, the onset frequency for stress relaxation is higher than the crosslinker unbinding rate over the full range of measured temperatures.

In order to explain the ~20-fold difference in timescale between the characteristic

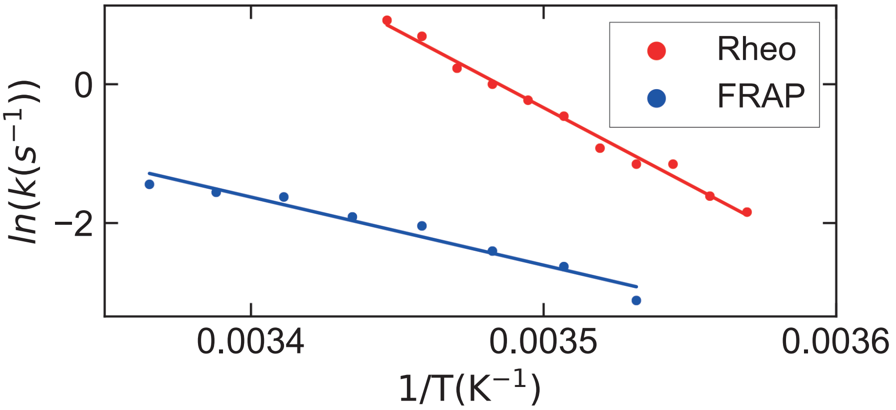

Figure 2.2: Arrhenius plot of the characteristic crosslink unbinding rates inferred from FRAP and rheology analysis. Fitting both sets of data to the Arrhenius equation (solid lines) yields an activation energy of $33 \pm 4\, k_\mathrm{B}\mathrm{T}$ for FRAP and $75 \pm 3\, k_\mathrm{B}\mathrm{T}$ for rheology.

rates inferred from FRAP and rheology, we hypothesize that stress relaxation in crosslinked actin networks occurs as soon as one of the actin binding domains of a crosslinker unbinds. In contrast, crosslinker redistribution as measured by FRAP requires both binding domains to detach. To formalize this hypothesis, we model the crosslinker dynamics by a three-state model where crosslinkers are either bound to zero (s_0), one (s_1) or two filaments (s_2). In this framework, the onset frequency for stress relaxation is defined by the rate of an s_2 crosslinker to unbind from one filament:

$$k_\mathrm{Rheo} = k_{21}. \tag{2.7}$$

The FRAP rate is more complex, as it requires unbinding from both filaments. Note that this rate is potentially much longer than the rate k_{21} as measured by rheology, as cycling between the singly and doubly bound state can occur many times before the crosslinker fully unbinds. We hypothesize that this cycling between both binding sites explains the difference in timescales between FRAP and rheology observed experimentally. As explained in detail in the Supplementary Information, we find an analytical solution for the experimentally observed rate of bound crosslinkers (s_1 and s_2) transitioning to free crosslinkers (s_0) which takes into account this cycling effect:

$$\begin{aligned} k_\mathrm{FRAP} = & \quad {}^1\!/\!_2 \cdot (k_{10} + k_{12} + k_{21}) - \\ & {}^1\!/\!_2 \cdot \sqrt{(k_{10} + k_{12} + k_{21})^2 - 4 \cdot k_{10} \cdot k_{21}}. \end{aligned} \tag{2.8}$$

The FRAP rate contains two unknown parameters, k_{10} and k_{12}, which we can dissect by measuring the recovery rate as a function of the actin concentration: whereas the unbinding rates k_{10} and k_{21} are independent of the actin concentration, the binding rate

k_{12} increases linearly as the average filament-filament distance decreases. Assuming that there is no spatial correlation between filaments:

$$k_{12} = k_{12,\mathrm{act}} \cdot [\mathrm{actin}], \tag{2.9}$$

where [actin] is the concentration of actin in μM and $k_{12,\mathrm{act}}$ the binding rate at an actin concentration of 1 μM. Consequently, the three-state model predicts that the FRAP rate decreases with an increase of the actin concentration, as crosslinkers reside more often in the double bound state. Consistent with this prediction, we find that the FRAP rate decreases from $0.31 \pm 0.04\ \mathrm{s}^{-1}$ at 24 μM actin to $0.21 \pm 0.02\ \mathrm{s}^{-1}$ at 60 μM actin [Fig. 2.3a]. In contrast, the onset frequency of stress relaxation as measured with rheology does not depend on the actin concentration (Refs. [37, 52, 56] and Fig. 2.8), as the unbinding rate k_{21} is independent from the actin concentration. We next combine eq. 2.8 and 2.9 to fit the FRAP data as a function of the actin concentration and find $0.43 \pm 0.06\ \mathrm{s}^{-1}$ for the unbinding rate k_{10} and $0.3 \pm 0.1\ \mathrm{s}^{-1}$ for the binding rate k_{12} at an actin concentration of 48 μM.

Lastly, in order to measure k_{01}, we perform a spindown assay to separate actin-bound crosslinkers ($s_1 + s_2$) from freely diffusing crosslinkers (s_0) as a function of the actin concentration. We find that the fraction of bound crosslinkers increases with the concentration of actin [Fig. 2.3b]. Like k_{12}, the binding rate k_{01} increases linearly with the actin concentration:

$$k_{01} = k_{01,\mathrm{act}} \cdot [\mathrm{actin}]. \tag{2.10}$$

Due to detailed balance, we know that the fraction of bound linkers depends on all (un)binding rates according to (see SI for the derivation):

$$\phi_{\mathrm{bound}} = \frac{s_1 + s_2}{s_0 + s_1 + s_2} = \frac{k_{01} \cdot k_{21} + k_{01} \cdot k_{12}}{k_{10} \cdot k_{21} + k_{01} \cdot k_{21} + k_{01} \cdot k_{12}}. \tag{2.11}$$

Using this equation, we fit the spin-down data to extract the last unknown rate, $k_{01,\mathrm{act}}$ and find $0.83 \pm 0.03\ \mathrm{s}^{-1}$. All rates are summarized in Fig. 2.3c.

2.4. DISCUSSION

We have compared the dynamics of crosslinker unbinding in actin networks as measured by fluorescence recovery after photobleaching and by rheology. Surprisingly, we have found that the crosslinker unbinding rate measured by FRAP is more than an order of magnitude slower than the onset frequency of stress relaxation measured by rheometry. We have rationalized this difference with a three-state model where crosslinkers are bound to either 0, 1 or 2 filaments. Whereas stress relaxation in the network already occurs as soon as crosslinkers unbind from one of the two filaments, full crosslinker unbinding as measured by FRAP requires detachment from both filaments. Our results are consistent with rheology [37, 81] and FRAP measurements [38, 82–84] in literature and provide a mechanistic explanation to the difference in rates. Furthermore, we have used this model to extract crosslinker transition rates that are otherwise difficult to access.

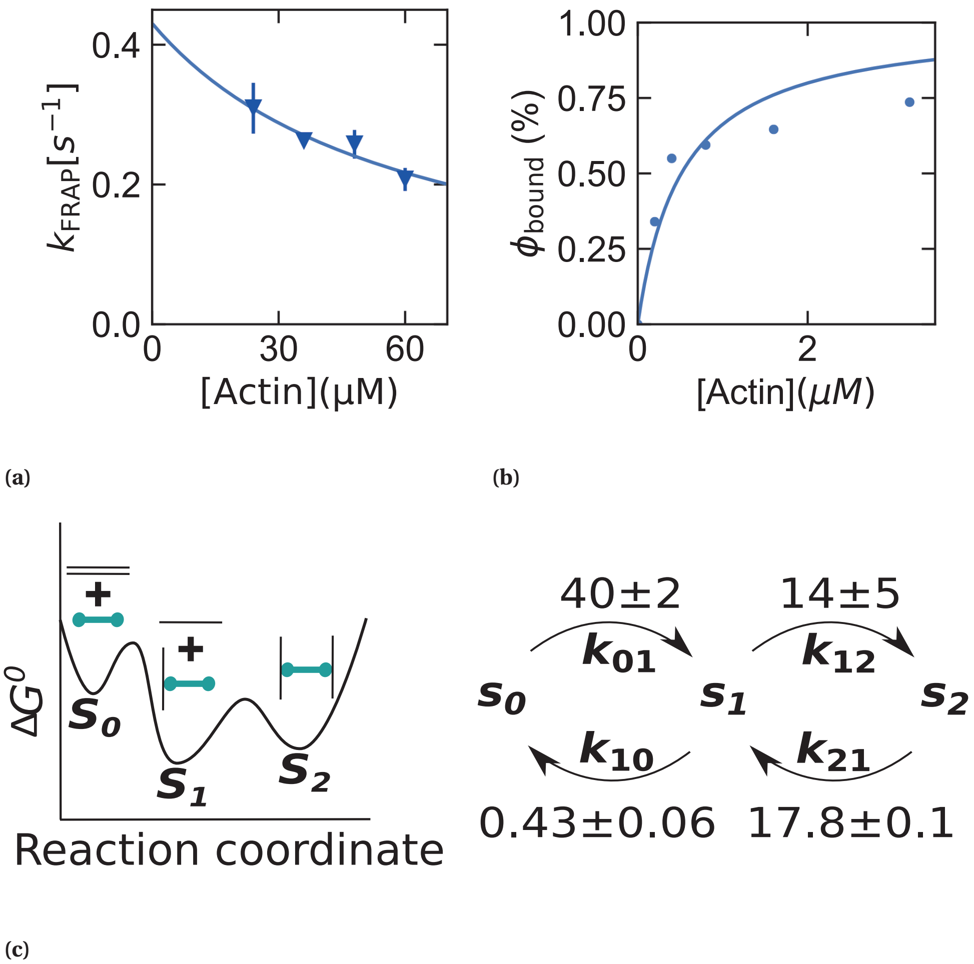

(a)

(b)

(c)

Figure 2.3: Retrieving crosslinker binding and unbinding rates from a three-state model.a) The FRAP rate as a function of actin concentration measured at 298 K is fitted with the three-state model (line; eqs. 2.8 and 2.9) to extract k_{10} and k_{12}. The error bars are the standard error calculated on basis of 4 repeats per condition. b) The fraction of bound crosslinkers as a function of the actin concentration is fitted with Eq. 2.11 (line) to extract k_{01}. c) All rates are in s^{-1} and with standard error on basis of the fit, measured at 25 ^{o}C at an actin concentration of 48 μM. The rate k_{21} is extrapolated to $T = 25\,^{o}$C using the Arrhenius plot of the onset frequency of stress relaxation [Fig. 2.2].

Interestingly, we have found that the unbinding rate of a crosslinker attached to one filament is more than an order of magnitude slower than when two filaments are attached (0.43 ± 0.06 s^{-1} vs. 17.8 ± 0.1 s^{-1}). This difference suggests that binding of a second filament causes crosslinker frustration, which speeds up crosslinker-filament dissociation. This crosslinker frustration is different from the frustration of actin *filaments* in crosslinked bundles [103], which is due to the helical pitch of actin filaments [104, 105]. Instead, we attribute the increased crosslinker unbinding to deformation of the *crosslinker* [106, 107]. Steered molecular dynamics have revealed that torsion in the ACTN4 backbone is energetically highly unfavorable and a 180^o torsion requires $\sim 75\,k_{\mathrm{B}}$T, similarly a crosslinker extension of 10% requires $\sim 70\,k_{\mathrm{B}}$T [106]. As the persistence length of actin filaments is large ($\sim 10\ \mu$m [93]) compared to the typical crosslinker distance ($\sim 0.5\ \mu$m), binding of two filaments likely causes constraints in the crosslinker orientation and length. Therefore, we speculate that crosslinker frustration should be common in crosslinked semiflexible polymer networks. Our work provides an experimentally straightforward way to characterize the crosslinker kinetics by combining rheology with FRAP measurements, for example as a function of the crosslinker compliance [33, 88].

We thank Harmen Wieringa and Piet Rein ten Wolde for the analytical derivation of the equations presented in the appendix. We thank Wouter Ellenbroek, Nicholas Tito, Fred MacKintosh and Chase Broedersz for fruitful discussions. We thank William Brieher and Vivian Tang for the kind gift of purified ACTN4, Marjolein Kuit-Vinkenoog for actin purification, Henk-Jan Boluit for design and Philippine Doekes for testing and calibrating the temperature control.

APPENDIX

THREE STATE MODEL

We are interested in the rate at which crosslinkers fully unbind. We consider crosslinkers with two 'heads', i.e. binding sites for actin filaments; this means they can be in three states, unbound, single head bound, two heads bound. Bound crosslinkers start off in a distribution over both states 1 (single head bound) and 2 (both heads bound). Here, we will calculate the first passage time distributions to the full unbinding (state 0), given that the crosslinkers start in state 1 or state 2. The combined first passage time distribution is a linear combination of these two subdistributions. We will show that this distribution is peaked, and decays exponentially afterwards. We show that the FRAP recovery curve is governed by this exponent, which we calculate analytically on basis of the crosslinker (un)binding rates.

We denote the first passage time distribution from state i to state j by $f_{i,j}(t)$, which gives the probability density that a crosslinker starting at state i reaches state $j \neq i$ for the first time after a period t. Hence, our goal is to calculate $f_{1,0}(t)$ and $f_{2,0}(t)$. The latter distribution can be decomposed into the first time t' that the crosslinker arrives from state 2 to state 1, and the time $t - t'$ it takes to finally make it to state 0,

$$f_{2,0}(t) = \int_0^t f_{2,1}\left(t'\right) f_{1,0}\left(t - t'\right) \mathrm{d}t'. \tag{2.12}$$

This convolution can be resolved using the Laplace transform

$$\widetilde{f}_{i,j}(s) \equiv \int_0^\infty f_{i,j}(t)\, \mathrm{e}^{-st}\, \mathrm{d}t, \tag{2.13}$$

which applied changes the convolution of Eq. 2.12 into a simple product

$$\widetilde{f}_{2,0}(s) = \widetilde{f}_{2,1}(s)\, \widetilde{f}_{1,0}(s). \tag{2.14}$$

There is only a single rate leaving from state 2, giving a simple form of the first passage time distribution to state 1:

$$f_{2,1}(t) = k_{21} \mathrm{e}^{-k_{21} t}, \tag{2.15}$$

where k_{21} is the rate at which a crosslinkers go from state 2 to state 1. The Laplace transform of this equation gives

$$\widetilde{f}_{2,1}(s) = \frac{k_{21}}{s + k_{21}}. \tag{2.16}$$

There are two options for a crosslinker bound with a single head, namely binding the loose head or fully unbinding. This means that the first passage time probability $f_{1,0}(t)$ can be split into a part where the first step is unbinding, and a part where the first step involves full binding. When the first step is towards state 2 at time t', then a first passage is required from state 2 to state 0 in the remaining time, leading to

$$\begin{aligned} f_{1,0}(t) =& k_{10}\mathrm{e}^{-(k_{10}+k_{12})t} \\ &+ \int_0^t k_{12}\mathrm{e}^{-(k_{10}+k_{12})t'} f_{2,0}\left(t-t'\right)\mathrm{d}t'. \end{aligned} \tag{2.17}$$

Again, we perform a Laplace transform on both sides of the equation to resolve the convolution. Eq. 2.14 and Eq. 2.16 subsequently are used to create a linear equation for $\widetilde{f}_{1,0}(s)$,

$$\begin{aligned} \widetilde{f}_{1,0}(s) =& \frac{k_{10}}{s+k_{10}+k_{12}} \\ &+ \frac{k_{12}}{s+k_{10}+k_{12}}\frac{k_{21}}{s+k_{21}}\widetilde{f}_{1,0}(s)\,. \end{aligned} \tag{2.18}$$

The solution of this equation is given by

$$\widetilde{f}_{1,0}(s) = \frac{k_{10}\,(s+k_{21})}{s^2+(k_{10}+k_{12}+k_{21})\,s+k_{10}k_{21}} \tag{2.19}$$

$$= \frac{k_{10}}{r_2-r_1}\left[\frac{k_{21}-r_1}{s+r_1}+\frac{r_2-k_{21}}{s+r_2}\right], \tag{2.20}$$

while through Eq. 2.14,

$$\widetilde{f}_{2,0}(s) = \frac{k_{10}k_{21}}{s^2+(k_{10}+k_{12}+k_{21})\,s+k_{10}k_{21}} \tag{2.21}$$

$$= \frac{k_{10}k_{21}}{r_2-r_1}\left[\frac{1}{s+r_1}-\frac{1}{s+r_2}\right]. \tag{2.22}$$

Here, we defined the two positive effective rates

$$\begin{aligned} r_1 =& \frac{1}{2}\,(k_{10}+k_{12}+k_{21}) \\ &- \frac{1}{2}\sqrt{(k_{10}+k_{12}+k_{21})^2-4k_{10}k_{21}}, \end{aligned} \tag{2.23}$$

$$\begin{aligned} r_2 =& \frac{1}{2}\,(k_{10}+k_{12}+k_{21}) \\ &+ \frac{1}{2}\sqrt{(k_{10}+k_{12}+k_{21})^2-4k_{10}k_{21}}. \end{aligned} \tag{2.24}$$

For a general initial state, of which the fraction in state 1 is α, and thus the fraction in state 2 is $(1-\alpha)$, the first passage time distribution from that general state to state 0 is defined as

$$f_{2-\alpha,0}(t) = \alpha f_{1,0}(t) + (1-\alpha)\,f_{2,0}(t) \tag{2.25}$$

The general solution can be found by applying inverse Laplace transforms to Eq. 2.20 and Eq. 2.22. We make use of the inverse Laplace transform, and solve the complex integrals using Cauchy's residue theorem.

$$f_{2-\alpha,0}(t) = \frac{k_{10}}{r_2 - r_1} \cdot \left[(k_{21} - \alpha r_1)\, \mathrm{e}^{-r_1 t} - (k_{21} - \alpha r_2)\, \mathrm{e}^{-r_2} \right]. \tag{2.26}$$

This is the general solution for the first passage time distribution. It can be shown that $r_1 < k_{21} < r_2$, and since $0 \leq \alpha \leq 1$, we may write

$$f_{2-\alpha,0}(t) = \frac{k_{10}}{r_2 - r_1} (k_{21} - \alpha r_1)\, \mathrm{e}^{-r_1 t} \left[1 - \frac{k_{21} - \alpha r_2}{k_{21} - \alpha r_1} \mathrm{e}^{-(r_2 - r_1)} \right]. \tag{2.27}$$

This distribution contains an exponential tail with a rate k_{tail} which equals

$$k_{tail} = \lim_{t \to \infty} \frac{\log \left[f_{2-\alpha,0}(t) \right]}{t} = \lim_{t \to \infty} \frac{\dot{f}_{2-\alpha,0}(t)}{f_{2-\alpha,0}(t)} = r_1. \tag{2.28}$$

We argue that this rate is related to the rate observed in FRAP experiments performed on actin networks crosslinked by fluorescently tagged crosslinkers. Unbound linkers diffuse into the bleached region and are responsible for the recovery of fluorescence. Furthermore, detailed balance imposes that the flux of unbinding events from the dark region must equal the flux of binding new fluorescent crosslinkers. As the recovery rate is insensitive to the size of the bleach area, we assume that the diffusion time is negligibly small compared to the unbinding time. Therefore, the observed recovery rate equals the unbinding rate of the linkers, k_{tail}.

This can be made more explicit by directly considering the dark and fluorescent fractions in the bleached area. Denote by π_i the equilibrium fractions in state i, and call the dark and fluorescent fractions $p_i^D(t)$ and $p_i^F(t)$ respectively. The fluorescent fraction becomes smaller than π_i at $t = 0$, the moment of bleaching. Since the total amount of molecules does not change, we have

$$\pi_i = p_i^D(t) + p_i^F(t). \tag{2.29}$$

The assumption of a negligibly small diffusion time makes that $p_0^D(t) = 0$ and $p_0^F(t) = \pi_0$. For the two fluorescent fractions in the bound states the master equation can be given in vector form when we define the vector

$$\mathbf{p}^F(t) = \begin{pmatrix} p_1^F(t) \\ p_2^F(t) \end{pmatrix}. \tag{2.30}$$

The master equation is then

$$\dot{\mathbf{p}}^F(t) = \begin{pmatrix} -(k_{10} + k_{12}) & k_{21} \\ k_{12} & -k_{21} \end{pmatrix} \mathbf{p}^F(t) + \begin{pmatrix} k_{01}\pi_0 \\ 0 \end{pmatrix}. \tag{2.31}$$

$$= -M\mathbf{p}^F(t) + \mathbf{b}. \tag{2.32}$$

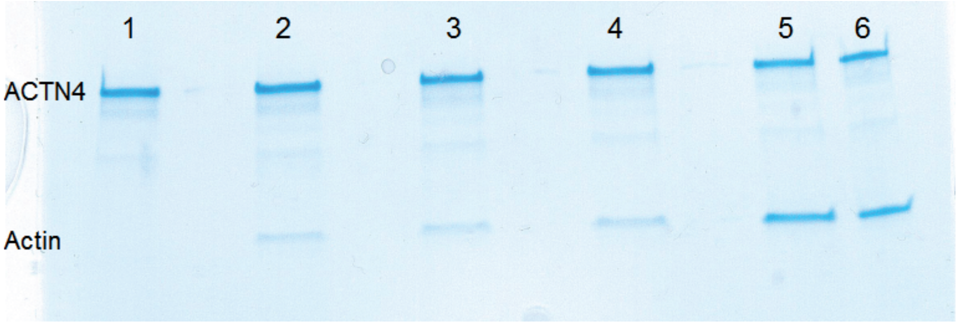

Figure 2.4: SDS-PAGE gel stained with Instant blue. The supernatant resulting from a high-speed centrifugation of a mixture of actin filaments and crosslinkers was put on a polyacrylamide gel. The top band shows the ACTN4 (100 kDa) and the lower band shows actin (42 kDa). Each channel contains a different actin concentration: $1 = 0\,\mu$M, $2 = 0.2\,\mu$M, $3 = 0.4\,\mu$M, $4 = 0.8\,\mu$M, $5 = 1.6\,\mu$M and $6 = 3.2\,\mu$M.

On the second line, the negative of the matrix is named M and the constant vector contribution is $\mathbf{b}$. The particular solution of this differential equation is constant,

$$\mathbf{p}_p^F(t) = M^{-1}\mathbf{b}. \tag{2.33}$$

The homogeneous solutions can be created by finding the eigenvectors and eigenvalues of M, and decomposing $\mathbf{p}^D(t)$ into these eigenvectors. The contribution to the solution of each eigenvector decays with a rate equal to its corresponding eigenvalue. The eigenvalues of M are exactly r_1 and r_2, so using a similar analysis as before in equation 2.28, we conclude that the fluorescence recovery rate equals r_1 in the long time limit.

APPROXIMATION OF THE RECOVERY RATE

For the experimentally relevant regime of small k_{10}, the rate in Eq. 2.23 can be approximated by the mean first passage time [Fig. 2.9]. First, we look at the general solution Eq. 2.26 and choose α such that the dark fractions in state 1 and 2 initially obey detailed balance,

$$\alpha = \frac{k_{21}}{k_{12} + k_{21}}. \tag{2.34}$$

We call this initial state π, which gives the first passage time distribution

$$\begin{aligned} f_{\pi,0}(t) = &\frac{k_{10}k_{21}}{r_2 - r_1} \\ &\left[\left(1 - \frac{r_1}{k_{12} + k_{21}}\right)e^{-r_1 t} + \left(\frac{r_2}{k_{12} + k_{21}} - 1\right)e^{-r_2 t}\right]. \end{aligned} \tag{2.35}$$

This distribution has mean value

$$\tau_\pi = \frac{k_{12} + k_{21}}{k_{10}k_{21}} + \frac{k_{12}}{k_{21}\left(k_{12} + k_{21}\right)} \approx \frac{k_{12} + k_{21}}{k_{10}k_{21}}. \tag{2.36}$$

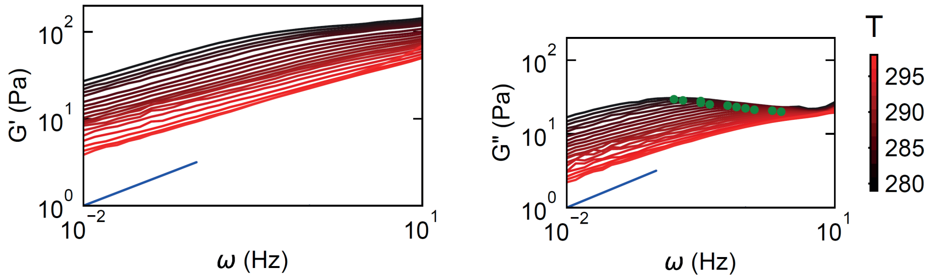

(a) **(b)**

Figure 2.5: Rheology at different temperatures. Frequency sweeps of the storage (a) and loss (b) modulus measured at different temperatures from 280 K (black) to 298 K (red) reveal an increase of the storage and loss modulus and a decrease of the the typical frequency ω_{rheo} (green dots) as a function of temperature.

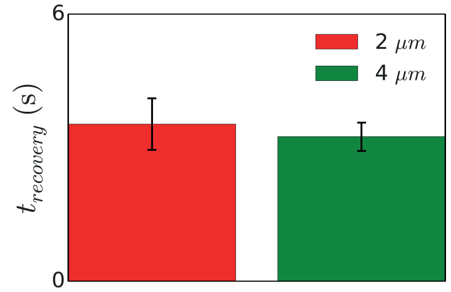

Figure 2.6: Effect of FRAP bleach area on the FRAP rate. The average recovery time for a FRAP radius of 2 μm is not significantly different from a FRAP radius of 4 μm, suggesting the recovery time is not significantly affected by the diffusion time of the crosslinkers, but instead is dominated by the crosslinker unbinding time. Data was acquired at 298 K. The error bars represent the standard error on basis of 4 repeats per condition.

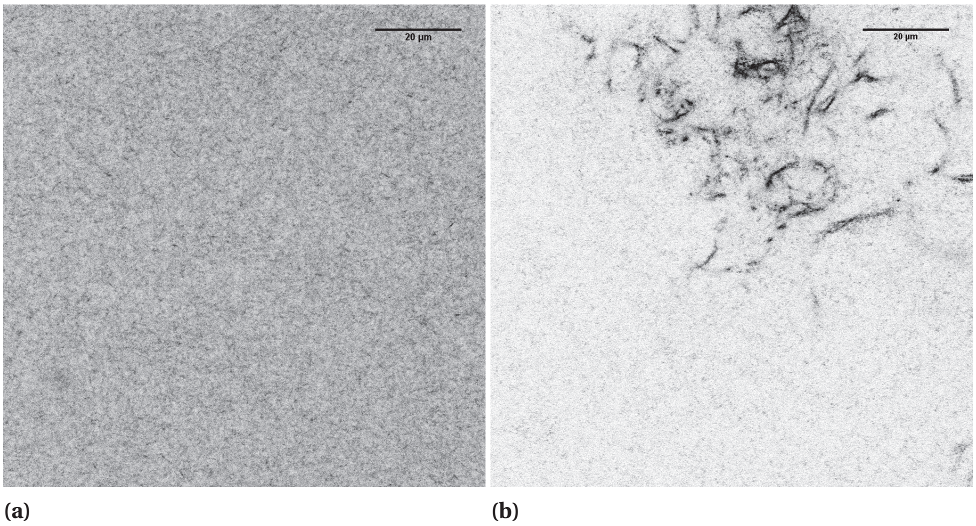

(a) **(b)**

Figure 2.7: Confocal fluorescence images of ACTN4 crosslinked actin networks a) At a 1:100 ACTN4:actin molar ratio, the concentration used for all experiments in this manuscript, an isotropically crosslinked actin network is observed with no structure above the diffraction limit. b) For comparison, actin bundles were observed at a 1:25 ACTN4:actin molar ratio. The color coding was inverted for both images to improve the visual contrast between bundles and background. Scale bars are 20 μm.

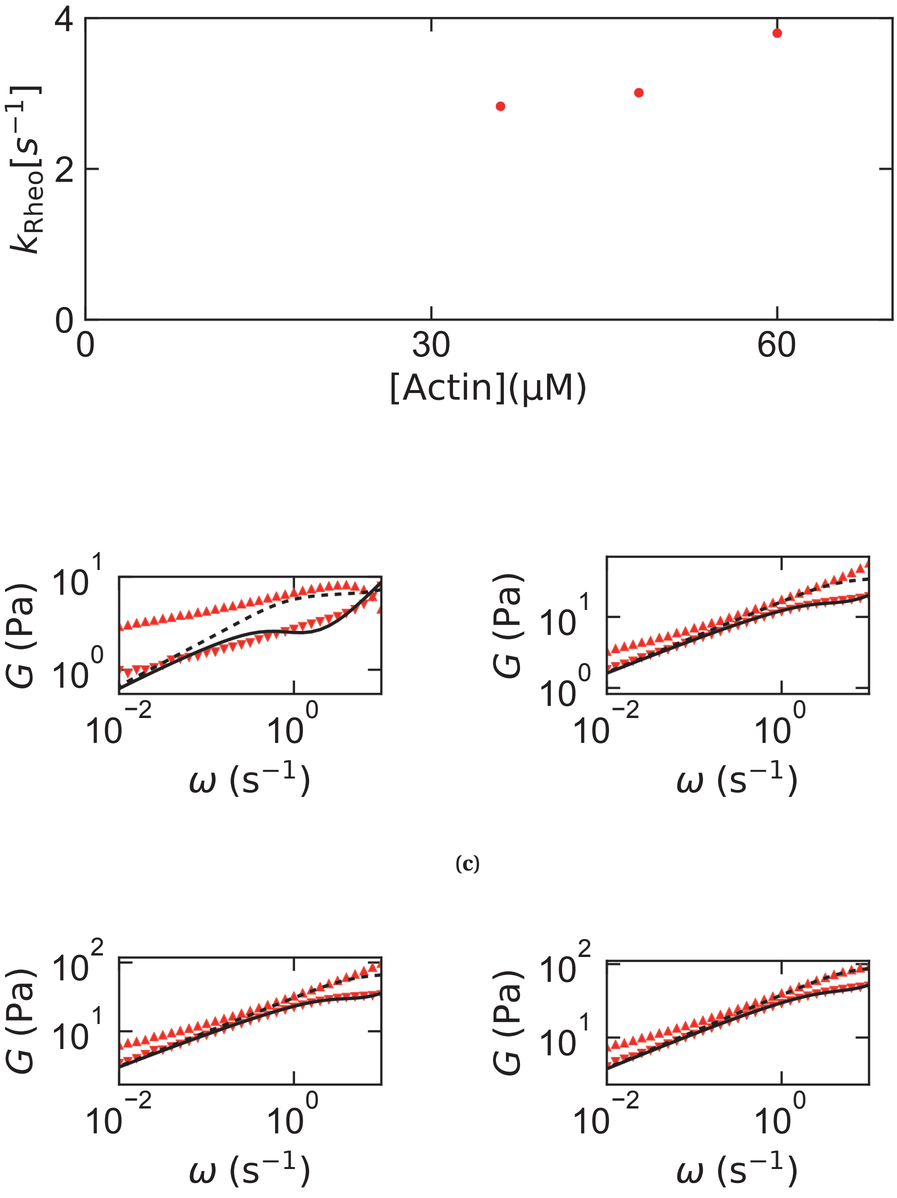

(a)

(b) **(c)**

(d) **(e)**

Figure 2.8: Rheology at different actin concentrations. a) In contrast to the FRAP rate, the rate measured by rheology does not decrease with the actin concentration. Remarkably, a slight increase of the onset frequency of stress relaxation upon an increase of the actin concentration is observed, although that might be due to the imprecision of the fit. Indeed, previous studies found that the timescale measured with rheology is concentration-independent [37, 52, 56]. b-e) The storage and loss modulus (upward and downward pointing triangles) as a function of frequency for 24 (b), 36 (c), 48 (d) and 60 μM actin (e) measured at 298 K. The dashed and solid lines show the fit on basis of eqs. 2.1 and 2.2. The timescale measured at an actin concentration of 24 μM was discarded because of the poor quality of the fit.

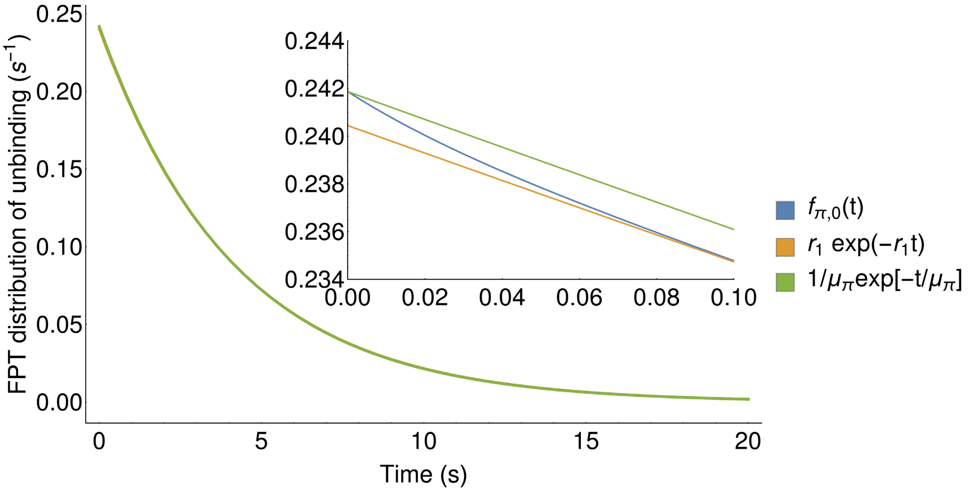

Figure 2.9: Crosslinker unbinding kinetics. The unbinding time distribution for crosslinkers that are initially singly or doubly bound with probabilities set by detailed balance (blue). The exponential distributions with rates equaling the long time tail (orange, Eq. 2.37) and the approximate mean unbinding time (green, Eq. 2.36) are also given. For small time, the true distribution deviates slightly from the approximate lines (inset), but all distributions coincide for larger times. The parameter values used are $k_{10} = 0.43\,\mathrm{s}^{-1}$, $k_{12} = 14\,\mathrm{s}^{-1}$, and $k_{21} = 18\,\mathrm{s}^{-1}$.

The approximation is valid when $k_{10} \ll k_{12}, k_{21}$. We can approximate Eq. 2.23 in the same regime, giving

$$r_1 = \frac{1}{2}(k_{10}+k_{12}+k_{21})\left(1-\sqrt{1-\frac{4k_{10}k_{21}}{(k_{10}+k_{12}+k_{21})^2}}\right), \tag{2.37}$$

$$\approx \frac{1}{2}\frac{1}{2}\frac{4k_{10}k_{21}}{k_{10}+k_{12}+k_{21}} \tag{2.38}$$

$$\approx \frac{k_{10}k_{21}}{k_{12}+k_{21}}. \tag{2.39}$$

The first line uses that $\sqrt{1+\epsilon} \approx 1+\epsilon/2$. Hence, we see that $r_1 \approx 1/\mu_\pi$ when k_{10} is small, and equals k_{10} times the fraction that is in state 1, as given by Eq. 2.34.

EQUILIBRIUM FRACTIONS

The fractions occupying the three states 0, 1, and 2 are set by the transition rates between them and by detailed balance. We call π_i the equilibrium, stationary fraction in state i. Detailed balance says that

$$k_{01}\pi_0 = k_{10}\pi_1, \tag{2.40}$$

$$k_{12}\pi_1 = k_{21}\pi_2. \tag{2.41}$$

Together with the normalization condition $\pi_0 + \pi_1 + \pi_2 = 1$, this gives the solutions

$$\pi_0 = \frac{k_{10}k_{21}}{k_{10}k_{21} + k_{01}k_{21} + k_{01}k_{12}}, \tag{2.42}$$

$$\pi_1 = \frac{k_{01}k_{21}}{k_{10}k_{21} + k_{01}k_{21} + k_{01}k_{12}}, \tag{2.43}$$

$$\pi_2 = \frac{k_{01}k_{12}}{k_{10}k_{21} + k_{01}k_{21} + k_{01}k_{12}}. \tag{2.44}$$

3

ORIGINS OF SOFT GLASSY RHEOLOGY IN THE CYTOSKELETON

Dynamically crosslinked semiflexible biopolymers such as the actin cytoskeleton govern cell shape and mechanics. Semiflexible biopolymers stiffen nonlinearly in response to mechanical loads, whereas the crosslinker dynamics allow for stress relaxation over time. Here we show, through a combination of rheology and theoretical modeling, that the combined nonlinearity in time and stress leads to an unexpectedly slow stress relaxation, similar to disordered systems close to the glass transition. Our work suggests that transient crosslinking combined with internal stress is the microscopic origin for the universal glassy dynamics as frequently observed in cellular mechanics.

3.1. INTRODUCTION

Biopolymers form the scaffolds of life, providing rigidity to both cells and their extracellular matrix [39, 108]. An important characteristic of biopolymers such as fibrin [109], intermediate filaments [71] and actin [48] is their high bending rigidity relative to most synthetic polymers. This generally leads to a competition between entropic and energetic effects that results in a range of material properties not captured by traditional polymer physics. One such property is the highly nonlinear elastic response of biopolymer networks, in which the shear rigidity can increase by orders of magnitude upon deformations by only a few percent [51]. For permanently crosslinked semiflexible polymer networks, this phenomenon is well accounted for by the compliance due to transverse bending fluctuations that become suppressed under a load [48, 50].

The interactions of biopolymers are also complex. An example is the transient crosslinking by specialized crosslinker proteins that takes place in the actin cortex, which causes stress relaxation on timescales much longer than the typical cross-linker unbinding time [95, 110]. The resulting viscoelastic flow does not follow a simple Maxwell model with a single relaxation time, but instead follows power law behavior characteristic of multiple relaxation times [37].

Here, we show that the nonlinear response of transiently crosslinked actin networks exhibits an unexpectedly slow stress relaxation, similar to soft glassy systems [73, 80]. Interestingly, in contrast with prior models of soft glassy rheology [75, 76, 79], this behavior is only observed in the nonlinear regime. We show that the time- and stress-dependent response of actin networks is consistent with a model that accounts for both the nonlinear stiffening [48, 50] and transient crosslinking [37] of semi-flexible polymers. Our results may provide an explanation for many prior reports of slow relaxation and near solid-like viscoelastic response in reconstituted cytoskeletal networks [75, 78] and in living cells [73, 74, 77, 94, 111–113]. While these phenomena have been discussed in the context of phenomenological soft glassy rheology [73–79], a more microscopic mechanism has been lacking. The present work suggests that the glassy dynamics in the cytoskeleton are a natural consequence of transient cross-links, combined with prestress.

3.2. RESULTS

Using small amplitude oscillatory rheology, we measure the storage (crosses) and loss moduli (circles) in the absence of prestress (black data points) as a function of frequency of actin networks, which are isotropically crosslinked by the dynamic linker α-actinin-4 (ACTN4), a prominent crosslinker in human cells [114, 115] [Fig. 3.1c]. Qualitatively consistent with previous experiments, we find a power law frequency dependence of the moduli at frequencies below 1 Hz (black line) with an exponent close to $1/2$, as previously predicted theoretically and observed experimentally [37]. The $^1/_2$ exponent reflects the broad spectrum of relaxation times from the unbinding and rebinding of multiple crosslinkers along a filament [Fig. 3.1a] [37]. The viscous modulus becomes less frequency dependent for higher frequencies (> 1 Hz) , and is expected to peak at the crosslinker unbinding rate (not observed here and therefore likely beyond 10 Hz) as crosslinker unbinding becomes increasingly unlikely [37].

Next, we measure the nonlinear storage and loss moduli using a superimposed small

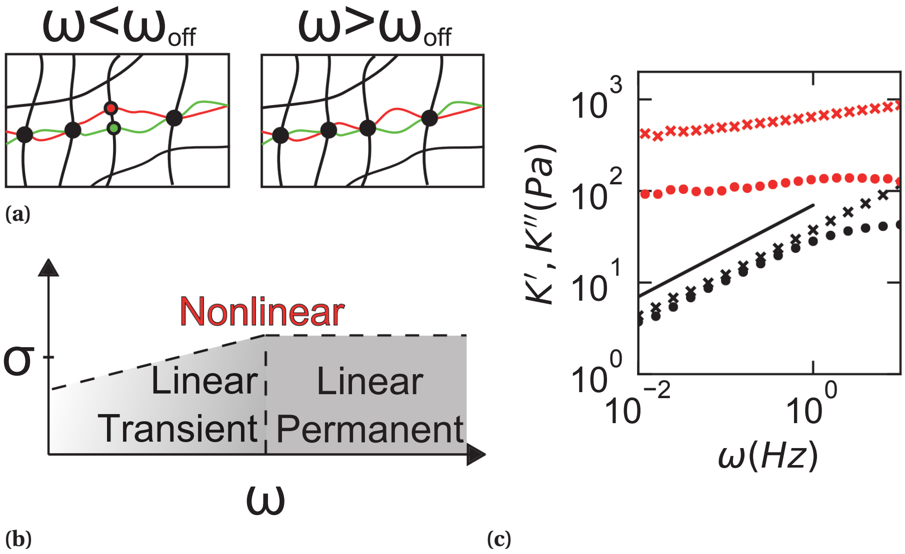

Figure 3.1: Time-dependent viscoelastic response of transiently crosslinked semiflexible polymer networks. a) Schematic of network of actin filaments (black lines) connected by crosslinkers (black dots). Left: filament before and after a crosslinker remodeling event (green and red). Right: such events are unlikely for frequencies larger than the crosslinker unbinding rate ω_{off}. b) Schematic phase diagram showing three different viscoelastic regimes as a function of time and applied stress. At low stresses in the linear elastic regime, networks behave as permanent networks or crosslink kinetics dominate the dynamics, depending on frequency. Our work shows that beyond an onset stress, a single length scale that is nonlinear in both stress and frequency governs the mechanics. This onset stress decreases for frequencies below the crosslinker unbinding rate as the effective crosslinker distance decreases. c) The storage (crosses) and loss moduli (circles) of a crosslinked actin network against frequency in the absence of prestress (black) and for 8 Pa prestress (red). The lines indicates a 1/2 power law.

amplitude oscillation in the presence of 8 Pa prestress (red data points in Fig. 3.1c). We find that both moduli are larger in the presence of prestress by 1-2 orders of magnitude than in the absence of prestress over the entire frequency range. We attribute this increase in moduli to the stress stiffening response of semiflexible polymer networks due to suppression of filament bending fluctuations [48, 50]. More surprisingly, we find that both the storage and loss moduli are significantly less frequency-dependent in the presence of prestress than the 1/2 power law observed in the absence of prestress.

To find out the origin of the stress-dependent changes in the time-dependent rheology, we systematically vary the prestress over a range from 0.1 to 8.0 Pa with a superimposed small amplitude oscillation at different frequencies ($\omega = 0.01...10$ Hz). We find that that both the differential storage and loss moduli increase as a function of prestress over all frequencies [Fig. 3.2]. This increase is consistent with a $\sigma^{3/2}$ power-law stress stiffening, as previously identified both experimentally and theoretically for semiexible polymer networks [51, 71]. To test the agreement with the model more quantitatively, we

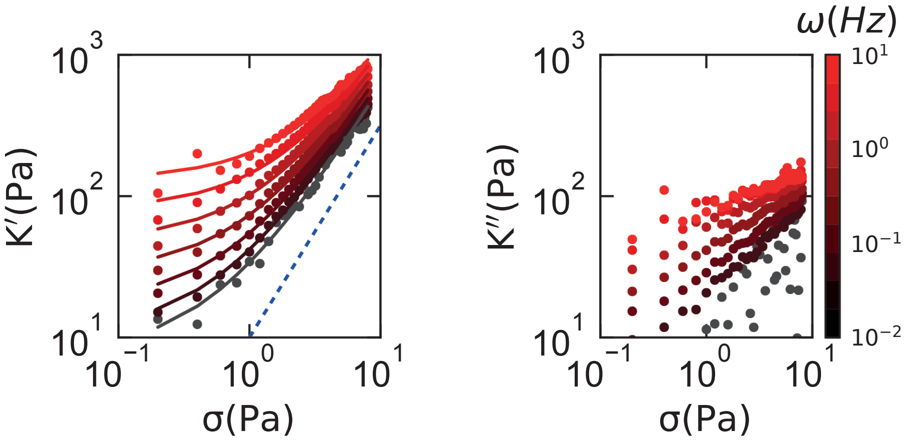

(a)

(b)

Figure 3.2: Time-dependent stiffening. The differential storage (a) and loss (b) moduli of an ACTN4 crosslinked actin network are plotted against the applied stress and color coded as a function of frequency from 0.01 Hz in black to 5 Hz in red in 7 logarithmically spaced steps. The solid lines represent fits to Eq. 3.1. The blue dashed line represents the 3/2 power law characteristic of *permanently* crosslinked semiflexible polymer networks [51].

fit the differential storage modulus at each frequency to the following cross-over function:

$$K' = G \cdot (1 + \sigma/\sigma_{0,\mathrm{tr}})^{3/2}, \tag{3.1}$$

where $G(\omega)$ is the linear storage modulus and $\sigma_{0,\mathrm{tr}}$ is the characteristic stress for the onset of stiffening at a given frequency. Remarkably, although the model for the $\sigma^{3/2}$ stiffening was developed and confirmed previously for the nonlinear elasticity of *permanently* crosslinked networks, it accurately captures the nonlinear elastic response of transiently crosslinked actin networks as well. However, whereas the onset stress for nonlinearity of permanently crosslinked networks is independent of frequency [51, 71], we find that this onset systematically increases with frequency for transiently crosslinked semiflexible polymer networks [Fig. 3.3a].

In order to capture both the frequency and the stress dependence of the shear moduli, we propose a model in which we combine the transient nature of the crosslinkers with the nonlinear force-extension behavior of the semiflexible actin filaments. For permanently crosslinked networks, the storage modulus in the linear regime is dependent on the distance between crosslinkers, l_o [48]:

$$G_0 \sim \rho\kappa l_p / l_0^3, \tag{3.2}$$

where l_p is the persistence length of the filament, ρ the filament length density per vol-

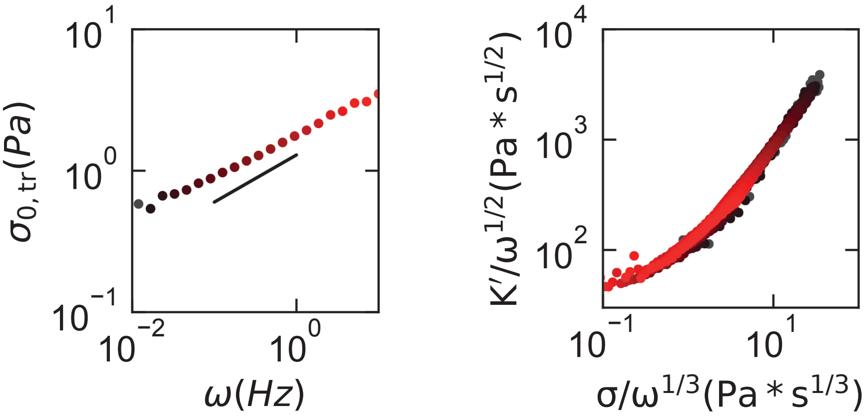

(a) **(b)**

Figure 3.3: Mastercurve behavior of the time and stress dependent viscoelastic behavior of actin networks. a) The onset stress for stiffening of actin networks follows a 1/3 power law dependence on frequency (black line), consistent with eq. 3.6. b) Stress-stiffening curves over all frequencies can be collapsed onto a single mastercurve using Eq. 3.9. The color coding is identical to [Fig. 3.2].

ume and κ the bending rigidity of the filament. In the nonlinear regime, the modulus becomes independent of the distance between crosslinkers, but is defined by the length scale beyond which bending wavelengths are suppressed due to the filament axial tension τ [39]:

$$l_\tau \sim \sqrt{\kappa/\tau}. \tag{3.3}$$

As filament axial tension increases with the applied stress, $\sigma \sim \rho\tau$, the relevant bending wavelengths become smaller and the storage modulus increases nonlinearly with the applied stress:

$$K \sim \rho\kappa \frac{l_p}{l_\tau^3} \sim \rho\kappa l_p / l_0^3 (\sigma/\sigma_0)^{3/2}, \tag{3.4}$$

where $\sigma_0 \sim \rho\kappa/l_0^2$ is the threshold stress at which the network begins stiffening as the typical filament bending wavelength decreases below the typical crosslinker distance. The important difference of transient networks compared to permanent ones is that the effective crosslinker distance increases with time as more crosslinkers unbind [37]:

$$l_{\text{tr}} \sim \omega^{-1/6} > l_0 \text{ for } \omega < \omega_{\text{off}}, \tag{3.5}$$

where ω_{off} is the crosslinker unbinding rate. As a result, the onset for stress stiffening now depends on frequency according to

$$\sigma_{0,\mathrm{tr}} \sim \rho\kappa/l_{\mathrm{tr}}^2 \sim \omega^{1/3}. \tag{3.6}$$

In order to capture both transient and non-transient regimes, we let

$$l_{tr} = l_0\left(1+\sqrt{\omega_{\mathrm{off}}/\omega}\right)^{1/3}. \tag{3.7}$$

Strictly speaking, this is correct in the asymptotic plateau ($\omega \gg \omega_{\mathrm{off}}$) and transient ($\omega \ll \omega_{\mathrm{off}}$) regime, while it is only approximate in the crossover regime at intermediate frequencies. But, we show below that Eq. 3.7 is nevertheless consistent with the experiments over the full frequency range ($10^{-2} \leq \omega \leq 10^1$).

Similarly, in order to approximate the crossover from the linear to the nonlinear regime, we let

$$l_\tau = l_{tr}(1+(\sigma/\sigma_{0,\mathrm{tr}}))^{1/2}. \tag{3.8}$$

Again, strictly speaking, this is correct for linear ($\sigma \ll \sigma_{0,\mathrm{tr}}$) and highly nonlinear ($\sigma \gg \sigma_{0,\mathrm{tr}}$) regimes, although we show below that it approximates well the behavior of actin networks over the entire experimentally accessible range of stress.

The resulting expression for K' is

$$K' \sim \rho\frac{\kappa l_p}{l_0^3}\frac{[1+(\sigma/\sigma_{0,\mathrm{tr}})]^{3/2}}{(1+\sqrt{\omega_{\mathrm{off}}/\omega})}. \tag{3.9}$$

This model accurately describes the observed trends in the nonlinear rheology of actin networks. Firstly, the theory predicts a $\omega^{1/3}$ scaling of onset stress for nonlinearity (eq. 3.6), consistent with our experimental data [Fig. 3.3a]. Secondly, using Eq. 3.9, we successfully collapse all stress-stiffening data [Fig. 3.3b]. Lastly, we use Eq. 3.9 to accurately fit the differential storage modulus as a function of frequency over all prestresses [Fig. 3.4a]. Interestingly, using ω_{off} as a free parameter, we find that the characteristic frequency decreases as the applied stress is raised [Fig. 3.5]. This result is consistent with earlier rheological measurements on networks crosslinked by ACTN4 [57], and suggests catch bonding [116] where the crosslinker unbinding rate decreases with force [38].

Strikingly, the $K \sim \omega^{1/2}$ power law predicted by Ref. [37] is only observed in the absence of prestress [Fig. 3.1c], whereas prestressed networks are significantly less frequency dependent [Fig. 3.4a,b]. We attribute the stress-dependence of the frequency spectrum to two competing nonlinearities. On the one hand, the effective crosslinker distance increases with time (Eq. 3.5), allowing for longer parts of an actin filament to freely fluctuate. On the other hand, the onset stress for stiffening decreases with time (Eq. 3.6), which suppresses filament fluctuations. Together, these two effects cause the frequency dependence to be weaker with increasing stress. We quantify this effect by fitting the data with an empirical power law $K(\sigma,\omega) = \alpha(\sigma)\cdot\omega^{\beta(\sigma)}$ commonly used in the cell rheology literature [73, 77, 111–113] and find that the exponent β decreases from 0.5 in the absence of stress to 0.1 at 8 Pa [Fig. 3.4c]. Furthermore, we find that the prefactor α increases for the loss modulus and, even more steeply, for the storage modulus as the network stiffens, such that the network becomes more solid-like with increasing stress [Fig. 3.4d].

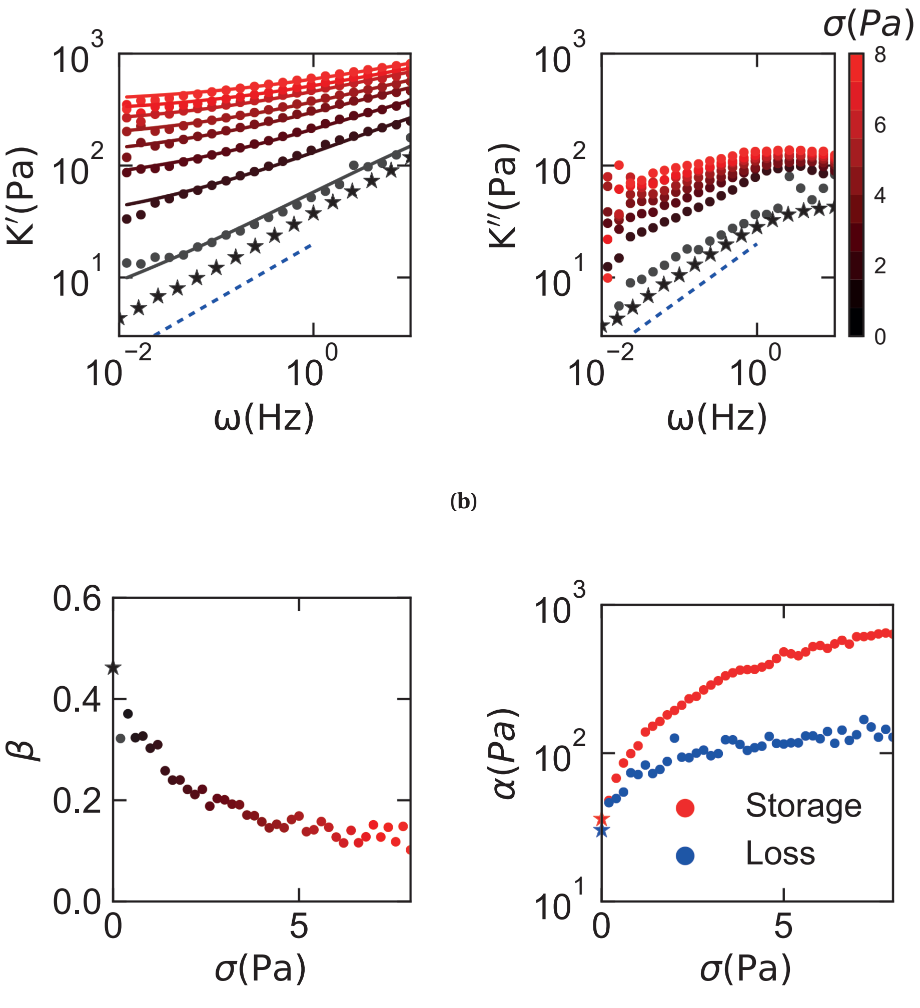

(a)

(b)

(c)

(d)

Figure 3.4: Frequency dependence of stressed networks. The differential storage (a) and loss (b) moduli of an ACTN4 crosslinked actin network are plotted against the applied frequency and color coded as a function of prestress from 0.2 Pa in black to 7.2 Pa in red with 1 Pa steps. The stars are data in the absence of prestress. The blue line represents the 1/2 power law characteristic of networks *in the absence of stress.* [37]. The solid lines represent fits to $K'(\sigma,\omega)$ according to Eq. 3.9 (see Fig. 3.5 for the fitting parameters). The frequency dependent storage and loss differential moduli are fitted between 0.01 and 1 Hz with an empirical power law $\alpha(\sigma)\cdot\omega^{\beta(\sigma)}$. The exponent β (c) and a pre-factor α (d) are shown as a function of stress.

3.3. DISCUSSION

We have investigated the dynamics of stressed semiflexible biopolymer networks that are transiently crosslinked. We find that the elastic response of such a network is well captured by a simple model that combines prior models for the linear viscoelasticity of transient gels and the nonlinear elasticity of permanent networks. Key to our model is a single length scale defined by Eqs. 3.7,3.8 that characterizes the upper limit of fluctuating wavelengths. This length depends nonlinearly on both time/frequency and stress. The resulting mechanics are different from permanently crosslinked networks [71, 109, 117], as such networks are time-independent except at very high frequencies, typically beyond 100 Hz, where the viscous drag of the fluid hampers filament relaxation [102, 118–120]. Recently, Ref. [79] proposed a model for the nonlinear response of transient semiflexible networks, but no specific relationship between the stress and the exponent governing the time dependence was predicted. While our minimal model does not include such effects, it is able to capture the stress and frequency dependence of the nonlinear elastic response. The current work goes beyond earlier work studying the linear response of transiently cross-linked semiflexible polymer networks. We find that the previously reported $K \sim \omega^{1/2}$ scaling is only apparent at small stress.

Other work on stressed dynamically crosslinked actin networks has focused on the effect of force-induced linker (un)binding [56, 57, 121], sliding of crosslinkers along filaments [122, 123] and the effect of shear-induced filament alignment [124]. While our minimal model does not include such effects, it is able to capture the stress and frequency dependence of the nonlinear elastic response. In future work, it would be interesting to include the additional microscopic effects mentioned above [56, 57, 121–123, 125], as well as to quantitatively understand the differential loss modulus, K'' , for example by using detailed network simulations of transiently connected semiflexible polymers [85].

We find that stressed semiflexible polymer networks exhibit power law dynamics with a small exponent ($\beta \sim 0.1$). Remarkably, mechanical experiments on living cells have revealed similar power law dynamics [73, 74, 77, 94, 111–113]. These mechanical properties are reminiscent of observations on a range of disordered systems close to the glass transition [80]. The soft glassy rheological properties found in cells have been phenomenologically described by assuming a broad distribution of microscopic relaxation timescales [73, 75, 76, 78, 79]. Whilst this phenomenological description can account for the experimental data [73, 75, 77, 78, 94, 111–113], it offers no insight into the microscopic processes governing these dynamics. Here we suggest that the glassy dynamics are a natural consequence of transient cross-links, combined with prestress.

Myosin motor-driven contractility is a likely source for such prestress in the cell [35, 126]. Consistent with our results, experiments on cells have revealed that the power law exponent decreases with the prestress generated by actomyosin contractility [113]. Remarkably though, whereas the reconstituted networks become more solid-like with prestress [Fig. 3.4d], mechanical experiments on cells have shown that the loss modulus increases more rapidly than the storage modulus as a function of myosin-driven tension [113]. We speculate that external stress as imposed in our rheological experiments differs from internal stresses generated by myosin motors, as motors not only cause contractility but also fluidize networks via inter filament sliding [65, 127] and severing [64, 66].

We Thank Fred Mackintosh for the development of the theoretical model. We thank William Brieher and Vivian Tang for the kind gift of purified ACTN4, Marjolein Kuit-Vinkenoog for actin purification, Bela Mulder for critical reading of the manuscript and Chase Broedersz for useful discussions.

APPENDIX

PROTEIN PURIFICATION AND NETWORK FORMATION.

The actin crosslinker human α-actinin 4 (ACTN4) was purified as described in reference [98]: Rosetta E. Coli cells were transformed to express recombinant crosslinkers with a 6xhis-tag. Induction was performed with 500 μM isopropyl β-D-1-thiogalactopyranoside for eight hours at 25^{o}C. After centrifugation at 6000 g for 15 minutes, cells were resuspended in 20 mM NaCl, 5 mg/ml lysozyme and 20 mM Hepes, pH 7.8. The cells were lysed by a freeze-thaw cycle, and centrifuged at 20,000 g for 30 min. The recombinant protein was purified from the supernatant using a QIAGEN nickel column. Next, the column was washed with 20-bed columns of 500 mM NaCl, 25 mM imidazole, and 20 mM Hepes, pH 7.8. The recombinant proteins were eluted with 10-bed volumes of 500 mM NaCl, 500 mM imidazole, and 20 mM Hepes, pH 7.8. The proteins were concentrated using a Centricon filtration device (Millipore) and purified by gel filtration in 150 mM NaCl, 20 mM Hepes pH 7.8, and 10 mM dithiothreitol (DTT) using an AKTA purifier (GE Healthcare) and a Sephadex 200 column.

Actin was purified from rabbit psoas skeletal muscle as described in reference [99] and stored at -80^oC in G-buffer (2 mM tris-hydrochloride pH 8.0, 0.2 mM disodium adenosine triphosphate, 0.2 mM calcium chloride, 0.2 mM dithiothreitol) to prevent polymerization. We used a concentration of 48 μM (2 mg/ml) for all our experiments and actin was polymerized in a buffer consisting of 50 mM KCl, 20 mM imidazole pH 7.4, 2 mM $MgCl_2$, 1 mM DTT and 0.5 mM MgATP (F-buffer). Unless otherwise mentioned, we used a crosslinker concentration of 0.48 μM to obtain a molar ratio of 1/100 crosslinker/actin and on average about 1 crosslinker per 0.5 μm of actin filament; under these conditions, networks are unbundled and isotropic as verified by confocal fluorescence microscopy [Fig. S6.17]. All chemicals were bought from Sigma Aldrich unless otherwise mentioned.

RHEOLOGY

Rheology was performed using a stress-controlled Kinexus Malvern Pro rheometer with a stainless steel 20 mm radius cone plate geometry with a 1^o degree angle. We loaded 40 μl of the ACTN4 crosslinked actin networks directly after mixing the proteins into the polymerization buffer. A thin layer of Fluka mineral oil Type A was added around the geometry to prevent evaporation, and the sample was closed off with a hood to minimize effects of air flow. Polymerization of the network was followed by applying a small oscillatory shear with a strain amplitude of 0.5 % and a frequency of 0.5 Hz for 2 h. Next, a frequency sweep was performed between 0.01 – 10 Hz, using 10 data points per decade and an amplitude of 0.5%. Afterwards, 2D stress/frequency rheology was performed [Fig. S3.6a] by varying both the prestress (0.2 – 8 Pa) and the frequency (0.01 – 10 Hz) with an amplitude of oscillation that equals 10% of the applied constant stress. Frequencies above 10 Hz could not be measured as inertial effects from the rheometer dominated the rheological response of the actin network at high frequencies. The prestress was increased from 0.2 Pa to 8 Pa with 0.2 Pa intervals. At every step in prestress, a superimposed small amplitude oscillation was applied with a frequency of oscillation that started at a frequency of 10 Hz for every prestress and was decreased to 0.01 Hz in 20 logarithmically spaced steps using 4 cycles per frequency. After reaching 8 Pa, the prestress was decreased with 0.2 Pa intervals, again performing a frequency sweep at every prestress. All experiments were performed at $T = 298$ K.

In the main text, all figures show data from the decreasing sweep as the viscoelastic flow due to the prestress was smaller for the decreasing sweep than for the increasing sweep [Fig. 3.6b]. However, we show that similar trends are observed in the upward stress/frequency sweep [Fig. 3.7]. Furthermore, the stress/frequency sweep data in the main text [Fig. 3.2] and [Fig. 3.4a,b] only show a representative selection of the experimental data to preven graphs from becoming crowded, whereas the full data sets are shown in [Fig. S3.7].

FITTING PROCEDURE

We fit the differential storage modulus with Eq. 3.9 from the main text using a least square fitting algorithm in two steps. In the first step, we fit the data with all parameters (pre-factor, characteristic frequency and an onset stress of stiffening) fixed over the entire stress/frequency range. In the second step, we refine the fit by allowing for a stress-dependent characteristic frequency, using the pre-factor and onset stress of stiffening from the first step. Note that the characteristic frequency obtained in this way is larger than the highest probed frequency over the full stress range [Fig. S3.5]. Therefore, the values should be interpreted with caution as the absolute values are sensitive to the choice of pre-factor and onset stress of stiffening. However, the decrease in characteristic frequency with prestress shown in [Fig. S3.5] should be robust.

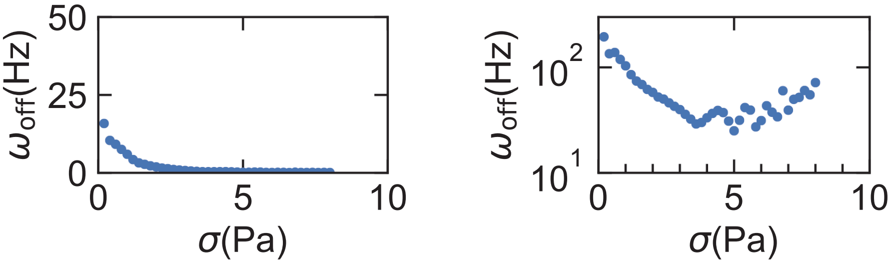

(a) **(b)**

Figure 3.5: Characteristic frequency indicative of the crosslinker unbinding rate as a function of the applied stress. The differential storage modulus was fit at every prestress with Eq. 9, using the characteristic frequency as a free parameter. Data are shown on a lin-lin (a) and log-lin scale (b). The pre-factor and onset stress of stiffening (σ_0, not $\sigma_{0,\mathrm{tr}}$) were fixed at resp. 748 Pa and 11.8 Pa.

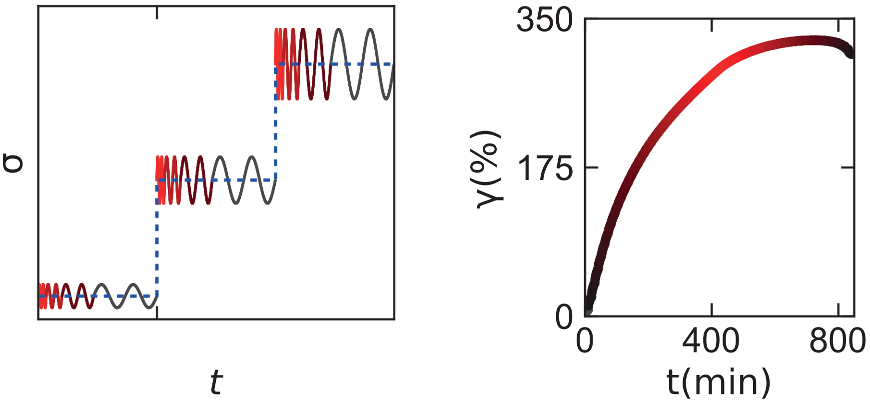

(a) **(b)**

Figure 3.6: Stress protocol and creep. a) Schematic of the 2D stress/frequency protocol. We apply a prestress (dashed blue line) with a superimposed small amplitude oscillation, varying both the frequency and prestress in time. Using this protocol, we measure the differential storage and loss moduli. The frequency is color coded. b) During the 2D stress/frequency sweep, the actin network is under continuous stress and therefore viscoelastically flows. Here we plot the strain as a function of time, with $t = 0$ corresponding to the start of the sweep. The prestress is color coded from 0.1 Pa in black to 8 Pa in red. After approximately 400 min, a full 2D scan is completed and the stress is ramped down to measure the reversibility of the stiffening (400 – 800 min).

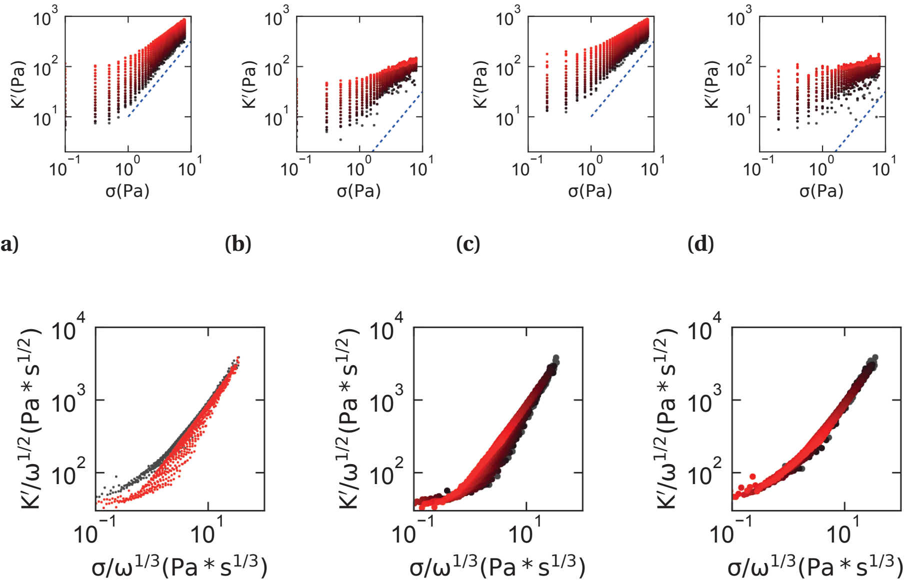

(a) (b) (c) (d)

(e) (f) (g)

Figure 3.7: Comparison of upward and downward 2D stress/frequency sweeps. The differential storage (a,c) and loss (b,d) moduli for the upward (a,b) and downward (c,d) stress sweep. The dashed line shows the 3/2 power law expected for permanently crosslinked networks. e) Using Eq. 9, we collapse the upward (red) and downward (black) curves - showing that the stiffening and frequency dependence are both insensitive to the sample history. The individual upward (f) and downward (g) curves are color coded as a function of frequency similar to [Fig. 3.3] from the main text.

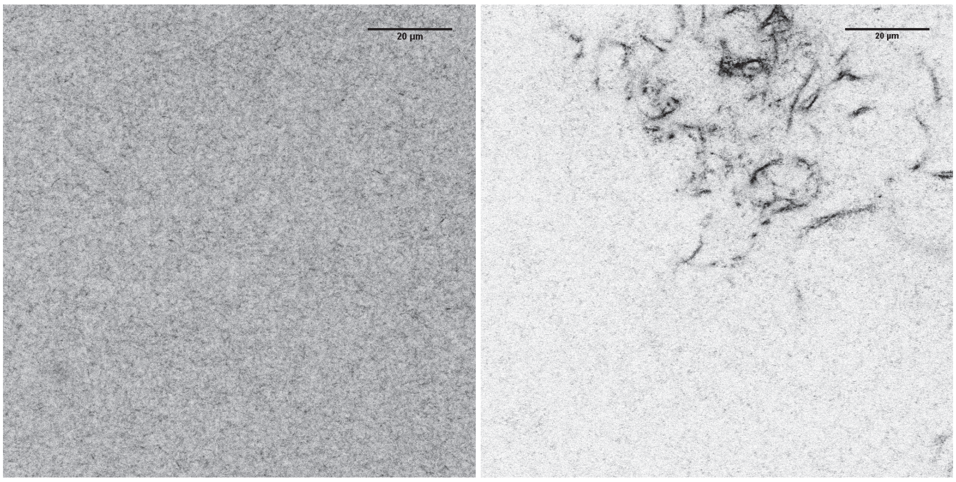

(a) (b)

Figure 3.8: Confocal fluorescence images of ACTN4 crosslinked actin networks a) At a 1:100 ACTN4:actin molar ratio, the concentration used for all experiments in this manuscript, an isotropically crosslinked actin network is observed with no structure above the diffraction limit. b) For comparison, actin bundles were observed at a 1:25 ACTN4:actin molar ratio. The color coding was inverted for both images to improve the visual contrast between bundles and background. Scale bars are 20 μm.

4

CRACK INITIATION IN VISCOELASTIC MATERIALS

In viscoelastic materials, individually short-lived bonds collectively result in a mechanical resistance which is long-lived but finite, as ultimately cracks appear. Here we provide a microscopic mechanism by which a critical crack length emerges from the nonlinear local bond dynamics. Due to this emerging length scale, macroscopic viscoelastic materials fracture in a fundamentally different manner from microscopically small systems considered in previous models. We provide and numerically verify analytical equations for the dependence of the critical crack length on the bond kinetics and applied stress.

4.1. INTRODUCTION

Liquids cannot fracture, but solids can. We consider the intermediate case: viscoelastic materials. These materials are made of filaments or particles interconnected by short-lived bonds. This design theme of transient networks is commonly used in both natural and man-made materials such as cytoskeletal polymer networks in cells [37], physical gels [128], associative and telechelic polymers [129], and colloidal gels [130].

The molecular dynamics of transient networks lead to interesting macroscopic mechanics: at times shorter than the bond lifetime the material behaves like a solid [37], while on longer time scales the bonds reorganize and the material deforms viscoelastically [37, 122, 131]. As a result, transient networks are much more deformable than permanent networks [132]. However, viscoelastic materials can resist mechanical stress only for a limited time, after which the system suddenly loses its mechanical percolation, a process which is known as fracturing [129, 133–135]. This raises the question how we can design transient networks such that the robustness against stress is optimized, which requires an understanding of the mechanism by which transient networks fracture.

Fracturing of viscoelastic materials is often explained by the Griffith theory of crack stability in brittle solids [99, 129, 133, 136–138]. The Griffith theory predicts that beyond a critical stress, initial defects will grow into macroscopic cracks as the elastic energy released by the crack dominates the surface energy required for separation [139]. This thermodynamic model provides a criterion for stability, but cannot be used to describe the dynamic process of stochastic crack initiation [140]. Moreover, this framework was originally developed for solids, and assumes defects are either static or growing. This assumption is clearly invalid for viscoelastic materials, as defects are not static entities but instead continuously appear and heal [141]. Therefore, viscoelastic materials require a framework which takes into account the reversible bond dynamics.

The seminal work of Bell on cellular adhesion provides such a framework of reversible bond dynamics under force [142], and has received considerable attention in studying small-scale systems such as protein clusters which provide cellular adhesion [143, 144], fracturing of a single colloidal strand [134] and protein unfolding [145].

In all of these works, force is assumed to be homogeneously distributed across all bonds, which appears to be a realistic assumption for microscopically small systems. Contrarily, in the context of viscoelastic materials, theoretical [146, 147] and experimental work on both synthetic gels [148] and biopolymer networks [149] has revealed non-affine deformations upon application of global stress [150]. Indeed, imaging of various networks under stress showed inhomogeneities of the local force which are strongly correlated in space [125, 151, 152]. These inhomogeneities might be negligible when considering bulk properties such as the average bond lifetime under stress [54, 153], but likely play a key role in crack initiation. In situ imaging of stressed viscoelastic materials revealed that fracturing occurs via well-defined cracks [129, 136, 154, 155] rather than via the homogeneous degradation expected from the Bell model [54, 142–145, 153, 156], suggesting local rather than global load sharing. At which length scale does the global load sharing assumption become inaccurate? And what determines the fracturing properties of a system of reversible bonds under load beyond this length scale?

To answer these questions we developed a minimal model that includes reversible bond dynamics (figure 4.1a) in the simplest possible ’material’ that is capable of exhibiting spatial inhomogeneity required for studying crack initiation: bonds distributed over a 1D-space, subject to tensile load. The experimental analogue in three-dimensional networks is a shear load as a constant tensile load would cause continuous thinning [136]. To account for inhomogeneous load sharing, we assume a force distribution that depends on the local bond spacing (figure 4.1b). We show that this minimal model system exhibits spontaneous crack initiation and subsequent fracture, in a manner that is consistent with experimental observations in wide range of viscoelastic materials [129, 136, 154, 155]. We verify our results by comparison with a mechanical model. We study the process of crack initiation in more detail by locally ’ablating’ bonds (figure 4.1c), which reveals a critical crack length beyond which fracturing occurs. We provide analytical equations describing the process of crack initiation on basis of the nonlinear bond dynamics, and predict the dependence of the critical crack length on both bond properties and applied stress. Our work reveals that microscopic viscoelastic materials smaller than this typical crack length behave qualitatively different from macroscopic viscoelastic materials.

4.2. METHOD

We initialize a one-dimensional (1D) network with N equally spaced binding sites using periodic boundary conditions, each bond having a probability K to start in a closed state. Next we model the dynamics of the bonds with a kinetic Monte Carlo scheme [157] using the following bond dynamics:

$$K = \frac{k_{\text{on}}}{k_{\text{on}} + k_{\text{off},0}} \tag{4.1}$$

where k_{on} is the rate of bond closing and $k_{\text{off},0}$ the rate of bond opening in the absence of force (figure 4.1a). We normalize time by the on-rate, k_{on}. Note that we do not introduce a force-dependence in k_{on}, as binding sites could both appear and disappear as a function of shear stress. Moreover, including a force-dependence in the on-rate would introduce an extra parameter in the model, without qualitatively changing any of our results. The off-rate increases exponentially with the applied force f on the bond in keeping with the Bell model [142]:

$$k_{\text{off}}(f_i) = k_{\text{off},0} \cdot \exp(\frac{f_i}{f_{1/\text{e}}}) \tag{4.2}$$

where $f_{1/\text{e}}$ is the force where the off-rate has fallen to $1/\text{e}$ of $k_{\text{off},0}$. We calculate the force per bond f_i via

$$f_i = \alpha_i \cdot \sigma \tag{4.3}$$

where σ is the stress on the system and α is a yet to be defined stress intensity factor per bond. In global load sharing, the applied stress is equally divided over all bonds. To investigate the effect of inhomogeneous force distribution as present in any network under stress [125, 151, 152], we investigate a local load sharing model. In this model, we assume that the force distribution is dependent on the distance l_i of a bond to its nearest

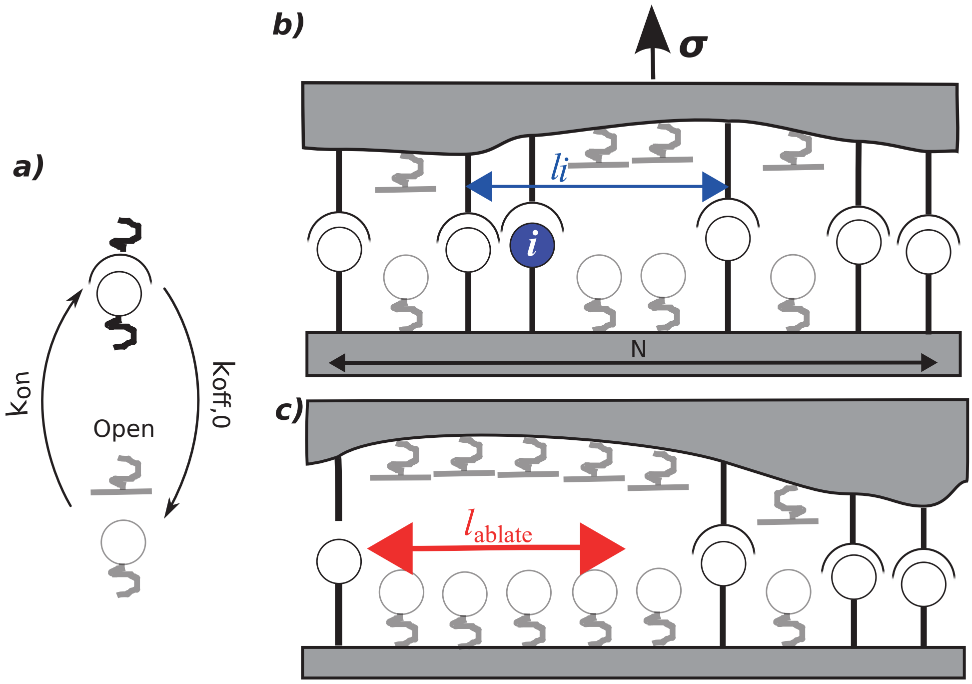

Figure 4.1: Schematic of model a) Bonds switch from an open to a closed state with rate k_{on} and reverse with a rate of $k_{\text{off},0}$ in the absence of force. b) Bonds in a closed state share an applied load σ (the force normalized by the system size), where the load distribution depends on the distance l_i from bond i to its nearest neighbors. c) We perform bond ablation experiments by opening all bonds in l_{ablate} adjacent positions to investigate the critical length required for triggering fracturing. Periodic boundary conditions are used to prevent edge effects from influencing the results.

neighbor on both sides (figure 4.1b). Explicitly, we define a stress intensity factor α on a closed bond at site i by:

$$\alpha_i = \begin{cases} N \cdot \frac{l_i}{\sum_i l_i} & \text{Local} \\ \frac{N}{\sum_i n_i} & \text{Global} \end{cases} \tag{4.4}$$

where n_i equals 1 when the bond is closed and 0 when the bond is open. Note that in both modes of load sharing the total amount of force is independent of the bound fraction and normalized by the system size, $\frac{\sum_i f_i}{N} = \sigma$. We normalize the applied stress by the bond force sensitivity $f_{1/e}$. After calculating the force on all bonds, we employ a kinetic Monte Carlo step to either open or close a bond stochastically. We repeat this process of stochastic bond removal/addition until all bonds are removed.

4.3. RESULTS

As shown in figure 4.2a, the fraction of closed bonds fluctuates over time, until it drops precipitously to zero at a certain moment that we denote as the rupture time. The rupture time is exponentially distributed - indicative of the stochastic nature of fracturing [158]. To test the sensitivity of the average rupture time to the applied stress, we perform simulations at a fixed network size and fixed bond affinity for different levels of stress ($N = 20$, $K = 0.9$, $\sigma = 0.5...2$). For both local and global load sharing, we find that the average rupture time shows two distinct regimes with a transition around $<t_{\text{rupt}}>\approx 1$ (figure 4.2b). As we will explain later on, these regimes correspond to a metastable network at low stress and an unstable network at high stress. Importantly, networks with local load sharing are markedly less robust than globally load sharing networks, with smaller average rupture times at all stresses.

To test how the system size influences the average rupture time, we perform simulations for networks with N varying between 5 and 100 (figure 4.2c). In case of global load sharing, we see that the average rupture time monotonically increases with system size, as the relative fluctuations of the fraction of closed bonds ($\frac{\sum_i n_i(t)}{N}$) decreases [134, 142–144]. In case of local load sharing, we find similar rupture times as compared to globally load sharing networks for small N. But strikingly, beyond a critical length (around $N = 12$ for these conditions), we find that only in case of local load sharing the rupture time decreases with increasing system size, according to $<t_{\text{rupt}}>\sim N^{-1}$ (inset of figure 4.2c). This dependence suggests a constant crack initiation rate for every 12 bonds at this particular stress. Indeed, kymographs of simulations using local load sharing reveal that fracturing proceeds via cracks rather than homogeneous degradation (figure 4.2d). The relevance of our model is limited to crack initiation, the rate-limiting step in rupturing [159], as the fracture energy during crack propagation depends on system-specific physical processes, such as solvent dynamics and polymer disentanglement [160, 161].

To understand what sets the critical length for crack initiation as observed in figure 4.2c, we performed 'ablation experiments' (figure 4.1c): first we equilibrate the network under stress, next we remove all bonds in l_{ablate} adjacent positions, then we study whether bond ablation triggered network fracturing. We chose the system size $N=l_{\text{ablate}}\cdot 10$, such that the system is large compared to the number of ablated bonds, yet small enough to allow for equilibration without spontaneous crack initiaton. Figure 4.3a shows how fracturing becomes more likely upon increasing the ablation size l_{ablate}, and that the required ablation size l_{ablate} to initiate fracturing decreases with the applied stress σ. Figure 4.3b shows that an increase of bond affinity K increases the critical ablation size l_{ablate} required for triggering fracture.

To quantitatively understand the ablation data, we define crack length L as the largest bond distance l_i in the system. In case of global load sharing, the force on bonds at the edge of the crack stays independent of L as long as $L \ll N$, so ablation does not induce fracture. By contrast, in case of local load sharing, the force on the bond at the edge of the crack is $f=\sigma\cdot L\cdot 1/2$ (the factor $1/2$ is because the load on the hole is shared by the bonds at both ends). Thus, k_{off} exponentially grows with the crack size due to a linearly increasing force, whereas the chance of rebinding increases only linearly due to a larger area in which rebinding can occur. As a result, for large enough l_{ablate}, bond unzipping will occur for any system under stress.

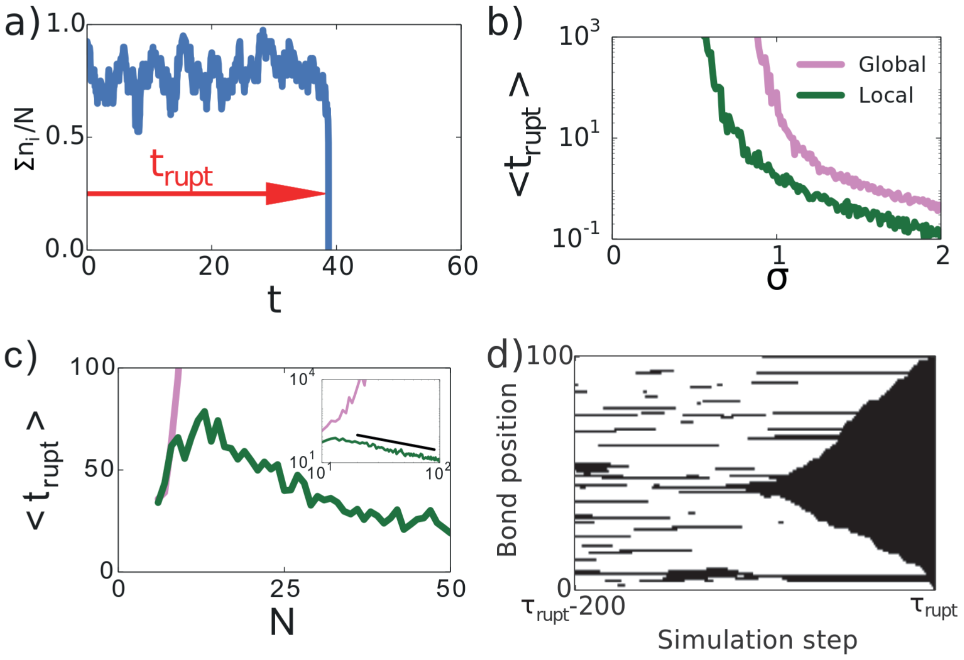

Figure 4.2: Stochastic rupture of simulated 1D transient networks subject to a mechanical stress. a) Typical example of the fraction of closed bonds in time upon application of stress, after $t = t_{\text{rupt}}$, spontaneous fracture occurs ($K = 0.9$, $N = 20$, $\sigma = 0.7$, global load sharing). b) Stress dependence of rupture time. Although quantitatively different, global and local load sharing show qualitatively similar behavior with two exponential regimes with a cross over at around $<t_{\text{rupt}}>\approx 1$ ($K = 0.9$, $N = 20$). c) The system size dependence of the rupture time reveals a qualitative difference between global and local load sharing: whereas the rupture time increases with system size for global load sharing, local load sharing shows an optimum in strength at a well-defined system size ($K = 0.9$, $\sigma = 0.7$). Inset: same data on a log-log scale, showing that after a critical system size $<t_{\text{rupt}}>\sim N^{-1}$ for local load sharing. d) Kymograph of crack initiation under local load sharing (white=closed, black=open) clearly reveals how bond opening proceeds via a well-defined crack. The x-axis shows simulation step rather than time, as the crack propagation is orders of magnitude faster than the crack initiation (figure 4.2a). Note that time is normalized by k_{on}.

We are interested in the length L_{unstable} at which the crack becomes unstable. As a first order approximation, we can find the fixed points of crack length $\overset{*}{L}$ by calculating the length at which the rates of bond opening and closing are equal (figure 4.4a):

$$2 \cdot k_{\mathrm{off}}(1/2 \cdot \sigma \cdot \overset{*}{L}) \approx k_{\mathrm{on}} \cdot \overset{*}{L} \tag{4.5}$$

This condition is met at the average bond distance at equilibrium, L_{stable}, and the bond distance at the unstable point, L_{unstable}:

$$L_{\mathrm{stable}}(\sigma, K) \approx 2 \cdot \frac{W_0(-\sigma \cdot (\frac{1}{K} - 1))}{-\sigma} \tag{4.6}$$

$$L_{\mathrm{unstable}}(\sigma, K) \approx 2 \cdot \frac{W_{-1}(-\sigma \cdot (\frac{1}{K} - 1))}{-\sigma} \tag{4.7}$$

where W is the Lambert W function with W_0 the main branch and W_{-1} the second branch [162]. Note that the network transitions from metastable to unstable at L_{stable}=L_{unstable} (seen as a change in slope in figure 4.2b at around $<t_{\mathrm{rupt}}>\approx 1$). For local load sharing, the transition from a metastable to an unstable network occurs beyond a critical bond-to-bond distance L_{unstable}, whereas for global load sharing this transition occurs beyond a critical fraction of open bonds and therefore explains the continuous increase of rupture time as function of time [134, 142–144].

To test equation 4.7, we show in figure 4.4b that all ablation data can be successfully collapsed onto a single master curve using a normalized ablation size $\frac{l_{\mathrm{ablate}}}{L_{\mathrm{unstable}}}$. To compare equation 4.7 with both the ablation data and the typical length scale observed in figure 4.2b, we first define a critical ablation length, l_{crit}, which we obtain by fitting the size dependence of the rupture probability ϕ_{rupt} to a sigmoidal function ϕ_{rupt}=$\frac{1}{1+e^{-l_{\mathrm{crit}}-l_{\mathrm{ablate}}}}$ at each applied stress and at bond affinity $K = 0.9$. We can now combine the critical ablation length l_{crit} from figure 4.3a with the optimal system size N found in figure 4.2c and conclude that all these data are well-described by equation 4.7 (figure 4.4c).

4.4. DISCUSSION

Up to now, theoretical work on transient network fracturing has been limited to the assumption of global load sharing [134, 142–144]. We find that $< t_{\mathrm{rupt}} >$ is insensitive to this assumption for microscopic systems. However, fracturing of macroscopic system follows fundamentally different rules, in which the notion of local load sharing becomes important. The length scale separating microscopic from macroscopic materials depends on K and σ, and ranges from tens of bonds up to arbitrarily large values (equation 4.7). Our study investigates the idealized limit of fully localized load sharing, but we observe similar behavior of a typical fracture length when the load distribution is simulated via a mechanical model [158, 163].

Our model predicts features which are different from global load sharing, but consistent with experimental observations on a wide range of viscoelastic materials. First, rupturing of macroscopic viscoelastic materials proceeds via spontaneous crack initiation, different from the homogeneous failure predicted by global load sharing models [134, 142–144]. This prediction is borne out by experimental observations of a wide

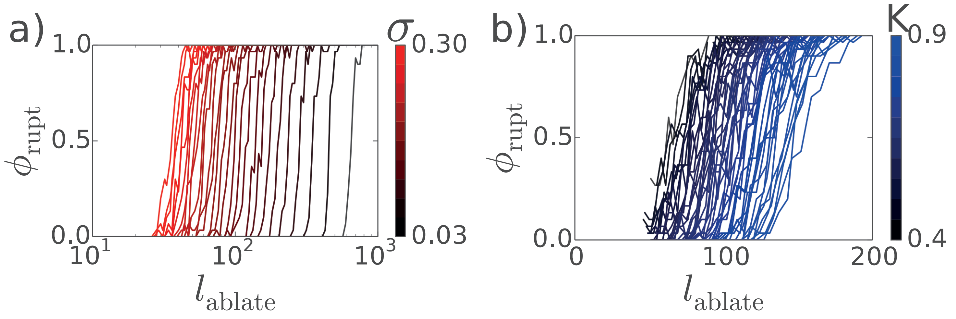

Figure 4.3: Characterization of critical crack length in local load sharing Ablation experiments were performed by first equilibrating the system under stress until $t = 1$, next bonds were ablated: $n_i = 0$ for i=0...l_{ablate}. After the ablation, the network was studied up to $t = 2$. This experiment was repeated 30x per condition, and the fraction of observed ruptures ϕ_{rupt} was recorded. We plot the fraction of observed ruptures ϕ_{rupt} as a function of the ablation size l_{ablate} for different values of a) applied stress σ at $K = 0.9$ or b) bond affinity K at $\sigma = 0.1$. Control ablation experiments using the same parameter with global load sharing never showed fracturing.

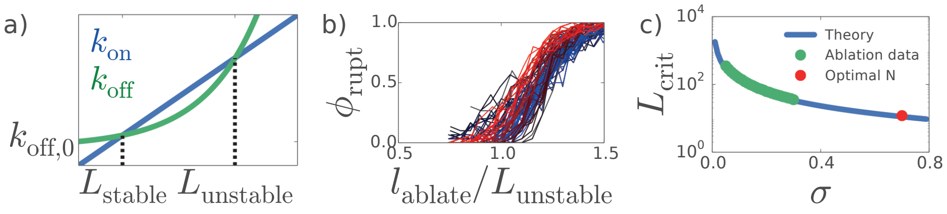

Figure 4.4: Comparison between theory and simulation a) As a function of crack size, the on-rate increases linearly, whereas the off-rate increase exponentially. As a result, the crack becomes unstable after L_{unstable}. b) All data from figure 4.3 can be collapsed obtained onto a single master curve by normalizing according to $l_{\mathrm{ablate}}/(L_{\mathrm{unstable}}(\sigma, K))$. c) Equation 4.7 quantitatively predicts both the critical length for ablation, and the width at which the maximal rupture time is observed in figure 4.2.

range of viscoelastic materials [129, 136, 154, 155]. Second, the model of global load sharing predicts that the rupture time strongly increases with the system size. As a result, delayed fracturing ($<t_{\text{rupt}}> \gg k_{\text{on}}$) would only be experimentally observable very close to the critical stress for any macroscopic system. Instead, delayed fracture is experimentally observed for many different viscoelastic materials over a wide range of stresses [129, 133–135]. We find that in case of local load sharing, the dependence of $< t_{\text{rupt}} >$ on σ does not diverge upon increasing system size N. Thus, our model for the first time explains why delayed fracturing is readily observable on laboratory timescales over a wide range of stresses in; experiments.

The model makes several concrete predictions that can be tested experimentally by applying shear stress on viscoelastic materials. Firstly, we predict that the average rupture time measured at constant stress will be inversely proportional to the system size (figure 4.2c) as the crack initiation rate is constant per volume. Secondly, the presence of a critical crack length can be measured directly by performing laser ablation on viscoelastic materials under stress, a technique that is common in biophysical studies of cell and tissue tension [23]. Thirdly, the dependence of the critical crack length on the applied stress and bond kinetics (Equation 4.7) can be tested experimentally. The bond kinetics can for instance be experimentally controlled by changing the temperature in cross linked actin networks [164] or salt conditions in polyelectrolyte gels [165].

Previous simulations of viscoelastic materials have only considered systems of 10-100 bonds in width [137, 166–168] - small compared to typical crack lengths as found in our study and therefore significantly less sensitive to local load sharing than macroscopic materials used in experiments [129, 133–135]. Future computational work should focus on networks larger than the typical crack length to investigate how microscopic details not addressed in our simple 1D model (e.g. polymer length [33] or network fractality [169]) influence the dynamics of bond inhomogeneity in two [137, 166, 167] or three dimensions [168] as for traditional solids it is well-known that crack stability depends on the 3D shape of defects [139].

Our framework for understanding the crack initiation process in viscoelastic materials can be used to rationally design more robust materials. We have considered evenly distributed bonds. For future work, it would be interesting to investigate the effect of inhomogeneity under local load sharing. It is interesting to note that cellular adhesion proteins are not randomly distributed but clustered with a well-defined size [22]. Simulations have shown that an intermediate degree of clustering is optimal for preventing fracturing [170, 171], although the nature of this optimum remained poorly understood. We speculate that this optimal clustering density is related to the critical length scale for crack initiation and that this strategy of clustering bonds is an interesting design principle for synthetic materials.

We thank Giorgio Oliveri and Bas Overvelde for the development of the Finite Element Analysis. We thank Pieter Rein ten Wolde, Chase Broedersz, David Brueckner and Mareike Berger for fruitful discussions.

APPENDIX

CRACK INSTABILITY CRITERION

In the main text we derive a criterion for the size at which cracks become unstable (equation 7). Here we present the derivation in more detail. A full description of the crack dynamics $\frac{dL}{dt}$ is analytically untractable. However we can approximate the fixed points $\overset{*}{L}$, where $\frac{d\overset{*}{L}}{dt} = 0$, by considering the two types of events which contribute directly to the crack dynamics: unbinding of either of the two bonds at each edge of the crack, and rebinding of any of the bonds within the crack. Following equation 5.2, the rate k_{edge} at which unbinding at the edge occurs is:

$$k_{\text{edge}} = k_{\text{off},0} \cdot \exp(\frac{f_i}{f_{1/\text{e}}}) \approx k_{\text{off},0} \cdot \exp(\frac{L \cdot \sigma}{f_{1/\text{e}}}) \tag{4.8}$$

Note that this solution is only approximate, as we ignore the distance from the bonds at the edge of the crack to their nearest neighbor. Next, we compute the rate k_{center} at which binding occurs anywhere within the crack:

$$k_{\text{center}} = k_{\text{on}} \cdot L \tag{4.9}$$

We now ask at which crack length the rate of unbinding at the edge equals the rate of rebinding at the center:

$$k_{\text{on}} \cdot \overset{*}{L} \approx k_{\text{off},0} \cdot \exp(\frac{\overset{*}{L} \cdot \sigma}{f_{1/\text{e}}}) \tag{4.10}$$

As $K = \frac{k_{\text{on}}}{k_{\text{on}} + k_{\text{off},0}}$ (eq. 4.1) and $k_{\text{on}} = f_{1/\text{e}} = 1$ due to normalization, the equation simplifies to:

$$-\sigma \cdot (1 - K) \approx -\sigma \cdot \overset{*}{L} \cdot \exp(-\sigma \cdot \overset{*}{L}) \tag{4.11}$$

which we can solve using the Lambert W function [162], where the Lambert W function represents the branches of the inverse relationship of the function $f(z) = z \cdot \exp(z)$, so $z = W(z \cdot \exp((z))$. Solving this equation using the Lambert W function with $f(z) = -\sigma \cdot (1 - K)$ and $z = -\sigma \cdot \overset{*}{L}$ results in equation 4.6 and 4.7 for resp. the first (stable) and second (instable) branch of the Lambert W function [162].

MECHANICAL MODEL

To validate the behavior of cracks in viscoelastic materials obtained with the local load sharing assumption, we implemented a 2D mechanical model (figure 4.5) based on Finite Element Analysis (FEA) [163]. The transient bonds, modeled by a linear elastic material with a Young's modulus E and Poisson's ratio ν, are modeled as elastic bodies fixed

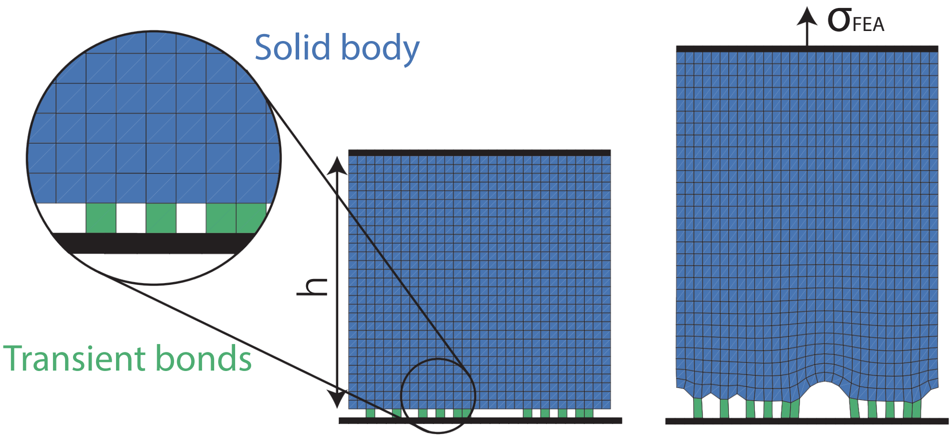

Figure 4.5: Finite element model Finite element model representation of an elastic body (blue) of total thickness h with random distribution of bonds (green) at rest (left) and stretched (right). The deformation, due to the applied force σ_{FEA} on the elastic body, is exaggerated for clarity.

at their bottom and attached to an upper body with the same material properties. Both the bonds and the elastic body are discretized using bi-linear square elements consisting of four nodes. The elastic body consists of $h \cdot N$ elements, where h is the height of the elastic body expressed in terms of the in number of elements and N is the number of bonds. Periodic boundary conditions are applied to the left and right boundaries. To apply tension to the bonds, a vertical displacement is applied to the upper boundary of the solid part, until a force σ_{FEA} is reached. A Monte Carlo scheme similar to the one used for the local load sharing model is applied to determine the transient behavior of the bonds, using equation 5.2 and 4.3, and we define the stress intensity factor value α_i for FEA as:

$$\alpha_i = \frac{U_i}{\sum_i U_i} N \tag{4.12}$$

where U_i is the bonds' elastic strain energy density which can be found by integrating the stress vector on the bond $\{\boldsymbol{s}\}_i$ for the strain vector $\{\boldsymbol{e}\}_i$ according to:

$$U_i = \int \{\boldsymbol{s}\}_i^T \{d\boldsymbol{e}\}_i = \frac{1}{2}\{\boldsymbol{s}\}_i^T \{\boldsymbol{e}\}_i = \frac{1}{2}\left[s_{xx} \quad s_{yy} \quad s_{xy}\right]_i \begin{bmatrix} e_{xx} \\ e_{yy} \\ e_{xy} \end{bmatrix}_i \tag{4.13}$$

Figure 4.6 shows how the elastic body redistributes the applied force on the bonds. Importantly, we observe a stress intensity distribution for FEA that is comparable to that of the local load sharing assumption using the settings of $h = N$ and $E_{\text{body}} = E_{\text{bond}}$. For future work it will be interesting to vary h and/or $E_{\text{bond}}/E_{\text{body}}$ and test the effect on the stress distribution and subsequent fracturing behavior.

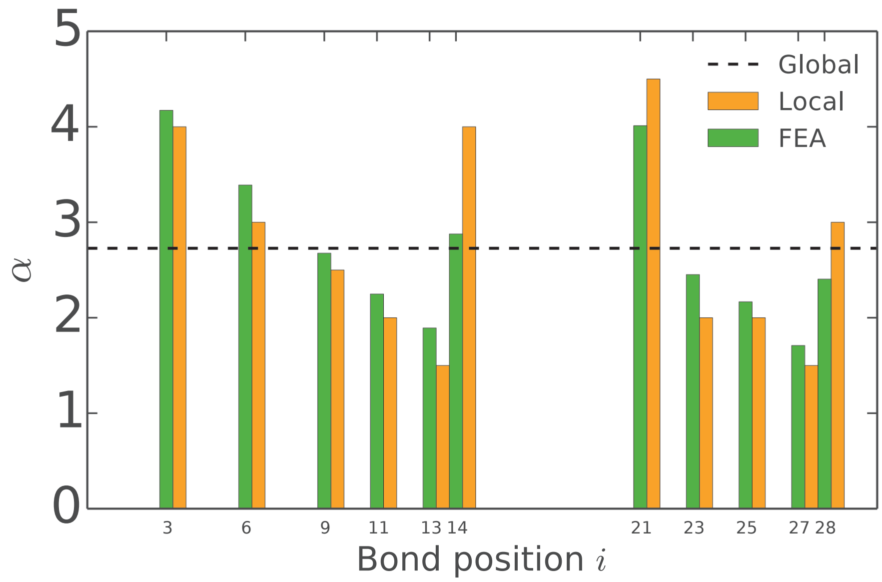

Figure 4.6: Comparison of load distribution Stress intensity factor comparison of different modes of load sharing (global, local, FEA) for the bond distribution shown in Figure 4.5.

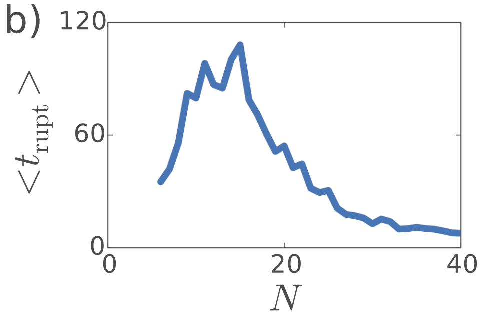

Figure 4.7: FEA verifies main qualitative difference between local and global load sharing Unlike global load sharing but similar to local load sharing [Fig. 4.2c], the average rupture time in FEA is peaked for intermediate system size N.

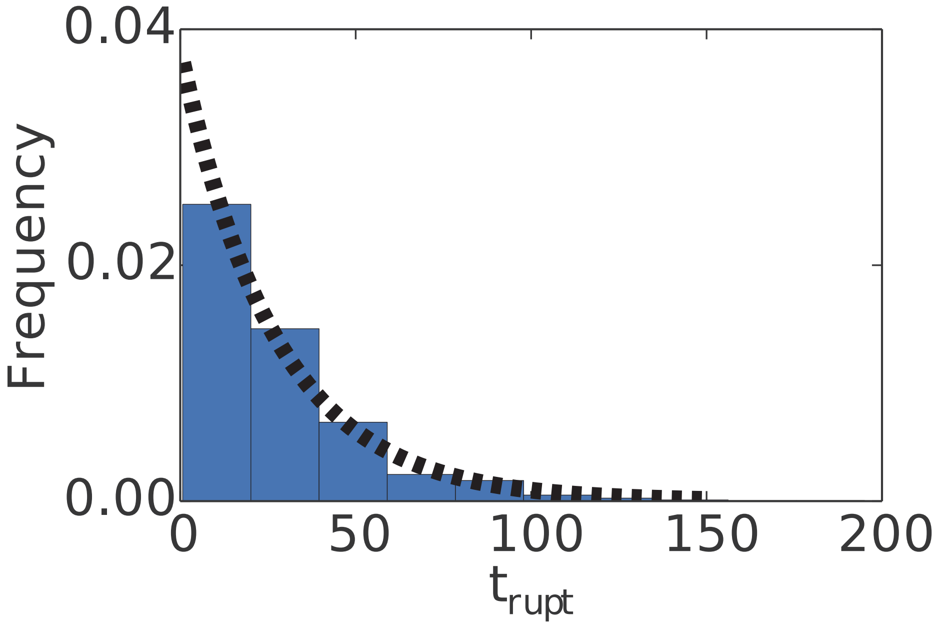

Figure 4.8: Rupture times are exponentially distributed We performed fracturing simulations under local load sharing for 1D networks (see figure 4.1) using identical parameters ($\sigma = 0.7$, $K = 0.9$, $N = 20$, 1000 repeats) and recorded τ_{rupt}. The distribution of rupture times is exponential, suggesting a stochastic process.

5

CROSSLINKER MOBILITY WEAKENS TRANSIENT POLYMER NETWORKS

Transient networks comprised of polymers connected by short-lived bonds are a common design theme for both biological and synthetic materials. Transient bonds can provide mechanical rigidity, while still allowing for viscoelastic flows on timescales longer than the bond lifetime. In many biological polymer networks such as the actin cytoskeleton, the short-lived bonds are formed by accessory proteins that diffuse away after unbinding. By contrast, bonds in synthetic networks, such as the pendant groups of telechelic polymers, can only rebind in the same location. Using a recently developed theoretical model of the fracturing of viscoelastic materials, we here investigate the effect of linker mobility on the bond dynamics of a network under stress. We find that although mean field properties such as the average bond linker lifetime are barely affected by bond mobility, networks cross linked by mobile bonds fracture more readily due to 'leaking' of linkers from crack areas to less stressed regions within the network. We propose a theoretical model to describe the redistribution of mobile linkers, which we validate by simulations. Our work offers insight into a potential trade-off that cells face, between fracture strength versus the modularity and tight dynamic control offered by mobile linkers.

5.1. INTRODUCTION

Transient polymer networks are connected by individually short-lived bonds, which collectively result in a long-lived mechanical resistance by distributed load sharing [159]. This design principle is the basis of viscoelastic materials: the reversible bond dynamics allow the network to flow whilst maintaining mechanical integrity [131]. Furthermore, transient networks are self-healing due to the reversibility of unbinding [172] and the sensitivity of the bond dynamics to a range of external conditions makes these materials stimuli-responsive [54, 164, 165]. Due to the viscoelastic flow, transient networks are much more deformable than permanent networks [132]. However, viscoelastic materials can resist mechanical stress only for a limited time, after which the system suddenly loses its mechanical percolation, a process which is known as fracturing [129, 133–135]. Crack initiation of viscoelastic materials occurs stochastically [129, 159] due to fluctuations in the local density of bound linkers [141, 173], which eventually results in fracture due to rapid crack propagation [160]. In order to understand the fracturing behavior of transient networks, one needs to understand the linker dynamics.

Transient networks can be divided in networks bound by immobile or by mobile linkers. Mobile linkers can be found in many biological systems. A well-studied example is the actin cortex, which consists of a network of actin filaments connected by actin-binding proteins [37]. These actin binding proteins can freely diffuse after unbinding. Similarly, cells use integrins [174] and cadherins [175] for cell-matrix and cell-cell adhesion [22], respectively. These adhesive proteins diffuse in the plane of the membrane after unbinding. By contrast, examples of networks connected by immobile linkers are colloidal gels connected by pendant groups [176] and adhesive polymer networks [177], such as hydrogen-bonded associative polymers [178], telechelic polymers [129], ionomers [179] and polyelectrolyes [155]. A biological example of immobile linkers can be found in fibrin blood clots, where fibrin forms fibers with pendant sticky groups which unbind upon mechanical loading [180].

Both mobile and immobile linkers result in transient networks, but only mobile linkers allow for linker rebinding in new locations of the network. This linker mobility allows for bond redistribution upon the application of mechanical stress [62, 124]. Due to crack-induced stress localization [139] and subsequent force-induced linker unbinding [142], bond redistribution is most pronounced around cracks. We therefore wonder what is the effect of linker mobility on the mechanical strength of a material?

In order to investigate the effect of bond mobility on network strength, we use a model which we recently developed in the context of crack initiation in viscoelastic materials [173]. This model includes force-sensitive reversible bonds that are subjected to an external stress. Different from previous transient network models [54, 142–145, 153, 156], this model acknowledges that the applied stress is distributed inhomogeneously over the bonds on basis of their spatial distribution [125, 151, 152]. As a result of this inhomogeneous force distribution, cracks stochastically initiate and subsequently propagate due to fluctuations in the local bond density [173]. However, this model was specific for the case of immobile linkers. We here extend the model, allowing us to include the effect of bond mobility to investigate the influence of bond mobility on the fracture strength of the network. Our model is in essence a fiber bundle model, where load is distributed over many bonds. This generic approach is used to study fracturing in a wide range of material, from cotton yarn to earthquakes [181]. The salient feature of our model is that the reversible bond dynamics in combination with local load sharing give rise to an inherent length scale for crack initiation as explained in our previous work [173].

The main result of our work is that bond mobility hardly affects mean field properties of a bond, such as the average bound lifetime, but significantly reduces the network's strength. We attribute the reduced network strength to the 'leaking' of linkers from crack areas to less stressed regions within the network. Intriguingly, mobile linkers are widespread in biology despite the reduced fracture strength compared to networks connected by immobile linkers. We speculate that cells trade fracture strength for the modularity and tight dynamic control offered by mobile linkers.

5.2. MODEL

5.2.1. IMMOBILE LINKERS

In this work, we compare a network connected by mobile linkers to a network connected by immobile linkers. For immobile linkers, we use a model that was introduced in reference [173]. Here, we briefly summarize its salient features for clarity, and afterwards explain how we extend this model to the case of mobile linkers.

We initialize a one-dimensional (1D) network with N equally spaced linkers using periodic boundary conditions, each link having a probability K to start in a bound state (figure 5.1a). Next we model the dynamics of the linkers with a kinetic Monte Carlo scheme [157] using the following linker dynamics:

$$K = \frac{k_{\mathrm{on}}}{k_{\mathrm{on}} + k_{\mathrm{off},0}} \tag{5.1}$$

where k_{on} is the rate of linker binding and $k_{\mathrm{off},0}$ the rate of linker unbinding in the absence of force. We normalize time by the on-rate, k_{on}. The off-rate increases exponentially with the applied force f_i on the linker i, in keeping with the Bell model [142]:

$$k_{\mathrm{off}}(f_i) = k_{\mathrm{off},0} \cdot \exp(\frac{f_i}{f_{1/\mathrm{e}}}) \tag{5.2}$$

where $f_{1/\mathrm{e}}$ is the force where the off-rate has decreased to $k_{\mathrm{off}}(f_{1/\mathrm{e}}) = k_{\mathrm{off},0}/e$. We calculate the force per linker f_i via

$$f_i = \alpha_i \cdot \sigma \tag{5.3}$$

where σ is the stress on the system and α is a yet to be defined stress intensity factor per linker. To account for the effect of inhomogeneous force distribution characteristic of polymer networks [125, 151, 152], we assume local loading sharing. Previously, we have shown that local load sharing provides an accurate description of crack initiation in macroscopic viscoelastic materials ($N > 100$) [173] consistent with experiments [129, 136, 154, 155]. Specifically, we assume that the force distribution is dependent on the distance l_i of a linker to its nearest bound linker on both sides. Explicitly, we define a stress intensity factor α on a bound linker at site i by:

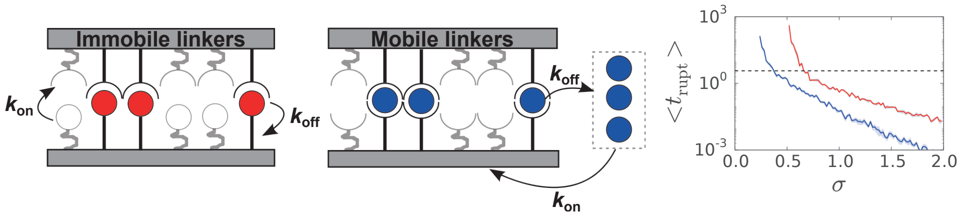

(a) **(b)** **(c)**

Figure 5.1: Immobile linkers provide stronger networks than mobile linkers. a) We consider the dynamics of bonds that bind with a rate k_{on} and unbind with a rate k_{off} that increases exponentially according to equation 5.2. Immobile linkers rebind in the same location from which they unbound, whereas (b) mobile linkers rebind in a random new location from a pool of freely diffusing linkers. c) The network lifetime versus of stress for networks connected by either mobile (blue) or immobile linkers (red). In both cases, a metastable regime at low stress and an unstable regime at high stress are observed, with a cross over at $< t_{\text{rupt}} >= \frac{1}{k_{\text{off}}} + \frac{1}{k_{\text{on}}}$ (dashed line). Notably, networks connected by immobile linkers have a higher $< t_{\text{rupt}} >$ at all stresses. $K = 0.9$ and $N = 10^3$ for both networks. The shaded regions show the standard deviation of the rupture time on basis of 30 repeats per condition.

$$\alpha_i = N \cdot \frac{l_i}{\Sigma_i l_i} \tag{5.4}$$

Note that the total force is independent of the bound fraction and normalized by the system size, $\frac{\Sigma_i f_i}{N} = \sigma$. We normalize the applied stress by the linker force sensitivity $f_{1/e}$. After calculating the force on all linkers, we employ a kinetic Monte Carlo step to either bind or unbind a linker stochastically. We repeat this process until all linkers are unbound, and define the time at which the last linker unbinds as the rupture time t_{rupt}.

5.2.2. MOBILE LINKERS

We model mobile linkers by initializing N linkers with a probability K to start in the bound state. Every linker gets assigned a random location in a network of length N. Each bound linker follows the same unbinding rules as explained above for immobile linkers, and each unbound linker binds with a rate k_{on}. However, crucially, the difference with immobile linkers is that mobile linkers get assigned a new location in the network (figure 5.1b), whereas immobile linkers always rebind in the same location as where they previously unbound. For mobile linkers, we consider the limit of rapid diffusion after unbinding, and therefore rebinding occurs in a random new location. Throughout the paper, we compare mobile and immobile linkers using the same parameters K, N and σ.

5.3. RESULTS

To probe the mechanical strength of transient networks, we study the network lifetime as a function of the applied stress. We run 30 simulations for each set of parameters and record the rupture time as the time where the fraction of closed bonds drops to zero. This way, we compare the rupture time as a function of stress for networks connected by mobile linkers versus immobile linkers, using otherwise identical parameters (figure 5.1b). We find that the average lifetime decreases with applied stress with two distinct regimes for both types of networks (figure 5.1c). In the high stress regime, the network lifetime is significantly shorter than the bond turnover time ($< t_{\mathrm{rupt}} > \geq \frac{1}{k_{\mathrm{off}}} + \frac{1}{k_{\mathrm{on}}}$, dashed line). In this regime, the network is unstable and the lifetime decreases exponentially as applied stress promotes linker unbinding. In the low stress regime, the network is metastable and linkers re-bind many times before rupturing is observed. The average network lifetime again decreases exponentially with stress, but more steeply compared to the high stress regime as not only the linker unbinding speeds up as a function of stress, but also the critical length for crack nucleation decreases (see section 5.4). Qualitatively, mobile and immobile linkers show a similar biphasic stress-dependence of the network rupture time. Strikingly, however, the mobile networks are weaker for all observed stresses, even though the linker affinity K and number of linkers N are identical.

To investigate why linker mobility compromises network strength, we compare the microscopic linker properties at steady state. We first consider the average lifetime of the bound linkers as a function of stress. As shown in Figure 5.2a, the average bound linker lifetime decreases with stress for both networks, due to force-induced unbinding. Moreover, the average lifetimes are comparable for mobile and immobile linkers. Similarly, we find that the average bond-bond distance is comparable for mobile and immobile linkers ($< l >= 1.4$ and $< l >= 1.1$ respectively, vertical lines in figure 5.2b).

Why is the network lifetime with mobile linkers drastically smaller than with static linkers, even though the average linker lifetime and bond-bond distance are similar? To understand this difference in network lifetime, we need to look beyond the mean field properties as rupture is a stochastic phenomenon, initiated by the emergence and growth of cracks due to local fluctuations [129, 136, 154, 155, 173]. Plotting the distribution of bound linker distances at steady state reveals a crucial difference between immobile and mobile linkers: whereas their mean values are comparable, the bond-bond distance is significantly more widely distributed for mobile than for immobile linkers (figure 5.2b). We conclude that the reduced strength of networks crosslinked by mobile linkers is due to a more inhomogeneous force distribution over all bonds.

To investigate at what system size the difference between mobile and immobile linkers emerges, we compare networks with sizes ranging from $N = 1$ to $N = 10^3$ (figure 5.3). For both mobile and immobile linkers, $< t_{\mathrm{rupt}} >$ increases with N for microscopically small systems (up to $N \approx 10$ for mobile linkers or $N \approx 20$ for immobile linkers), as relative fluctuations in the number of bound linkers become smaller. Conversely, for macroscopically large systems ($N \approx 30$ for mobile linkers or $N \approx 20$ for immobile linkers) the average rupture time decreases with system size according to a power of -1, as the number of crack nucleation sites increases linearly with the system size. However, an intermediate size regime exists for mobile linkers ($20 < N < 30$) where a faster decrease of the rupture time is observed. We hypothesize that this intermediate regime is caused

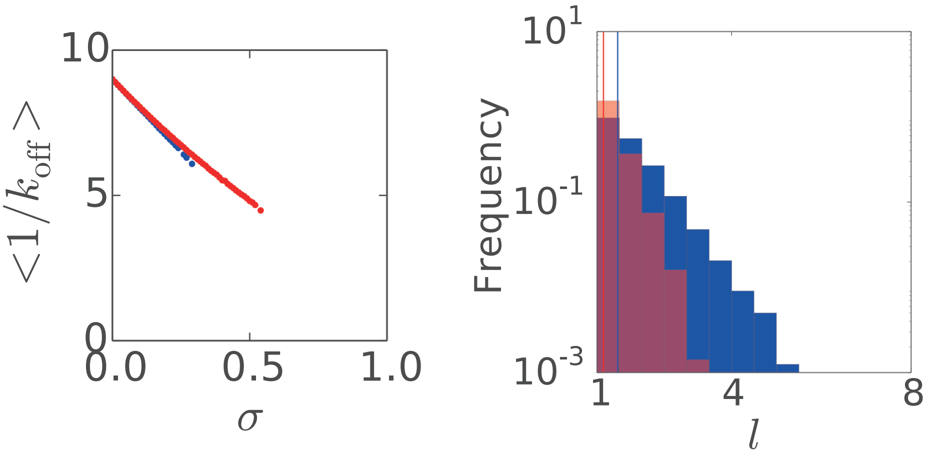

(a) (b)

Figure 5.2: Bond mobility does not affect the average linker lifetime and bond spacing, but broadens the distribution of bond-bond distances. a) Average bound lifetime of mobile (blue) versus immobile linkers (red) as a function of the applied stress ($K = 0.9$, $N = 10^3$). The networks are first equilibrated under stress up to $t = 30$, before the average bond lifetime is determined. The average bound lifetime is measured over the entire metastable regime, which extends to larger stress for immobile than for mobile linkers (figure 5.1c). b) Distribution of bond-bond distances measured at a fixed stress, bond affinity and system size ($\sigma = 0.2$, $K = 0.9$ and $N = 10^3$). The vertical lines represent the average bond-bond distance for immobile (red, $< l >= 1.1$) and mobile linkers (blue, $< l >= 1.4$).

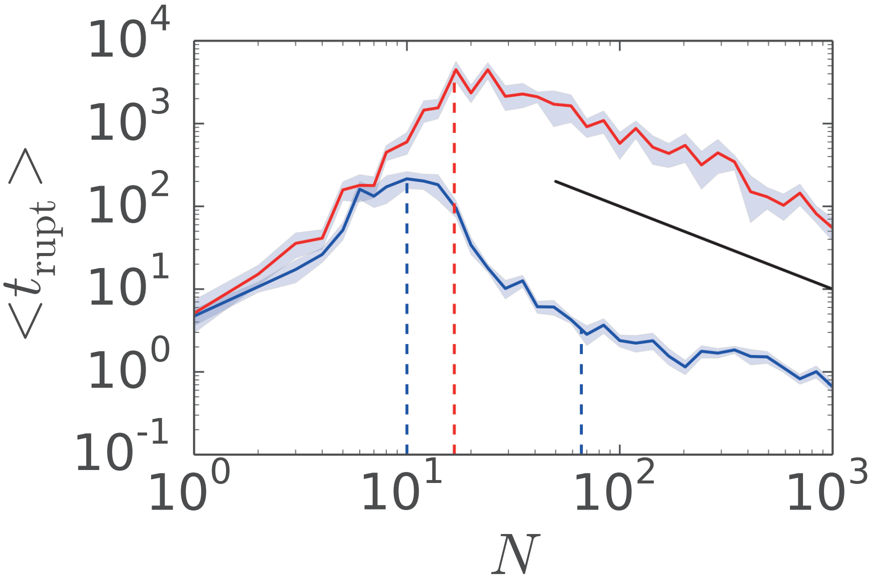

Figure 5.3: System size dependence of the network lifetime. The network lifetime is compared for immobile linkers (red) and mobile linkers (blue). For microscopically small systems ($N \leq 10$) the network lifetime increases with N ($\sigma = 0.55$, $K = 0.9$). For macroscopic systems, the network lifetime follows a -1 power law (black line) due to an increase of possible crack nucleation sites. For networks connected by mobile linkers, an intermediate size regime exists (between the two blue dashed lines) where the network lifetime decreases more steeply.

by ’leaking’ of linkers from stressed areas (large l) to the rest of the material.

In the limit of small systems, smaller than the crack length, rebinding of linkers always happens in the vicinity of the unbinding area. In the opposite limit of macroscopic materials, much larger than the crack length, the pool of free linkers is constant in time and therefore uncorrelated from local fluctuations in bound linker density. Thus, the network lifetime decreases solely due to the increased number of crack nucleation sites. For intermediately sized systems, there is an enhanced reduction in network lifetime with increasing system size, because the correlation between local bound linker density and pool of free linkers becomes smaller with system size. Local unbinding of a linker increases the fraction of free linkers that can subsequently rebind in the crack area. For macroscopically large systems however, the fraction of free linkers is relatively constant in time due to the rule of large numbers. In other words, linkers in macroscopic systems effectively ’leak away’ from the crack area into the bulk of the material.

5.4. THEORY

To test the hypothesis that mobile linkers leak away, we modeled the dynamics of a gap area free of linkers within the material of length L. The two processes which affect L are binding of linkers anywhere within the gap, and unbinding of either of the two linkers at the edge of the gap. We assume that the gap length L is significantly longer than the distance of each edge linker to its nearest neighbor. The unbinding rate of either of the linkers at the edge k_{L+} is therefore:

$$k_{\text{L+}} \approx 2 \cdot k_{\text{off}}(\frac{1}{2} \cdot L \cdot \sigma) = 2 \cdot k_{\text{off},0} \cdot \exp(\frac{1}{2} \cdot L \cdot \sigma) \tag{5.5}$$

The pre-factor 2 results from the fact that two linkers can unbind, and the exponent $\frac{1}{2}$ is because the force over the gap $(L \cdot \sigma)$ is distributed over both edge linkers. We next consider the binding of linkers anywhere within the gap. As the gap size increases, the rate of binding increases as more binding possibilities are present:

$$k_{L-} = \begin{cases} L \cdot k_{\text{on}} \cdot \frac{N-n}{N} & \text{Mobile} \\ L \cdot k_{\text{on}} & \text{Sticky} \end{cases} \tag{5.6}$$

where k_{L-} is the rate of binding in the gap, and n is the number of bound linkers. The factor $\frac{N-n}{N}$ for mobile linkers arises from the fact that the pool of free linkers decreases with the fraction of bound linkers. For immobile linkers, rebinding does not depend on the *global* pool of free linkers, as every linker only rebinds locally. For macroscopic systems, n is independent of L, namely $n = n_{\text{steady}}$. We calculate n_{steady} by numerically solving:

$$\frac{dn_{\text{steady}}}{dt} = 0 = k_{\text{on}} \cdot (N - n_{\text{steady}}) - k_{\text{off}}(\sigma) \cdot n_{\text{steady}} \tag{5.7}$$

where $k_{\text{on}} \cdot (N - n_{\text{steady}})$ is the total rate of linker binding and $k_{\text{off}}(\sigma) \cdot n_{\text{steady}}$ is the total rate of linker unbinding within the network. As $k_{\text{L-}}$ increases linearly with the gap size, whereas $k_{\text{L+}}$ increases exponentially, gaps will always become unstable for large enough L as unbinding occurs significantly more rapidly than re-binding [173]. We are interested in the length L_{unstable} at which gaps become unstable and propagate. We approximate L_{unstable} by calculating the length at which the rate of unbinding at the edge equals the rate of binding within the center $k_{L+}(L_{\text{unstable}}) \approx k_{\text{L-}}(L_{\text{unstable}})$, which we can numerically solve by combining equations 5.5, 5.6 and 5.7.

We test our theory quantitatively by measuring L_{unstable} by performing simulations where we ablate a gap of controlled length: first we equilibrate a network under stress until $t = 30$, after which we unbind all bound linkers in the positions $l = 0 \ldots l_{\text{ablate}}$. Next, we observe the network until $t = 60$ (figure 5.4a). We repeat this procedure for 100 networks per condition and plot the fraction of ruptured networks ϕ_{rupt} as a function of l_{ablate} (figure 5.4b). For small l_{ablate}, all networks stay intact, whereas networks become unstable and rapidly fracture for large l_{ablate}. We extract L_{unstable} from simulations by calculating the ablation length at which $\phi_{rupt}(l_{\text{ablate}}) = 0.5$ via linear interpolation. We observe that mobile linkers have a shorter typical ablation length than immobile linkers ($L_{\text{unstable}} \approx 35$ versus $L_{\text{unstable}} \approx 60$, respectively (figure 5.4b). For both types of networks,

L_{unstable} increases with σ as cracks are more likely to propagate under increasing stress (symbols in figure 5.4c). The theoretical model describes this trend correctly, although there is a systematic under-estimation of the absolute value of L_{unstable} by approximately 20% (lines in figure 5.4c). A fully quantitative calculation of L_{unstable} would require solving $\frac{dL_{\text{unstable}}}{dt} = 0$, which is not possible as we do not have an equation for $\frac{dL}{dt}$. Therefore, we have approximated the unstable point L_{unstable} by calculating the gap length at which linker unbinding is equally likely as linker binding within the gap. However, $k_{L+}(L_{\text{unstable}}) \approx k_{\text{L-}}(L_{\text{unstable}})$ is only a good approximation of the unstable length if an unbinding event increases the gap size by an equal amount as a rebinding event would decrease it. This assumption is not fully correct, as a linker unbinding event might only cause a marginal increase in gap length L in case the unbinding linker has a neighboring linker that is close-by, whereas a linker rebinding in the middle of the gap halves the gap size L.

We next calculated the crack length L_{unstable} as a function of the bond affinity K for both mobile and immobile linkers at a fixed $\sigma \cdot K = 0.2$ (figure 5.4d). We fix $\sigma \cdot K$ rather K, because otherwise L_{unstable} would increase far more rapidly as a function of K and would not be computationally tractable for large K. Furthermore, we choose to plot $L_{\text{unstable}} \cdot K$, rather than L_{unstable}, as this quantity roughly represents the number of ablated bound linkers. It is therefore more straightforward to interpret than L_{unstable} for different values of K, as the density of bound linkers varies with K. We find that $L_{\text{unstable}} \cdot K$ stays approximately constant for mobile linkers upon increasing the bond affinity K, whereas it increases for immobile linkers. As a result, the difference in $L_{\text{unstable}} \cdot K$ between mobile and immobile linkers is most pronounced for high K, whereas the two types of networks become similar at low K. Indeed, as seen from equation 5.6, the only difference between mobile and immobile linkers is the factor $\frac{N-n}{N}$, which reduces the rate of binding within a gap. In the limit of a low bond affinity K, $n_{\text{steady}} \ll N$ and therefore immobile and mobile linkers behave identically.

5.5. DISCUSSION

We studied the dynamics of a transient network of reversible bonds under mechanical stress, and have compared immobile linkers, which always rebind in the same place as where they unbound, with mobile linkers, which can rebind anywhere within the network. We found that the mean lifetime of bound linkers in a transient network is unaffected by the mobility of the linker (figure 5.2a). Yet, networks connected by mobile linkers are significantly weaker than network connected by immobile linkers, with fracturing times that are orders of magnitude lower (figure 5.1c). We attribute the reduced strength of networks connected by mobile linkers to the redistribution of mobile linkers from areas low in linker density, corresponding to highly stressed areas, to the rest of the material. This effect does not occur for immobile linkers, as they stay in the place from which they unbound. Our general model shows that linker mobility lowers the lifetime of any transient network with a system size larger than the crack initiation length l_{unstable}. We have investigated this length scale in the limit of nearest neighbor load sharing, but in previous work we have shown that this length scale also emerges for more long-ranged types of load sharing [173]. Therefore, we expect that our conclusion of reduced net-

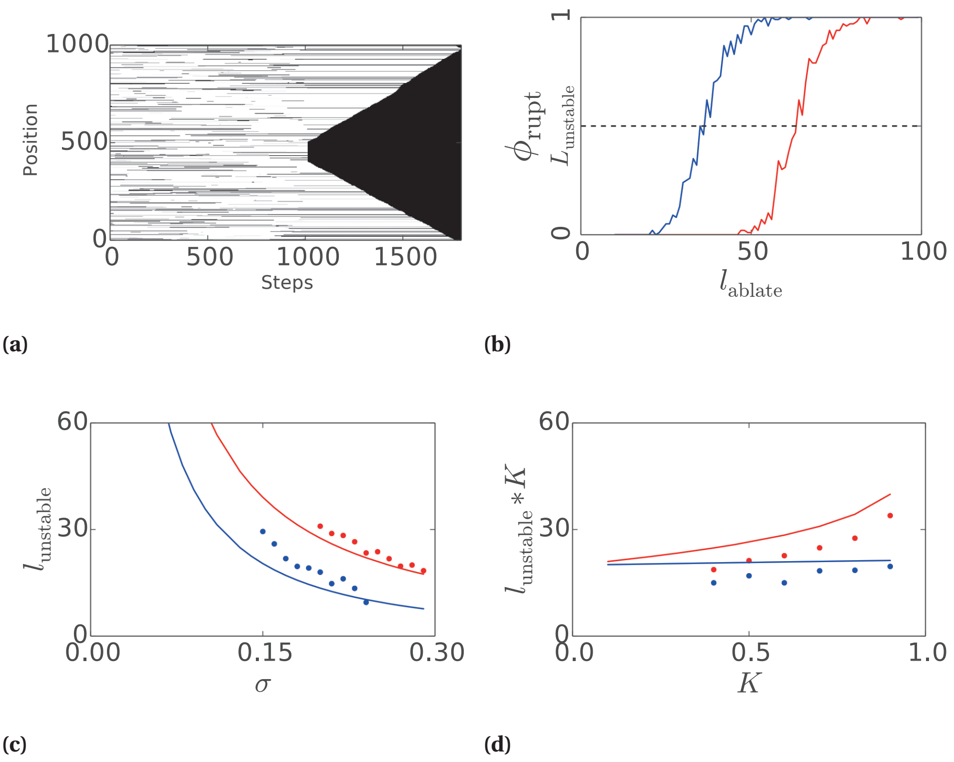

Figure 5.4: Bond ablation for immobile and mobile linkers. a) Kymograph representation of an ablation experiment ($K = 0.9$, $\sigma = 0.2$, $N = 10^3$ and $l_{\text{ablate}} = 100$; mobile linkers). We plot the bond position as a function of simulation step, where white represents a bound linker and black represents an unbound linker. The first 1000 steps show steady state dynamics of stochastic binding and unbinding, after which we ablate 100 adjacent bonds. Afterwards, the ablated gap propagates and the material fractures. b) The fraction of ruptured networks ϕ_{rupt} plotted as a function of ablation length l_{ablate} reveals how zones depleted of bonds can trigger fracturing. Notably, immobile linkers (red) require a larger l_{ablate} to trigger fracturing than mobile linkers (blue) ($\sigma = 0.2$, $K = 0.9$ and $N = 10 \cdot l_{\text{ablate}}$). (c, d) We compare l_{unstable} from the simulations (dots) with the theoretical prediction (lines - no free parameters) as a function of the applied stress σ (c - fixed $K = 0.9$) and the bond affinity K (d - fixed $\sigma \cdot K = 0.2$). Bond mobility weakens networks at high K but has no effect for small K.

work lifetime by bond mobility holds true for any macroscopic transient network. We note that we chose a one-dimensional model because nearest neighbor load sharing becomes ill-defined in higher dimension as the shape of a defect somehow needs to be acknowledged. Given that transient networks such as colloidal gels or polymer networks are not continuum materials at the microscopic level, no sensible choice can be made for load sharing in higher dimensions. However, we expect that our conclusion is general, as crosslinkers will leak away regardless of the dimensionality of the system.

Our results raise the question of why mobile linkers exist at all in nature [22, 37, 174, 175], as immobile linkers yield stronger networks. An important thing to note in this context is that fracturing in biology is not always detrimental. In fact, fracturing in some cases is even required for biological function. For example local failure of the actin cortex can lead to cell polarization [14–16] and facilitate a mode of cellular migration which relies on the formation of membrane blebs [18]. Similarly, destabilization and subsequent rupturing of the polar actomyosin cortex aids proper positioning of the cytokinetic furrow [17]. However, in many other circumstances fracturing of transient networks in biology is related to developmental defects [10, 12] and diseases [13, 115]. Therefore, the widespread existence of mobile linkers involved in cellular adhesion [22, 174, 175] and crosslinking of biopolymer networks [37, 71] requires explanation.

Both cell-cell and cell-matrix adhesion are mediated by proteins embedded in the membrane, which are either bound to their substrate or diffuse within the plane of the membrane and can therefore be classified as mobile linkers. Examples of such protein families are E-cadherin for cell-cell adhesion and integrin for cell-matrix adhesion [22]. The collagen matrix to which integrins adhere have mesh sizes of up to several micrometers [3], whereas the individual collagen fibers are only a few tens of nanometers thick [182]. As a result, the fraction of the membrane area which is in close enough proximity to fibers to allow for binding is very low. A large fraction of the plasma membrane area would have to be covered with immobile linkers in order to have a significant number of integrins interacting with the extracellular matrix. Instead, we speculate that linker mobility allows for diffusion through the membrane to facilitate binding to the sparse fibers. Therefore, linker mobility allows for cellular adhesion whilst requiring only a small fraction of the membrane area.

Biopolymer networks are either connected via stickiness of the fibers, for example in the case of fibrin fibers [180], or via mobile linkers such as cross linking ions which cross link the intermediate filament vimentin [71]. Different from the case of cellular adhesion, linker mobility does not necessarily increase the connectivity of biopolymer networks: where immobile linkers only require close proximity of two fibers, mobile linkers require the proximity of two fibers *and* the proximity of a linker. For ionically cross linked intermediate filaments, linkers are abundantly present as the concentration of magnesium ions in the cytosol is on the order of a mM [183]. Furthermore, as the concentration of intermediate filaments is orders of magnitude lower, in the μM regime [184], magnesium is abundant and has a low effective bond affinity K. In this regime mobile linkers are as strong as immobile linkers (figure 5.4d).

Another case of mobile linkers are actin binding proteins which cross link the actin cytoskeleton [37]. Many different types of cross linking proteins exist, with an enormous variety in their cross linking properties such as length [87], compliance [185], preferred binding angle [107], angular flexibility [88], typical lifetime of actin binding [89] and force sensitivity of the unbinding rate [186]. Many of these linker properties have been found to affect biopolymer network mechanics [37, 54, 87, 88, 187]. As a result, this variety of mobile linkers allows the cell to have tight dynamic control of the mechanical properties of its actin cytoskeleton, which would be difficult to obtain if the actin filaments were connected by the stickiness of the fibers.

5.6. CONCLUSION

To summarize, we have studied the fracturing of transient networks connected by either mobile or immobile linkers. Our main result is that linker mobility weakens networks under stress. We have proposed and verified a theoretical model to explain this effect on basis of the leaking of linkers from crack areas to less stressed areas within the material. Even though linker mobility weakens transient networks, mobile linkers are widespread in biology. We speculate that cellular adhesion proteins are more likely to interact due to linker mobility and the large variety of mobile linkers connecting the actin cytoskeleton allows for a flexible control over the mechanics.

5.7. FUTURE WORK

In this work we have focused on the effect of crosslinker mobility using a minimal model that contains only general features of transient networks, namely its linker dynamics. Beyond this general feature, real-life transient networks differ widely in their microscopic properties. For example, biopolymers are typically significantly stiffer than synthetic polymers [93]. Brownian dynamics simulations have been limited to investigate steady state properties of such materials [85], as studying fracturing is computationally very expensive due to the large separation of timescales between the linker unbinding rate and the network rupture time. By focusing exclusively on the crosslinker dynamics, our model allows for studying the effect of different types of crosslinker dynamics on network fracturing in a minimal model. However, it remains an open question how microscopic properties such as the network coordination number, filament stiffness and filament length affect the crack initiation rate of transient networks.

We hypothesize that such microscopic properties affect the crack initiation rate via the degree of load sharing. Up to now, we have considered fully localized (nearest neighbour) or global (homogeneous) load sharing [173]. However, the model can be readily extended to any type of intermediate load sharing [170, 171]. For future work, we suggest that detailed molecular dynamics simulations can be used to measure the degree of load sharing of various types of networks by bond removal and subsequent measurement of the load redistribution [188]. Next, this load redistribution can be used in our minimal model to investigate the crack initiation rate. Therefore, in the future our model allows for a multi-scale approach to investigate how the crack initation rate is influenced by microscopic properties such as the coordination number [169], filament length [86], crosslinker length [87], crosslinker density [35] and crosslinker flexibility [88].

We thank Pieter Rein ten Wolde and Chase Broedersz for fruitful discussions.

6

CATCH BONDS FORM DYNAMIC YET STRONG MATERIALS

Nature uses dynamic materials in order to combine mechanical resistance with the ability to adapt and self-heal. Biological soft matter is therefore made of transiently bonded interfaces and polymers [4, 189, 190]. Whereas synthetic transient networks readily fracture due to the inherent force sensitivity of dynamic bonds [129, 173, 191], biological networks are surprisingly strong [57, 192, 193]. How does biological matter achieve the ability to flow without risking mechanical failure [10, 11]? Remarkably, many biopolymer networks and virtually all cellular interfaces are crosslinked by catch bonds [194–196], proteins whose bond lifetime increases when moderate forces are applied via exposure of hidden binding sites [116]. After full exposure at high force, catch bonds behave like normal (slip) bonds whose bond lifetime monotonically decreases with force [116, 142]. Here we show by stochastic modeling of transient networks under stress that catch bonds provide vastly more long-lived networks than slip bonds. Surprisingly, catch bond networks are stronger than slip bond networks even when the individual bonds are weaker, which we attribute to a self-assembly mechanism against force inhomogeneity. We verify our conclusion experimentally by performing single molecule and network experiments on actin networks crosslinked by ACTN4 and a K255E mutant. Our work provides insight into the widespread phenomenon of catch bonds in biology and offers a new design route towards life-like materials that combine material adaptability with strength.

Protein/complex	**Plays a role in**	**Reference**
	Cellular interfaces	
P-Selectin	Cell-matrix adhesion	[198]
L-Selectin	Cell-matrix adhesion	[199]
Integrin	Cell-matrix adhesion	[194]
Von Willebrand factor	Cell-matrix adhesion	[200]
CD44	Cell-matrix adhesion	[201]
Cadherin	Cell-cell adhesion	[202]
Notch-jagged	Cell-cell adhesion	[203]
Catenin	Membrane-cytoskeleton adhesion	[196]
Talin	Membrane-cytoskeleton adhesion	[204]
Vinculin	Membrane-cytoskeleton adhesion	[59]
BBK32	Bacterial adhesion	[28]
FimH	Bacterial adhesion	[205]
	Biopolymer networks	
Myosin	Cytoskeleton	[206]
Kinetochore	Cytoskeleton	[207]
Actin	Cytoskeleton	[208]
Fibrin	Extracellular matrix	[209]
α-Actinin-4	Cytoskeleton	[38, 57], this work

Table 6.1: Overview of known proteins and complexes exhibiting catch bond behavior.

6.1. INTRODUCTION

Single molecule experiments have demonstrated catch bond behavior for a wide range of biological linkers (Table 6.1). Chief among them are actin binding proteins, which crosslink actin filaments in the cytoskeleton of the cell [4], and transmembrane proteins known as cadherins [175] and integrins [174], which form cell-cell and cell-extracellular matrix adhesions. Whereas catch bonds are well-studied on the single molecule level [116, 194–196], emergent phenomena in materials connected by catch bonds remain unexplored. To bridge this gap, we consider a simple 1D network of N reversible bonds sharing a load σ (Fig. 6.1a). We compare catch bonds with slip bonds. Specifically, we consider catch bonds that hide a second, strong binding site in the absence of force with their constitutively active counterparts whose two binding sites are always open. This comparison mimics the situation of a wild-type protein that acts as a catch bond and a mutant protein that is constitutively open such as the actin crosslinker ACTN4 and its K255E mutant [38, 57, 197]. Following this definition, catch bonds have a shorter lifetime than the corresponding slip bonds, irrespective of the applied force (Fig. 6.1b).

6.2. THEORETICAL MODEL

We model the effect of a force f on the unbinding rate k_{off} of a bound linker i as follows:

$$k_{\text{off},i}(f_i) = k_{\text{off},0}^{\text{catch}} \cdot \exp(-\frac{f_i}{f_{1/e}^{\text{catch}}}) + k_{\text{off},0}^{\text{slip}} \cdot \exp(\frac{f_i}{f_{1/e}^{\text{slip}}}) \tag{6.1}$$

The first exponent models the catching of the weakly bound state whereas the second exponent models the slipping of the active state. We compare catch bonds with constitutively active (slip) bonds ($k_{\text{off},0}^{\text{catch}} = 0$), keeping all other parameters identical (Table 6.2). We define a bond affinity $K = \frac{k_{\text{on}}}{k_{\text{on}}+k_{\text{off},0}}$, where k_{on} is the on-rate of unbound linkers. To account for the mobility after unbinding of linkers such as integrins and actin binding proteins, which diffuse in resp. the membrane or the cytosol, we allow for unbound linkers to rebind at a random new location [194, 196].

It is known that stressed networks connected by reversible bonds exhibit spontaneous crack initiation and propagation due to inhomogeneous load sharing [129, 173, 191]. We reproduce this fracturing behavior using a minimal model where the force per linker f_i depends on the global stress and the distance to its nearest neighbors l_i in 1D, using periodic boundary conditions (Fig. 6.1a):

$$f_i = \frac{l_i}{\Sigma_i l_i} \cdot \sigma \tag{6.2}$$

The total system length is normalized such that it equals the number of bonds. Time is normalized by the on-rate, and the applied stress is normalized by the typical unbinding force $f_{1/e}^{\text{slip}}$ and by the number of bonds.

Surprisingly, even though we consider slip bonds that are stronger on the single molecule level (Fig. 6.1b), we find that networks of catch bonds are nevertheless more stable under stress than networks of slip bonds. This is illustrated in Fig. 6.1c, which shows the time evolution of the bound linker fraction for networks of $N = 10^3$ bonds under a stress of $\sigma = 0.485$. The bound fraction initially shows only small fluctuations due to the large number of bonds, but in both catch and slip bond networks, the bound fraction eventually drops to zero due to the initiation and propagation of a crack (Fig. 6.12). Strikingly, the rupture time is only around 50 for the network of slip bonds (blue), whereas it is around 900 for the networks of catch bonds. Repeat simulations robustly show that despite the stochastic nature of fracturing, the network strength is enhanced by catch bonds compared to slip bonds (top panel Fig. 6.1c).

To investigate the generality of the enhanced strength of catch bond networks, we compare the average rupture time of catch and slip bond networks as a function of stress (Fig. 6.2a). For both types of networks, the network lifetime decreases exponentially with the applied stress with two distinct regimes. For low stresses, the networks are metastable and they experience stochastic fracture due to local fluctuations in bond density. For high stresses, the networks are unstable and all bonds unbind progressively. The cross-over rupture time separating the two regimes is comparable to the linker lifetime (indicated by the dashed line). We find that in the metastable regime, where the network lifetime is longer than the bond lifetime, catch bond networks are more long-lived

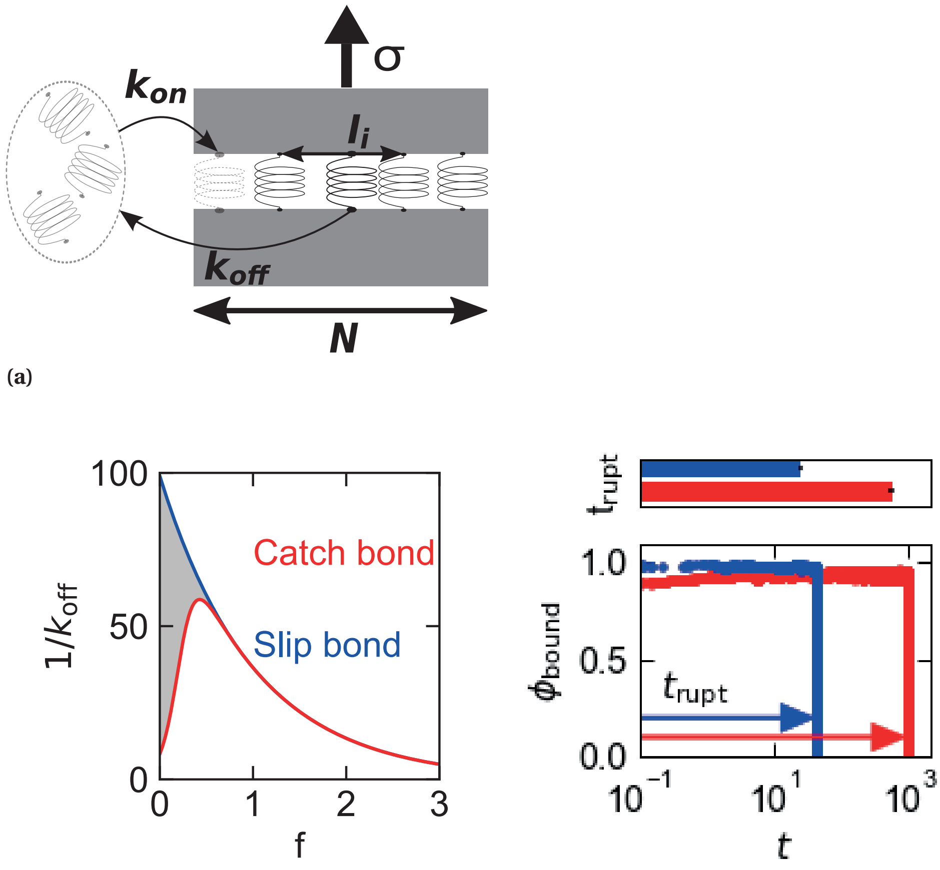

(a)

(b) **(c)**

Figure 6.1: Catch bonds enhance the mechanical strength of transient networks. a) We model transient networks as 1D arrays of linkers that stochastically exchange between a bound and freely diffusing state. N bound linkers share the applied force inhomogeneously according to the nearest neighbor distance l_i (red). b) Single molecule bound lifetime as a function of applied force for catch bonds (red) and slip bonds (blue), with $k_{\text{off},0}^{\text{slip}} = 0.01$, $k_{\text{off},0}^{\text{catch}} = 0.1$ (or $k_{\text{off},0}^{\text{catch}} = 0$ for the slip bond) and $f_{1/e}^{\text{catch}} = 0.4$. The grey area indicates the hidden binding potential of the catch bond compared to the constitutively active slip bond. c) Example rupture trajectories for catch and slip bonds showing the time evolution of the fraction of bound linkers under a stress $\sigma = 0.4$ with arrows indicating the rupture time of the network. Top panel: Comparison of the average rupture time for networks crosslinked by catch and slip bonds obtained from 50 repeats per condition.

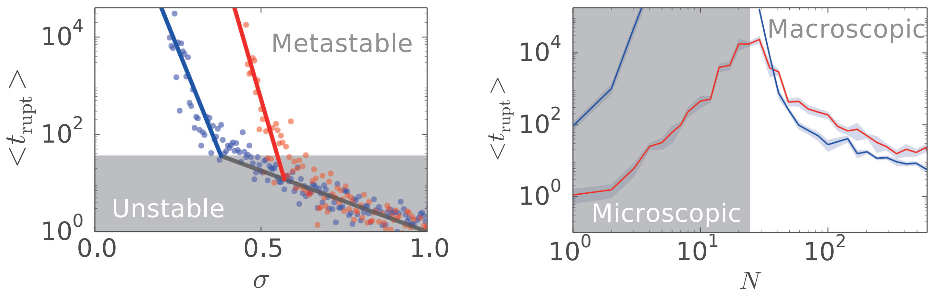

(a) **(b)**

Figure 6.2: Catch bonds provide enhanced network strength in metastable macroscopic networks. a) Both catch (red) and slip (blue) bond networks exhibit a metastable ($t_{\mathrm{rupt}} \geq 1/k_{\mathrm{off}}$) and an unstable rupture regime ($t_{\mathrm{rupt}} < 1/k^{\mathrm{slip}}_{\mathrm{off},0}$, grey area). The average rupture time decreases exponentially with the applied stress for both networks, but catch bond networks are significantly more long-lived in the metastable regime (solid lines to guide the eye). b) Both catch and slip bond networks exhibit a biphasic response on system size with a microscopic and macroscopic regime. Catch bond networks are weaker than slip bond networks for microscopically small systems (up to several tens of bonds), but stronger for macroscopic materials.

than slip bond networks by several orders of magnitude. We conclude that strengthening by catch bonds is a robust phenomenon.

How can catch bonds provide more long-lived networks than slip bonds, even though they are more short-lived on the single molecule level? As the increased network strength is a collective phenomenon, it is interesting to investigate what system size is required for the effect to emerge. We observe a biphasic dependence of the rupture time on system size for both catch and slip bonds, with an initial increase for small N followed by a decrease for large N. This biphasic dependence emerges from the nonlinear bond dynamics, which establish a critical crack length [97, 173]: for microscopic systems that are smaller than this critical crack length, the rupture time increases with N because relative fluctuations in the number of bound linkers become smaller [142]. By contrast, the rupture time increases with N for macroscopic systems, since the number of possible crack nucleation sites increases with system size. Our simulations show that catch bonds only exhibit longer network lifetimes compared to slip bonds for macroscopic systems larger than the critical crack length (Fig. 6.2b). For smaller systems, catch bond networks are actually weaker than slip bond networks. The catch bond advantage is therefore clearly not a single molecule property, but only emerges in macroscopic networks.

To investigate the mechanism behind this emergent behavior, we measure the steady state properties of the networks under stress. Specifically, we consider the distribution of distances between bonds in metastable networks under stress (Fig. 6.3a). Interestingly, the average bond spacing is higher for the catch bonds, consistent with their lower affinity, but the distribution is significantly narrower. Catch bond networks therefore present significantly fewer gaps of more than 40 empty bond sites. This interesting finding raises

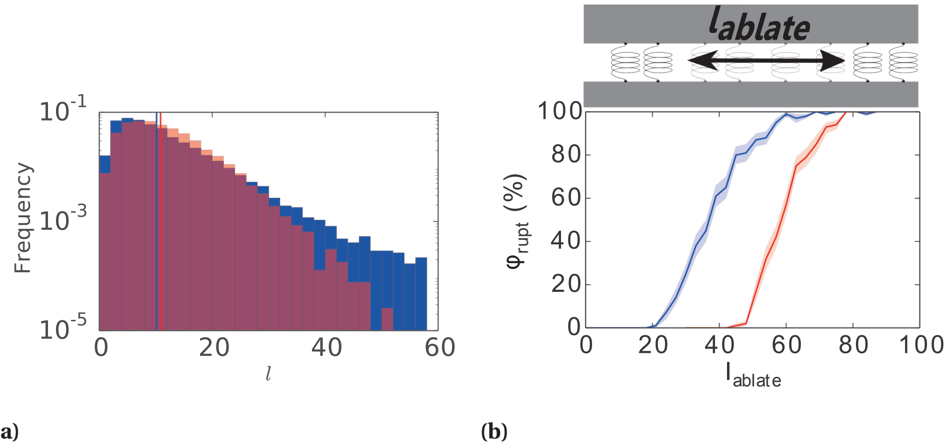

Figure 6.3: Catch bonds reduce force inhomogeneities and improve resilience against gaps. a) The distribution of bond distances l_i is measured at steady state ($3 < t < t_{\mathrm{rupt}} - 20$, sampled at intervals of $t = 30$, $\sigma = 0.22$). The average bond distance (vertical lines, 10.1 and 10.9) is larger for catch bonds (red) than for constitutively active slip bonds (blue), but the distribution is significantly more narrow. c) We perform ablation experiments by removing l_{ablate} adjacent bonds (black arrow, grey bonds) of a network under stress, and recording whether this ablation induces fracturing. The fraction of ruptured networks ϕ_{rupt} increases with ablation size for both constitutively active slip bond (blue) and catch bond (red) networks, but catch bond networks require larger ablation lengths to induce fracturing.

the question at which length gaps trigger network fracture. To identify this length scale, we perform ablation experiments: first we equilibrate a network under stress, and next we remove all bonds in the positions $l = 0 \ldots l_{\mathrm{ablate}}$ and observe the time evolution of the network. We repeat this procedure for 100 networks per condition and plot the fraction of ruptured networks ϕ_{rupt} as a function of l_{ablate} (Fig. 6.3b). All networks stay intact for small ablation lengths, whereas large ablation lengths destabilize the network and induce fracture. Notably, catch bond networks require approximately two times larger gap lengths to induce fracturing. Apparently the enhanced strength of catch bond networks emerges because they contain smaller gaps *and* can handle larger gaps without becoming unstable. Taken together, this means that cracks are less likely to initiate.

The observation that bonds are more homogeneously distributed in catch bond networks compared to slip bond networks suggests that linker diffusion and redistribution upon stress is an essential element of the strengthening mechanism. To test this idea, we simulate networks with immobile linkers, which can only rebind in the same location, so that bond redistribution is not possible (Fig. 6.10a). We again observe a biphasic dependence of network lifetime on system size, but, now the networks connected by catch bonds fail more readily than those connected by slip bonds irrespective of the system size (Fig. 6.10b). We conclude that bond redistribution is indeed essential for the catch bond advantage to emerge.

Finally we ask how the catch bond advantage depends on the single molecule binding kinetics. To this end, we study the lifetime enhancement ratio conferred by (mobile) catch bonds compared to slip bonds $\frac{<t_{\mathrm{rupt}}^{\mathrm{catch}}>}{<t_{\mathrm{rupt}}^{\mathrm{slip}}>}$ as a function of the degree of hidden binding potential and the activation force over a wide range of two orders of magnitude ($10^{-1.5} \leq k_{\mathrm{off},0}^{\mathrm{catch}} \leq 10^{0.5}$ and $10^{-1} \leq f_{1/\mathrm{e}}^{\mathrm{catch}} \leq 10^{1}$). We find that the catch bond advantage is maximal for intermediate values of both parameters and completely vanishes for large $k_{\mathrm{off},0}^{\mathrm{catch}}$ and/or large $f_{1/\mathrm{e}}^{\mathrm{catch}}$ (Fig. 6.4a). Importantly, we find that catch bonding only increases network lifetime when $k_{\mathrm{on}} \gg k_{\mathrm{off}}$ (Fig. 6.4b). This observation provides additional insight into the mechanism of the catch bond advantage. When $k_{\mathrm{on}} \gg k_{\mathrm{off}}$, an increase in k_{off} will barely affect the number of bound linkers, whereas the number of free linkers will linearly increase with k_{off}. This makes more linkers available for rebinding throughout the entire network, including in highly stressed areas, providing a self-assembly mechanism against force inhomogeneity that increases network lifetime (Fig. 6.4c).

6.3. EXPERIMENTAL VERIFICATION

6.3.1. ACTN4 AND A K255E MUTANT AS MODEL SYSTEM

To test the model's prediction that cryptic binding sites that can be open by force increase network stability, we compare actin networks crosslinked by wild type (WT) ACTN4 or by a K255E mutant. There is prior structural evidence that this crosslinker pair should nicely correspond to the catch/slip pair considered in our model [Fig. 6.1b]. WT ACTN4 has two weak actin-binding sites (ABS2 and ABS3 in Fig. 6.5b) that are always exposed, and one strong actin-binding site (ABS1) that is hidden [210]. The interaction between the ABS-1 domain and actin is blocked by an intramolecular lysine-tryptophan interface, which is thought to be opened upon mechanical loading [211]. In contrast, the ABS-1 binding domain is constitutively active for the K255E point mutant as the intramolecular interface is destabilized [Fig. 6.5b] [212]. The wild type crosslinker and the K255E mutant therefore serve as an ideal model system to experimentally test the prediction that hiding a linker binding site (ABS1-domain) improves network stability compared to crosslinking by a constitutively active linker (K255E mutant).

6.3.2. ACTN4-ACTIN CHARACTERIZATION

We first characterize both crosslinker variants by performing Fluorescence Recovery After Photobleaching (FRAP) measurements on actin networks crosslinked by fluorescently tagged crosslinkers. We find the recovery rate is 3.5 ± 0.6 s for the WT and 300 ± 160 s for the K255E mutant. This result is consistent with literature reports, which have shown that WT ACTN4 is a more dynamic linker than the K255E mutant [38]. Furthermore, we show that both WT and K255E crosslinkers are fully mobile after unbinding [Fig. 6.19], which is essential for the self-assembly process against force inhomogeneity predicted by the model [Fig. 6.10]. Next, we independently measure the affinity of the two crosslinkers using a high-speed cosedimentation assay. We determine the fraction of bound versus unbound linkers by measuring the amount of crosslinker that remains in the supernatant [Fig. 6.13]. We find that the WT variant has a binding affinity of $0.51 \pm 0.001\,\mu$M whereas the K255E mutant has a much higher affinity of $0.064 \pm 0.0002\,\mu$M [Fig.

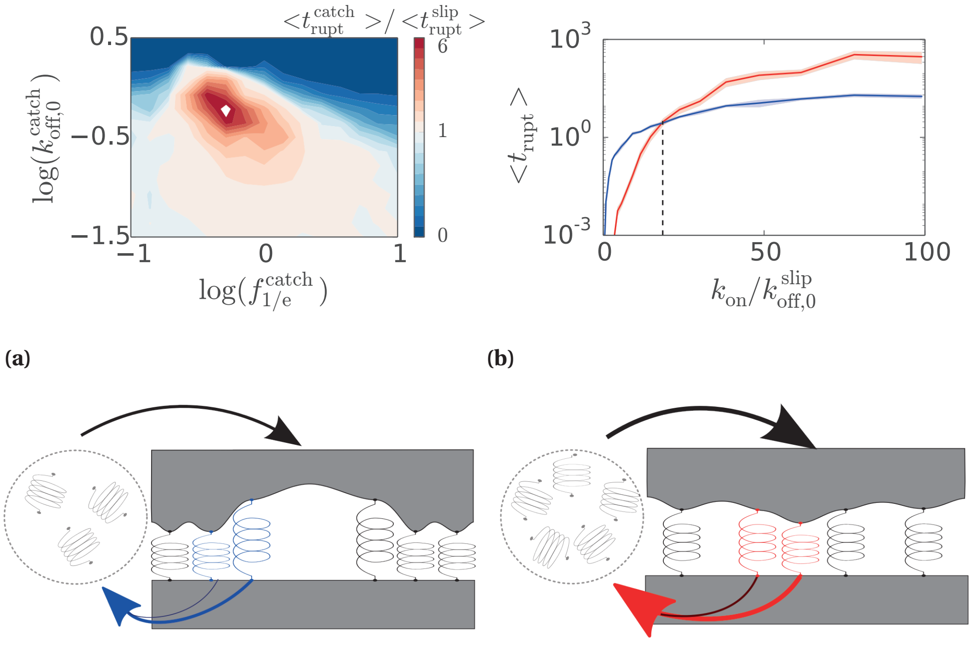

(a) **(b)**

(c)

Figure 6.4: Optimal catch bonding. a) Lifetime enhancement ratio of networks connected by mobile linkers as a function of the hidden binding potential and activation force reveals an optimum for intermediate values of both single molecule parameters. b) A plot of the network rupture time versus the binding affinity of the active state shows that catch bonds (red) only provide stronger networks than slip bonds (blue) close to the limit of saturation, where the majority of linkers is bound ($\frac{k_{on}}{k^{slip}_{off,0}} > 18$ or $K_{slip} > 0.95$, dashed line). c) Schematic of constitutively active slip bonds (left) versus catch bonds (right). Colored arrows represent the unbinding rate of a relatively stressed and relatively force-free linker. Catch bonds have a higher off-rate than the slip bonds, especially those carrying little force. Thus a larger pool of linkers is available for rebinding and thereby homogenizing the force distribution. This self-assembly process increases the lifetime of networks connected by catch bonds.

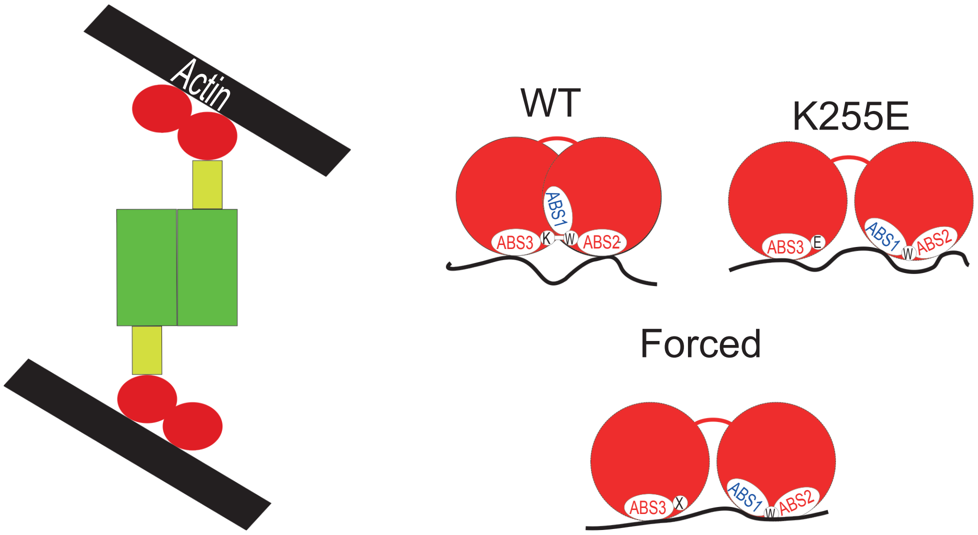

(a) **(b)**

Figure 6.5: Schematic of ACTN4-actin crosslinking. a) ACTN4 consists of two actin binding Calponin Homology (CH) domains (red), a neck region (yellow) and spectrin repeats (green) that mediate linker dimerization. b) The CH-domains contain three Actin Binding Sites (ABS). For the wild type (WT), ABS-1 is blocked from actin binding by a lysine-tryptophan interface that opens upon mechanical loading. In contrast, the ABS-1 domain is constitutively active for the K255E mutant**.**

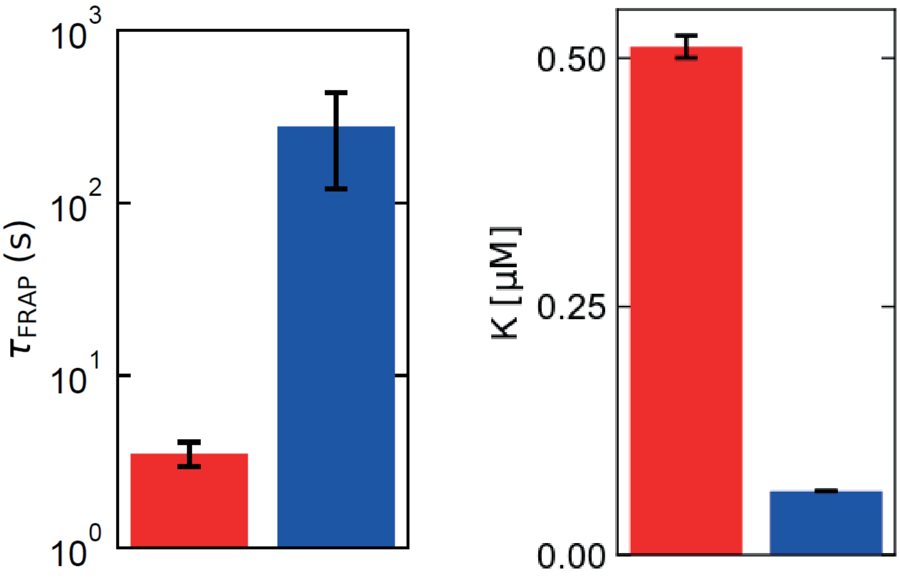

(a) **(b)**

Figure 6.6: ACTN4-actin linker kinetics. a) Crosslinker remodelling timescale measured with FRAP for WT (red) and K255E ACTN4 (blue) in the presence of 48 μM actin. The standard error is on basis of 6 repeats per condition. b) Affinity of both crosslinkers measured with a co-sedimentation assay. The standard error indicated by bars and shaded regions is on basis of the fit [Fig. 6.13]. Results were obtained at 298 K.

6.6b], quantitatively consistent with literature reports [92]. From the co-sedimentation assay and FRAP measurements we conclude that the WT crosslinker has a lower affinity for actin than the K255E mutant in the absence of force.

The high affinities of both the WT and K255E ACTN4 suggest that the majority of crosslinkers is bound at the actin concentration used in all of our experiments (48 μM). Indeed, when we spin down actin filaments in a network of 48 μM we find that virtually all crosslinkers are bound [Fig. 6.13]. This means that our network experiments target a regime where the model predicts that catch bonding is favourable [Fig. 6.4b].

The difference in crosslinker affinity for actin is also apparent in the rheological properties of actin networks crosslinked with the two variants [Fig. 6.7]. Both networks exhibit clear characteristics in their time-dependent rheology of transiently crosslinked polymer networks. For low frequencies, shorter than the crosslinker unbinding rate, both networks deform viscoelastically, with the storage and loss modulus following a power law dependence on frequency with an exponent of 1/2. This exponent arises from the superposition of multiple relaxation times of many crosslinkers connecting a single filament to the surrounding network, which collectively cause a $\omega^{-1/2}$ relaxation [37],

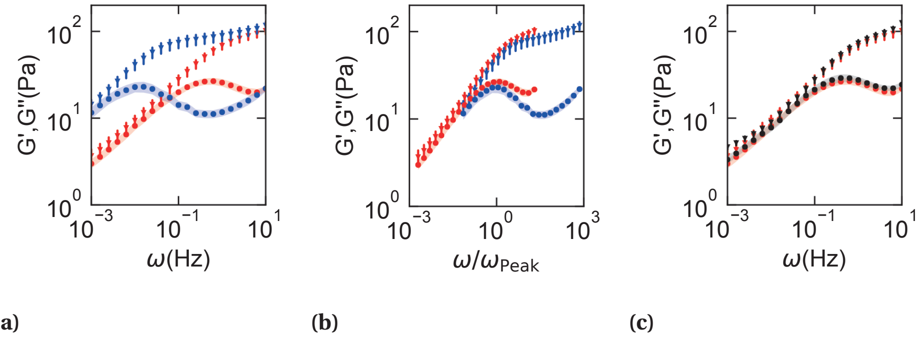

(a) **(b)** **(c)**

Figure 6.7: Time-dependent rheology of actin networks crosslinked by WT or K255E ACTN4 The storage (triangles) and loss moduli (circles and shading) were measured using small amplitude oscillatory strain. The moduli are shown as a function of frequency (a) and as a function of the frequency normalized by the frequency at which the loss modulus peaks (b). The peak frequency is 0.5 Hz for the WT (red), and 0.01 Hz for the K255E mutant (blue). Both curves are measured at 283 K. c) The time-dependent rheology of actin networks is compared between WT crosslinking at 283 K (red) and K255E crosslinking at 298 K (black). The standard error indicated by bars and shaded regions is on basis of 4 repeats per condition.

opposed to the stress relaxation observed for flexible polymer networks, which are well-described by a simple Maxwell model with a single relaxation time [72]. At the crosslinker unbinding rate, the loss modulus peaks and decreases for higher frequencies, whereas the storage modulus shows a plateau [37]. The moduli both show a slight upturn at frequencies above 5 Hz, which reflects the influence of viscous drag on the actin filaments [Fig. 6.7a].

Importantly, the WT exhibits the same dynamics as, but at a higher frequency than, the K255E mutant. By normalizing the applied frequency with the frequency at which the loss modulus peaks, both curves can be super-imposed. There is a small deviation between at high normalized frequencies, which we attribute to the effect of the viscous drag on the filaments [Fig. 6.7b]. This collapse suggests that, although the crosslinker lifetime is longer for the WT protein than for the K255E mutant, the network structure is not significantly different, as any change in for example the typical crosslinker distance would alter the absolute magnitude of the moduli of the network [37]. Indeed, with light microscopy we do not find any bundles, indicating that both networks are isotropically crosslinked [Fig. 6.17]. Furthermore, we can tune the frequency where G'' peaks for K255E crosslinked networks by increasing the temperature [Chapter 2], such that it equals the peak frequency of WT crosslinked networks at low temperature. Now, the time-dependent linear rheology of both networks is indistinguishable even without normalizing the frequency [Fig. 6.7c]. From the collapse in Fig 6.7b,c and the light microscopy [Fig. 6.17] we conclude that, even though the crosslinker lifetime is longer for the WT crosslinker than for the K255E mutant, the network structure is not significantly different.

6.3.3. ACTN4-ACTIN INTERACTIONS AT THE SINGLE-MOLECULE LEVEL

Next, we address the force-dependent binding dynamics of the two crosslinker variants at the single-molecule level by employing dual optical tweezers. We engineer a construct consisting of ACTN4 (both WT and mutant) covalently linked to a 2.5 kbp DNA handle modified with biotin, via a SFP synthase mediated reaction and a subsequent ligation (Fig. 6.8a, for details see Methods). We coat NeutrAvidin polystyrene beads with either the crosslinker construct, or with biotinylated and fluorescently labeled actin filaments [Fig. 6.8a].

Beads are optically trapped by a 1064 nm laser and we use confocal fluorescence microscopy to verify the different identities of the beads. Polystyrene beads show intrinsic autofluorescence at 532 nm laser excitation, while the labeled actin filaments can be excited with 638 nm light (Fig 6.8b). Next, we start an approaching-retracting protocol in order to establish connections between ACTN4 and actin [Fig. 6.8c, top panel]. In some occasions retraction leads to a marked increase in force [Fig. 6.8c, bottom panel], indicating the formation of a tether between an actin filament and a crosslinker. The interpretation of such events is aided by the inclusion of DNA in the construct. First, DNA serves as a spacer, reducing surface effects and unspecific binding. Indeed, the same protocol fails to create tethers when using DNA without crosslinker. Second, the DNA was specifically attached to ACTN4 close to the ABS3 domain, ensuring that the force exerted on ACTN4 by the optical tweezers is along the same direction as when ACTN4 is forced in stressed actin networks. Lastly, the well-known mechanical properties of DNA are used to discern between a single and multiple tethers (see Methods).

Tether lifetimes ranged from 40 ms to a few tens of seconds, and a portion of molecules did not break even after several minutes. Unspecific interactions between both beads likely explain the long-lived population, since we observe a similar trend for the wild-type and the mutant variants [Fig. 6.8d]. Therefore, to estimate the lifetime, we disregard the long-lived population and only consider tethers that break within 1 minute. Importantly, whereas the K255E mutant lifetime is longest at low force, wild-type ACTN4 shows a peak in the bond lifetime at an intermediate force (6 pN), characteristic of catch bond behavior. Furthermore, at this peak force, the WT and K255E mutant have similar bond lifetimes, consistent with the hypothesis that the K255E mutant is constitutively active [Fig. 6.8e].

6.3.4. FRACTURING OF ACTN4 WT AND K255E CROSSLINKED ACTIN NETWORKS

Now that we have established ACTN4 WT and the K255E mutant as an ideal model system, we test the theoretical prediction that catch bond behavior, as occurs in WT ACTN4, increases the network strength compared to constitutively active slip bond linkers such as the K255E mutant. We determine the rupture stress of crosslinked actin networks by linearly increasing the shear stress in time until the network fractures. During the stress ramp, we apply a superimposed small oscillatory oscillation to measure the differential storage modulus. We find that the differential storage modulus is constant for small stresses, but increases for larger stresses as the thermal undulations of the filaments are pulled taut [Fig. 6.9a]. This network stiffening behavior is characteristic for semiflexible

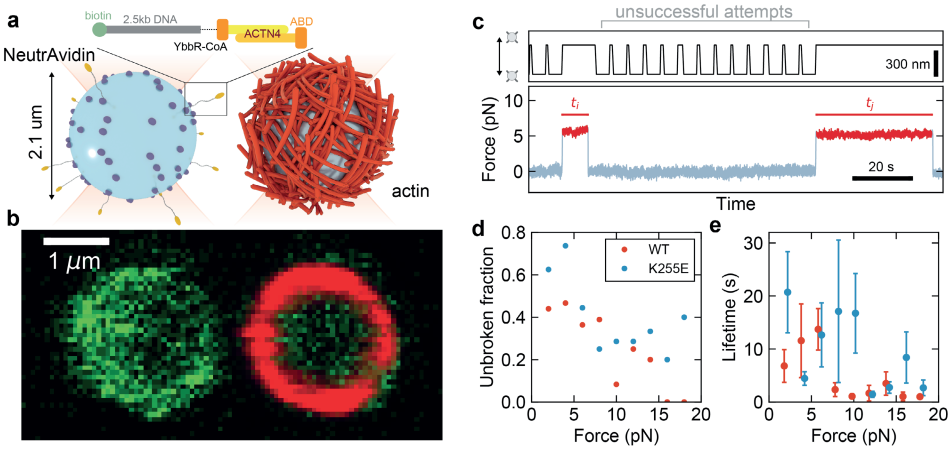

Figure 6.8: ACTN4-actin force spectroscopy reveal ACTN4 binding dynamics at the single-molecule level. a) Schematic of the force spectroscopy assay, where the interaction between an ACTN4-coated (left) and actin coated bead (right) is measured. The DNA construct attached to ACTN4 (top) aids in ascertaining the single-molecule nature of the interaction. b) Confocal scanning reveals the different bead identities. Green channel (λ=532 nm) shows the autofluorescence of polystyrene beads, while the red channel (λ=638 nm) indicates the presence of fluorescent actin on the surface of only one of the beads. c) Approaching and retracting protocol to establish ACTN4-actin connections (top). An increase in the force while retracting indicates the presence of a tether, and the lifetime is measured until the instant the tether breaks (bottom). d) Fraction of tethers that did not break after 1 minute. e) Lifetime of breaking tethers at different forces**.**

polymers such as actin [50].

At high stress, we find that the differential storage modulus precipitously drops to zero and the strain rate diverges [Fig. 6.9b], indicating rupture. Strikingly, we find that WT crosslinked networks fracture at 27 ± 3 Pa, whereas K255E networks are significantly weaker with a rupture stress of 9 ± 1 Pa [Fig. 6.9c]. We next measure the rupture stress of both types of networks at an elevated temperature (298 K instead of 283 K), such that the crosslinker unbinding rate is increased [Chapter 2]. For both types of networks, we find a lower rupture stress at the elevated temperature (from 27 ± 3 Pa to 14 ± 2 Pa for WT crosslinking and from 9 ± 1 Pa to 8 ± 1 Pa for K255E crosslinking [Fig. 6.9c, 6.18]). The lower rupture stress for networks with a higher crosslinker turnover rate is consistent with our theoretical model, where fracturing occurs due to fluctuations in the local crosslinker density. In contrast to the rupture stress, the rupture strain *increases* with temperature (from 273 ± 15 % to 847 ± 100 % for WT crosslinking and from 80 ± 5 % to 170 ± 24 % for K255E crosslinking [Fig. 6.9c, 6.18]), showing that crosslinker turnover increases the network deformability at the expense of the network strength. However, WT crosslinking yields more deformable and stronger networks than K255E crosslinking, yet consistent with the self-assembly mechanism against force-inhomogeneity offered by he catch bonding [Fig. 6.4c].

We furthermore observe that at low stress up to 1 Pa, crosslinking by WT ACTN4 results in a higher strain rate than crosslinking by the K255E mutant at the same temperature. We attribute this increased deformability to the increased crosslinker unbinding rate of the WT protein compared to the K255E mutant. However, importantly, the strain rate of WT crosslinked networks decreases as a function of stress and becomes similar to that of K255E crosslinked networks at intermediate stress [10 – 20 Pa in Fig. 6.9b]. This result strongly supports the hypothesis that the strong ABS-1 binding site is activated under network stress for the WT crosslinker, while it is constutively active for the K255E linker.

6.4. DISCUSSION

In summary, we have investigated the influence of single molecule catch bond behavior on network fracturing by a minimal 1D model combined with single molecule force spectroscopy and actin network rheology. By comparing catch bonds that undergo a force-induced activation from a weakly bound to a strongly bound state with their constitutively active slip bond counterparts, we have discovered that catch bonds enhance network strength by self-assembling against force inhomogeneity. Importantly, this catch bond advantage only emerges for macroscopically sized systems that are larger than the typical crack length, and it also requires the bonds to be close to saturation ($k_{\text{on}} \gg k_{\text{off}}$) and to be able to diffuse and redistribute after unbinding. These conditions are all satisfied in case of actin networks.

6.4.1. WT ACTN4 AND K255E AS A MODEL SYSTEM

To experimentally verify the conclusions of our theoretical model, we have used WT ACTN4 and the K255E mutant as a model system. Multiple lines of evidence show that the WT crosslinker is activated by force (catch bonding) whereas the K255E mutant is

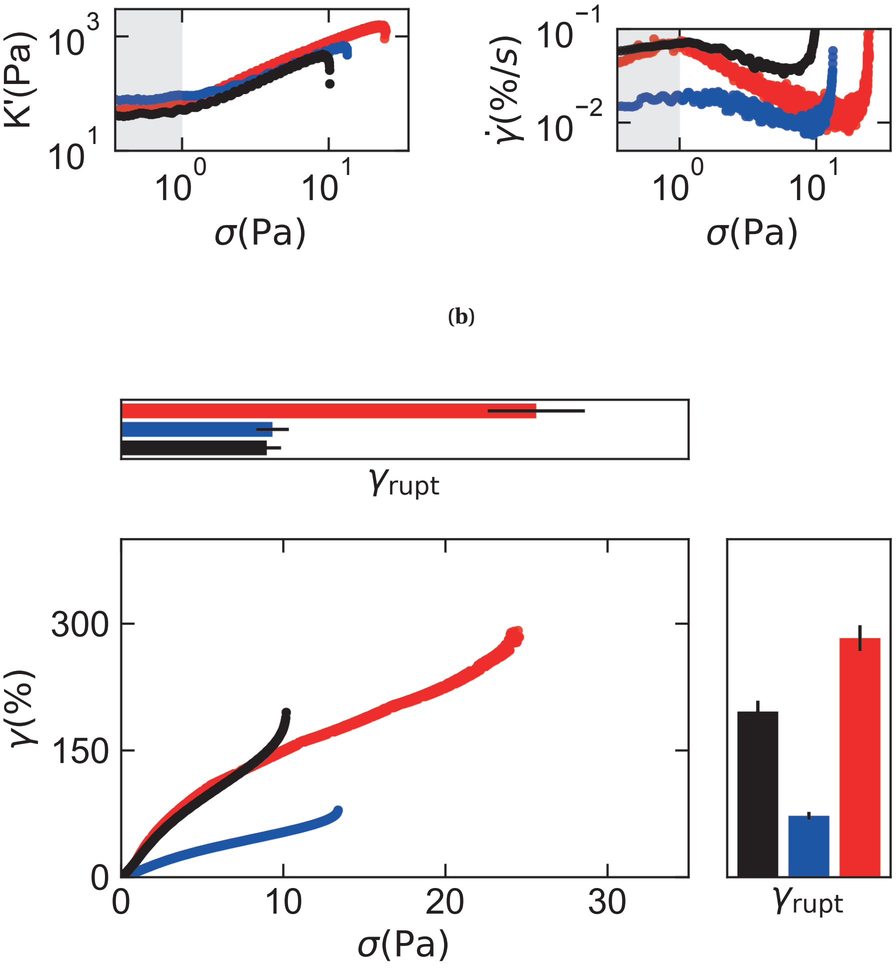

(a)

(b)

(c)

Figure 6.9: Trade-off between deformability and strength of transiently crosslinked actin networks. a) Representative example curves of the differential storage modulus measured at 0.5 Hz is plotted against the applied shear stress for actin networks crosslinked by ACTN4 WT (red), K255E (blue) or K255E at $T + 15$ K (black). We define the rupture strain as the last data point where K' exceeds the linear storage modulus. The shear rate (b) and shear strain (c) are plotted against shear stress for the same experiments. At the rupture stress, both quantities diverge. The top panel shows the average rupture stress and the right-most panel the rupture strain, with error bars representing the standard error on basis of 4 repeats per condition. All experiments are performed at a stress rate of 2.0 mPa/s.

constitutively active. First, we have found that the WT crosslinker has a lower affinity and shorter bound lifetime than the K255E mutant in the absence of force [Fig. 6.6]. Second, force spectroscopy shows that crosslinker unbinding for the WT protein slows down with force [Fig. 6.8]. Third, whereas the network shear rate is higher for WT crosslinked networks than for K255E networks, the shear rate becomes comparable for both types of crosslinkers at high stress [Fig. 6.9b].

Our findings unify a range of literature results: in living cells, mechanical experiments have revealed that WT but not K255E ACTN4 strongly localizes to actin stress fibers [84] and externally stressed areas of the actin cortex [38, 197], and that its bound lifetime increases with the application of stress [38]. In vitro experiments have shown that this increase of lifetime is intrinsic to the ACTN4-actin interaction and not due to regulatory pathways, as a similar increase of bound lifetime upon application of mechanical stress was observed in a reconstituted network consisting of only actin filaments and ACTN4 cross linkers [57]. Lastly, x-ray crystallography has identified ABS-1 as a hidden actin binding site [100] and MD-simulations have shown that this hidden binding site is exposed upon a K255E point mutation [210]. By contrast, the K255E mutant that has a constitutively exposed ABS1 domain was shown not to accumulate in stressed regions nor to increase its bound lifetime upon network stress [57, 84], suggesting that it is the exposure of the ABS1 domain upon force that is responsible for catch bonding. Summarizing, mechanical experiments on living cells [38, 197] and purified networks (Ref. [57] and Fig. 6.9b), single molecule force spectroscopy [Fig. 6.8], x-ray crystallography [100] and MD-simulations [210] all support our conclusion that the WT ACTN4 requires force to be fully active whereas the K255E mutant is constitutively active - similar to the situation that we have considered in the theoretical model [Fig. 6.1b]. Furthermore, the WT and K255E ACTN4 are mobile after unbinding [Fig. 6.6a] and operate close to saturation [Fig. 6.6b, Fig. 6.13]. Therefore, we conclude that the WT and K255E ACTN4 crosslinkers are an ideal model system to test our theoretical predictions.

6.4.2. ALTERNATIVE MECHANISMS

We propose, based on the consistency experiment and theory, that ACTN4 reinforces actin networks by catch bonding. There were earlier hints in the literature that networks crosslinked by WT might be stronger than K255E-networks, but this was never systematically explored [81]. Moreover, the increased rupture stress of WT crosslinking was attributed to the higher crosslinker unbinding rate compared to the K255E mutant, based on an idea that the lower crosslinker unbinding rate of the K255E mutant might prevent homogeneous stress redistribution and subsequent network remodeling [81]. However, by performing stress ramps at different temperatures we show that an increased unbinding rate actually leads to a *decreased* rupture stress [Fig. 6.9c, Fig. 6.18].

Another alternative explanation that has been put forward recently, on basis of cell stretching experiments, is that K255E ACTN4 networks are more brittle than WT ACTN4 networks due to a difference in network structure between both types of crosslinking [115]. However, the collapse observed in the time-dependent rheology [Fig. 6.7, 6.18] and the light microscopy data [Fig. 6.17] we observe suggest that the network structure in our experiments is not significantly different between both types of crosslinking. Our work suggests that the larger strength can be ascribed exclusively to catch bonding of

WT ACTN4.

6.4.3. FUTURE EXPERIMENTS

Our theoretical model makes several predictions that can be tested experimentally. Firstly, the network lifetime can be measured as a function of the applied stress. When a constant stress is applied, the model predicts that catch bond crosslinking should allow for a network lifetime that is orders of magnitude longer than slip bond crosslinking at low stress, but that networks have a similar rupture time at high stress [Fig. 6.2a]. Secondly, it would be interesting to consider recently developed mechanical experiments on networks as small as only a few bonds [213, 214], rather than the macroscopic networks as measured with rheology. This way, the theoretical prediction can be verified that catch bonding only improves the network strength for macroscopically sized systems [Fig. 6.2b]. Lastly, the theoretical model predicts that catch bonds increase the robustness via a self-assembly mechanism against force inhomogeneity [Fig. 6.3a]. Recent advances in fluorescent force sensors enable measuring the force per crosslinker [215]. In principle, by combining such force sensors with single molecule fluoresence techniques [216], the distribution of linker forces can be measured and compared between WT and K255E crosslinking. Whilst such experiments would be non-trivial to perform, it would allow for a detailed verification of the self-assembly mechanism proposed by the theoretical model.

6.4.4. RELEVANCE

Catch bonds are widespread in biology, and can be found in virtually any system of cellular adhesion and in many biopolymer networks including the cytoskeleton (table 6.1). In all these cases, mechanical force is distributed over many bonds and the bonds diffuse after unbinding - as described by our simple theoretical model. The functional relevance of catch bonds is often viewed in the context of mechanosensing, where the force-induced conformational transition could serve as a read-out for force [156, 197, 206]. Our results imply another, non-exclusive, possibility, namely that catch bonds evolved to prevent fracturing.

We have found two examples in biology where a mutation that turns the linker from a catch bonds into a constitutively active slip bonds leads to cell or tissue fragility. Indeed, the first example is the actin crosslinker α-actinin-4 and the K255E mutant as investigated here. Remarkably, the K255E point mutation causes a disease known as focal segmental glomerulosclerosis type 1 that is associated with brittle cells and kidney failure [57, 211]. The second example is the platelet adhesion glycoprotein Ibα mutant R1450E, which causes a disease known as von Willebrand disease type 2B [217–219]. Here, blood cells expressing the mutant vWD a1 are incapable of forming stable blood clots under flow, leading to excessive bleeding [219]. Again the mutant has a longer single molecule bound lifetime in absence of force while the lifetime approaches that of the wild type in the presence of force [217, 218]. Our work suggests a new physical mechanism to explain these diseases.

Outside biology, catch bonds provide an intriguing new biomimetic design principle towards smart materials. Typically materials trade deformability for strength [193], whereas many applications, especially in regenerative medicine [220], require both features. The strength of dynamic materials can be improved by the addition of permanent bonds [179, 221], but this greatly limits the deformability. Our findings show that catch bonds uniquely combine the advantages of enhanced deformability *and* strength of materials. Furthermore, unlike other bio-mimetic routes towards robust materials, which rely on hierarchically structured materials across several length scales [193, 222], molecular catch bonding is a single-length design principle. This makes the future design of synthetic materials relatively straightforward and modular, as it only relies on the molecular structure of the linker. Synthetic analogues of catch bonds have recently been discovered [223] and provide an excellent starting point towards highly dynamic yet strong biomimetic materials.

We thank Mario Avellaneda and Sander Tans for performing the single molecule experiments. We thank Martin van Hecke and Celine Alkemade for critical reading of the chapter. We thank Pieter Rein ten Wolde, Kees Storm, Wouter Ellenbroek, Chase Broedersz, David Brueckner and Mareike Berger for fruitful discussions. We thank Marjolein Kuit-Vinkenoog for actin and ACTN4 purification, and Vanda Sunderlikova for design, mutagenesis, cloning and purifying of the ACTN4 constructs used in the single molecule experiments.

APPENDIX

EXPERIMENTAL METHODS

SDS-PAGE GEL PROTOCOL AND QUANTIFICATION

SDS-PAGE gels were used to characterize and quantify purified proteins. In all cases, $20\,\mu$l sample was mixed with $20\,\mu$l InstantBlue and boiled at $95\,^{o}$C for 5 minutes in a closed Eppendorf vial. $30\,\mu$l of this solution was loaded onto a 4–15 % Mini-PROTEAN TGX™ Precast Protein Gel with 10 wells of 30 µl. Gels were run for 30 minutes at 200 V, washed with miliq water, stained overnight with InstantBlue and washed three times with tap water. Band intensities were quantified using ImageJ. Background correction was applied to all band intensities by subtracting the average intensity of a region adjacent to the band of interest.

PROTEIN PURIFICATION

The actin crosslinker human α-actinin 4 (the wild type variant and its mutant counterpart K255E) was purified as described in reference [98]: E. Coli cells were transformed to express recombinant crosslinkers with a 6xhis-tag. Induction was performed with 500 μM isopropyl β-D-1-thiogalactopyranoside for eight hours at $25\,^{o}$C. After centrifugation at 6000 g for 15 minutes, cells were resuspended in 20 mM NaCl, 5 mg/ml lysozyme and 20 mM Hepes, pH 7.8. The cells were lysed by a freeze-thaw cycle, and centrifuged at 20,000 g for 30 min. The recombinant proteins were purified from the supernatant using a QIAGEN nickel column. Next, the column was washed with 20-bed columns of 500 mM NaCl, 25 mM imidazole, and 20 mM Hepes, pH 7.8. The recombinant proteins were eluted with 10-bed volumes of 500 mM NaCl, 500 mM imidazole, and 20 mM Hepes, pH 7.8. The proteins were concentrated using Centricon (Millipore) and purified by gel filtration in 150 mM NaCl, 20 mM Hepes pH 7.8, and 10 mM dithiothreitol (DTT).

To ensure we use the same concentration of the WT and K255E ACTN4, we determined the ratio of stock concentrations by measuring the band intensity of both types of crosslinkers on a SDS-PAGE gel. We chose this method over determining the protein concentration by the absorbance of the stock solution at 280 nm, as with the SDS-PAGE gel we specifically measure the protein of interest and exclude the contribution of contaminants [Fig. S5]. WT and K255E ACTN4 were labeled on cysteine using maleimide-activated Oregon Green at a ratio of five fluorophores for every crosslinker at room temperature for 1 h. Labeled proteins were separated from free dyes by gel filtration using Superdex 200 (GE Healthcare) [98].

Actin was purified from rabbit psoas skeletal muscle as described in reference [99]. The concentration was determined by measuring the absorbance at 280 nm. Aliquots were stored at $-80\,^{o}$C in G-buffer (2 mM tris-hydrochloride pH 8.0, 0.2 mM disodium adenosine triphosphate, 0.2 mM calcium chloride, 0.2 mM dithiothreitol) to prevent

Figure	σ	N	$k^{\text{slip}}_{\text{off},0}$	$k^{\text{catch}}_{\text{off},0}$	$f^{\text{catch}}_{1/e}$
1c	0.485	10^3	10^{-2}	10^{-1}	0.4
2b	0.35	$1-10^3$	10^{-1}	0.4	0.8
3a	0.22	10^3	10^{-2}	10^{-1}	0.4
3b	0.22	10^3	10^{-2}	10^{-1}	0.4
S1b	1.35	$1-10^3$	10^{-2}	10^{-1}	1.5
4a	0.7	10^3	10^{-2}	$10^{-1.5}-10^{0.5}$	$10^{-1}-10$
4b	0.5	10^3	$10^{-2}-10$	$k^{\text{slip}}_{\text{off},0}\cdot 10$	0.4

Table 6.2: Table of parameters used for network simulations. In all simulations, we use $k_{\text{on}} = 1$ and $f^{\text{catch}}_{1/e} = 1$. The catch bond advantage was more pronounced at lower stresses [Fig. 2a]. However the computation time quickly diverges below the critical stress and simulating network rupture times below the critical stress therefore quickly becomes computationally intractable. We had to optimize σ per figure: small enough to have a clearly visible difference between catch and constitutively active slip bonds, and large enough to observe network fracturing in computationally feasible timescales.

polymerization. After thawing, we store G-actin stock samples overnight at 4 ^{o}C. The next day, we spin the sample at 120 000 g to spin down any aggregates. We store the supernatant at 4 ^{o}C for maximum of 7 days before use. Unless otherwise mentioned, we used a concentration of 48 μM, corresponding to 2 mg/ml, for all our experiments and actin was polymerized in an F-buffer consisting of 50 mM KCl, 20 mM imidazole pH 7.4, 2 mM MgCl_2, 1 mM DTT and 0.5 mM MgATP. Unless otherwise mentioned, we used a crosslinker concentration of 0.48 μM to obtain a molar ratio of 1/100 crosslinker/actin and on average around 1 crosslinker per 0.5 μm of actin filament; under these conditions, networks are isotropic [Fig. S8].

FLUORESCENCE RECOVERY AFTER PHOTOBLEACHING

The lifetime of bound crosslinkers was measured via Fluorescence Recovery After Photobleaching (FRAP) using a Nikon A1 confocal microscope with a perfect focus system and a 100x oil immersion objective using a 100-mW 488 nm argon ion laser. The FRAP protocol started with 10 images to determine baseline fluorescence. Next, bleaching was performed by using a high intensity laser power such that $50-70$ % of the fluorescence intensity was bleached in 0.5 seconds. The fluorescence recovery was tracked during a period of approximately 5x the typical recovery time, with a sampling rate that halved every 10 frames, starting with 10 frames/second. Unless otherwise mentioned, a circular area was bleached of 2 μm radius and an equally sized area was used as a reference. The laser intensity during imaging was chosen such that the reference intensity dropped less than 5 % during the recovery phase.

To extract a timescale for recovery. τ_{FRAP}, the normalized intensity during recovery I/I_{ref} was fitted with a single exponential function $I/I_{\text{ref}} = 1 - I_0/I_{\text{ref}} \cdot \exp(-\frac{t}{\tau})$, where I_0 is the intensity directly after bleaching. The timescale of recovery (hereafter named k_{FRAP}) is defined by the typical crosslinker diffusion time, which scales quadratically with the bleach radius, and the typical crosslinker unbinding time, which is independent of the

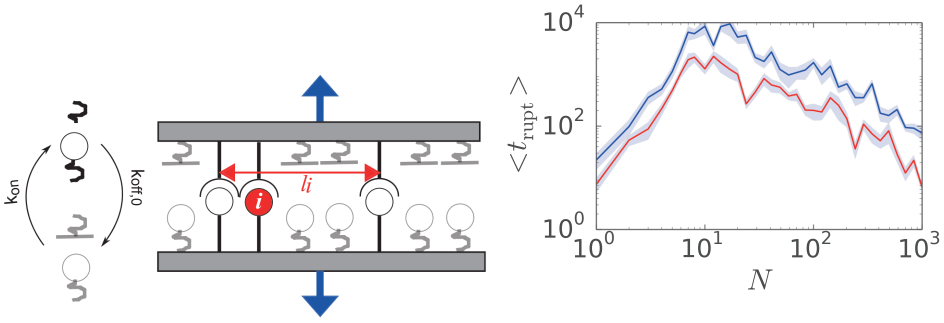

(a) **(b)**

Figure 6.10: System size dependence of rupture time for networks connected by immobile linkers. a) Schematic of a model with immobile linkers that always (re-)bind in the same location. b) The rupture time of networks connected by immobile linkers shows a biphasic dependence on system size, similar to networks connected by mobile linkers [Fig. 2b], but catch bonds networks (red) are less long-lived than constitutively active slip bond networks (blue) for any value of N.

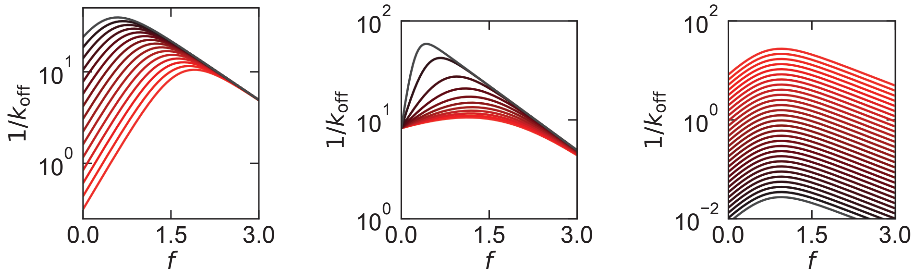

(a) **(b)** **(c)**

Figure 6.11: Force-lifetime curves for various parameters. Exemplary catch bond curves used to generate the data presented in Fig. 4a,b. The following parameter ranges were used: $10^{-1.5} \le k^{\text{catch}}_{\text{off},0} \le 10^{0.5}$ in 11 logarithmically spaced steps (a), $10^{-1} \le f^{\text{catch}}_{1/e} \le 10^{1}$ in 15 logarithmically spaced steps (b) and $10^{-1} \le \frac{k_{\text{on}}}{k^{\text{slip}}_{\text{off},0}} \le 10^{1}$ in 30 logarithmically spaced steps (c). All graphs are color coded in black for the lowest value and red for the highest value.

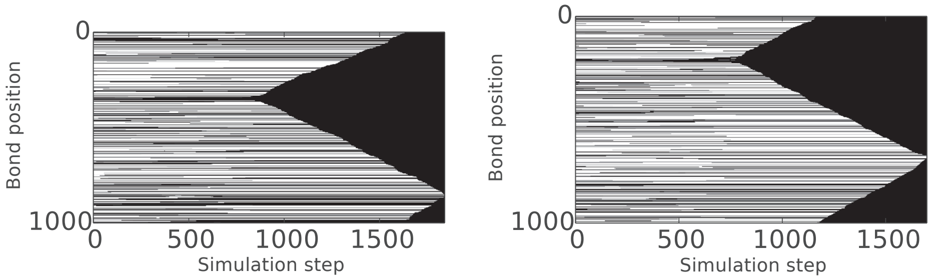

Figure 6.12: Kymographs of spontaneous crack initiation. Example kymograph showing the last 1700 simulation steps before fracturing of the slip (a) and catch (b) bond networks fracturing as presented in Fig. 1c. The fracture behavior is similar for both types of networks, except that cracks initiate less frequently for catch bond networks.

bleach radius. To dissect these two contributions, we compared the recovery time for different bleach radii, $2\,\mu$m and $4\,\mu$m. We did not find a statistically significant difference. We conclude that the FRAP recovery timescale is dominated by the typical crosslinker unbinding time, as any contribution of the diffusion timescale would have increased as a function of bleach area. This result is consistent with a calculation where we estimate that the typical diffusion distance during the typical fluorescent recovery timescale is significantly is larger than the FRAP radius (2μm) for both the WT ($40\,\mu$m) and the K255E mutant ($365\,\mu$m) . We used a diffusion constant based on the Stokes-Einstein relationship, assuming a crosslinker radius of 3 nm on basis of the crystal structure [100]).

CO-SEDIMENTATION ASSAY

A volume of $25\,\mu$l monomeric (G-)actin at increasing concentrations was co-polymerized with actin binding proteins in F-buffer at room temperature, keeping the actin binding protein (WT or K255E ACTN4) concentration constant ($0.1\,\mu$M). After two hours of polymerization the actin network together with the bound crosslinkers was spun down at 120 000 g. Afterwards, $20\,\mu$l was gently pipetted from the supernatant and run on an SDS-PAGE gel as described above. The fraction of bound linkers ϕ_{bound} was determined by subtracting and normalizing the ACTN4 band intensity at a particular actin concentration by the band intensity in the absence of actin: $\phi_{\text{bound}} = \frac{I-I_0}{I_0}$.

RHEOLOGY

Rheology was performed using a stress-controlled Kinexus Malvern Pro rheometer with a stainless steel 20 mm radius cone plate geometry with a 1^o degree angle. We loaded $40\,\mu$l of the ACTN4 cross linked actin networks directly after mixing the proteins into the polymerization buffer. A thin layer of Fluka mineral oil Type A was added around the geometry to prevent evaporation, and the sample was closed off with a hood to minimize effects of air flow. Polymerization of the network was followed by applying a small oscillatory shear with a strain amplitude of 0.5 % and a frequency of 0.5 Hz. After 2 h of

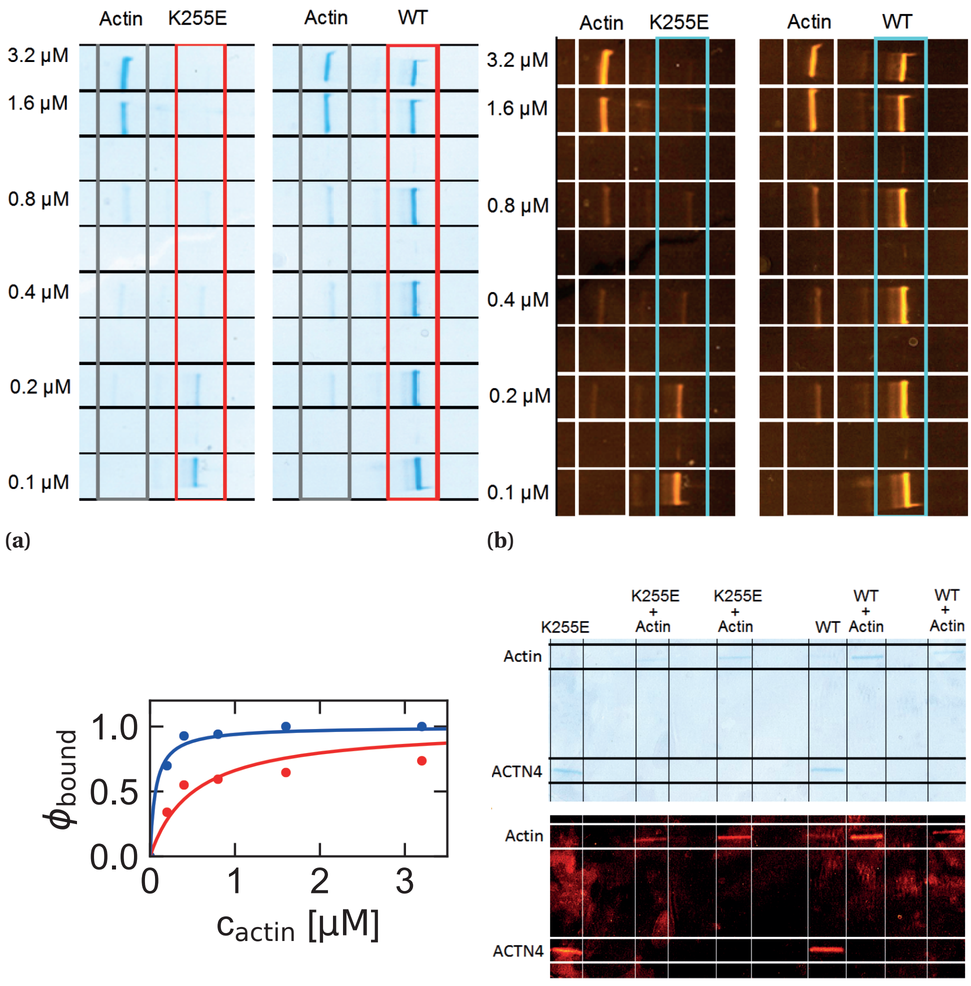

(a) (b)

(c) (d)

Figure 6.13: High-speed co-sedimentation. The supernatant resulting from a high-speed centrifugation of a mixture of actin filaments and crosslinkers was run on a SDS-page gel. The right band shows the WT or K255E ACTN4 (100 kDa) and the left band shows actin (42 kDa). Each channel contains a different actin concentration. a) shows the raw image whereas b) shows the same image with enhanced contrast via post-acquisition processing. c) The fraction of bound linkers as determined from the co-sedimentation assay as a function of the actin concentration was fit using $\phi_{\text{bound}} = \frac{c_{\text{actin}}}{K}$, where K is the affinity of the crosslinker. d) Co-sedimentation of WT and K255E ACTN4 was performed in the presence and absence of 48 μM actin (the concentration used in all network experiments). In the presence of an actin network, neither WT nor K255E ACTN4 could be detected in the supernatant. The top panel shows the raw image, the bottom panel shows same image with enhanced contrast via post-acquisition processing.

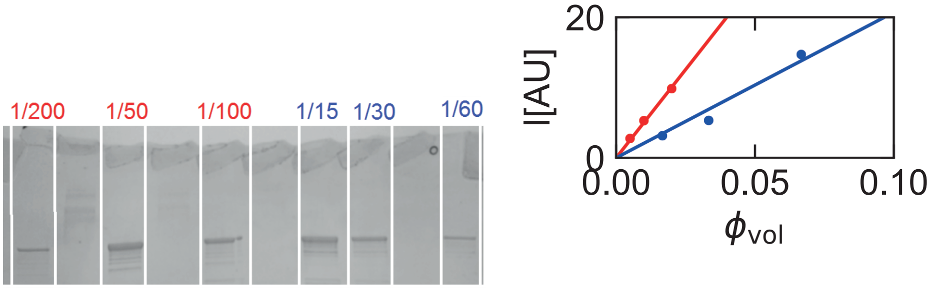

(a) **(b)**

Figure 6.14: Determination of the WT/K255E ratio in stock concentration. a) SDS-PAGE gel of the WT (red) and K255E (blue) at several different volume fractions. The brightest band in every channel shows the undegraded ACTN4 (WT or K255E). b) Quantification of the band intensity as a function of the undegraded crosslinker as a function of the volumetric fraction shows that the WT ACTN4 stock concentration is 2.5x more concentrated compared to the K255E stock concentration. Therefore, we dilute the WT ACTN4 2.5x more in all our network experiments to ensure that the same final concentration is used for both types of crosslinkers.

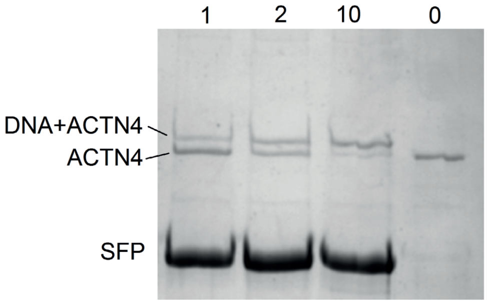

Figure 6.15: ACTN4-DNA coupling. DNA was coupled to ACTN4 to prepare the single molecule constructs. We performed coupling reactions at several different molar ratios of DNA:ACTN4. These samples were run on a SDS-PAGE gel to measure the degree of coupling. The DNA:ACTN4 molar ratios is indicated on top of each band. We find that the fraction of coupled ACTN4 monomers increases with the amount of DNA added to the solution. At a molar ratio of 1:1, most of the ACTN4 is uncoupled.

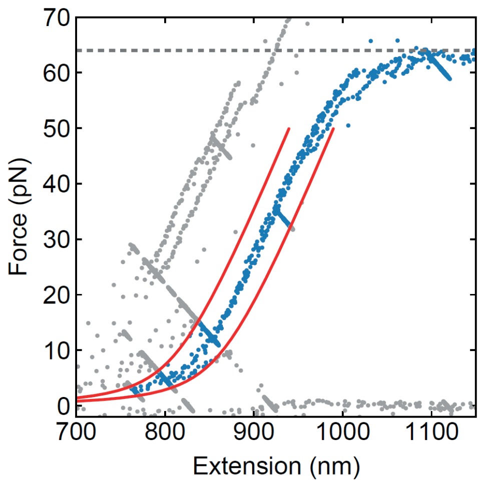

Figure 6.16: Classification criterion for single tethers. Force-extension curves revealed a force plateau between 63 and 65 pN that is characteristic of dsDNA [224] (dashed line). This was used as the criterion to classify tethers as single connections. Due to the uncertainty on bead radii and actin layer thickness, we generated two WLC models with contour lengths 25 nm shorter and longer than the theoretical 850 nm (red lines). Data lying within this range that broke in a clean step (and showed DNA overstretching when reaching 65 pN if pulled) was regarded as single tethers (blue dots), otherwise the data were discarded (grey dots).

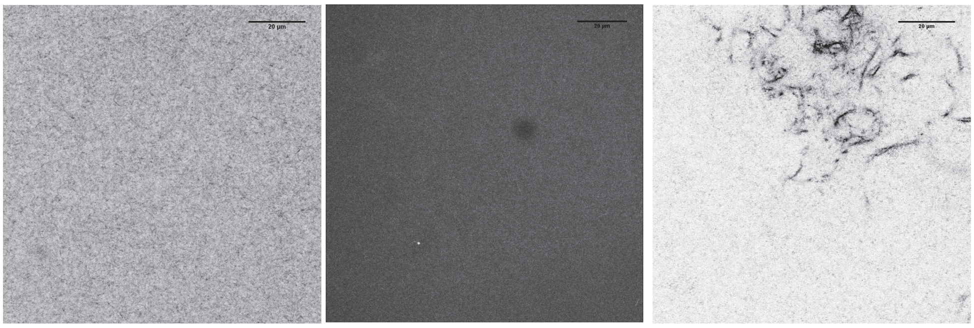

(a) **(b)** **(c)**

Figure 6.17: Confocal fluorescence images of ACTN4 crosslinked actin networks At a 1:100 crosslinker:actin molar ratio, the concentration used for all experiments in this manuscript, an isotropically crosslinked actin network is observed with no structure above the diffraction limit for both WT (a) and K255E ACTN4 (b). c) For comparison, actin bundles were observed at a 1:25 ACTN4:actin molar ratio. The color coding was inverted for both images to improve the visual contrast between bundles and background. Scale bars are 20 μm.

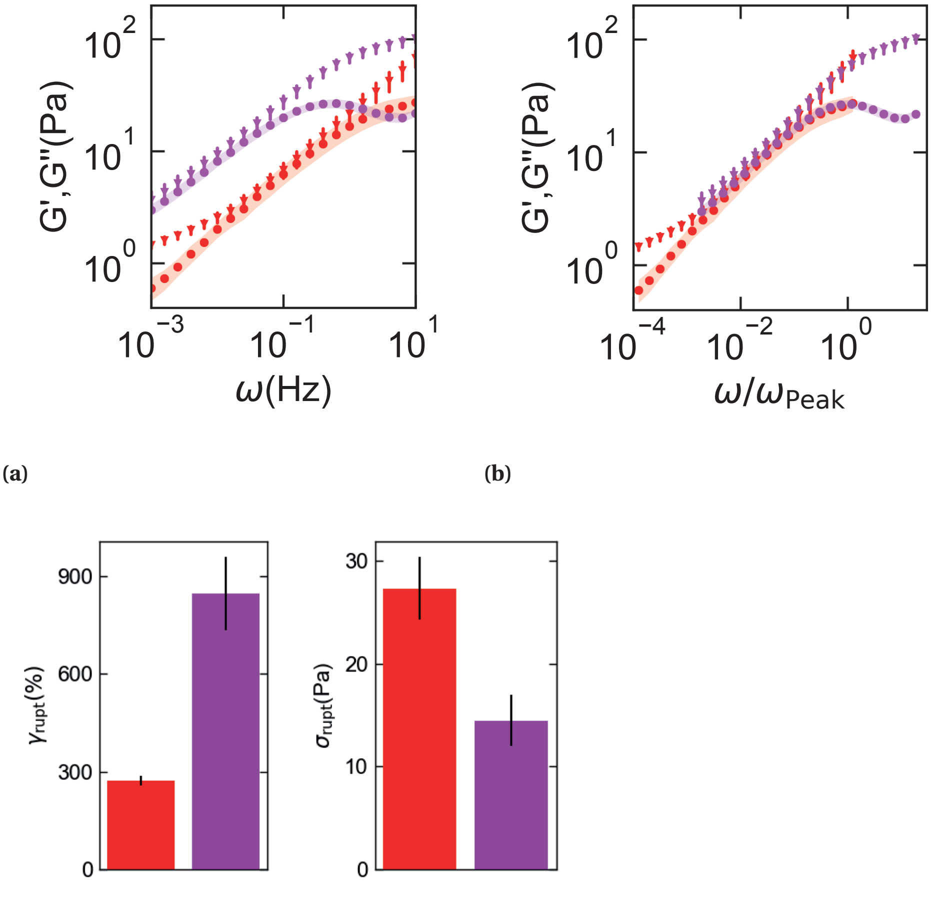

(a) **(b)**

(c) **(d)**

Figure 6.18: Comparison between WT crosslinked actin networks at different temperatures. The storage (triangles) and loss moduli (circles and shading) were measured using small amplitude oscillatory strain. The moduli are shown as a function of frequency (a) and as a function of the frequency normalized by the frequency at which the loss modulus peaks (b). The peak frequency is $8\,Hz$ at $298\,K$ (red), and $0.5\,Hz$ at $283\,K$ (magenta). The average rupture strain (c) and rupture stress (d) was measured at a stress rate of 2.0 mPa/s. The error bars indicated vertical lines and shaded regions represent the standard error on basis of 4 repeats.

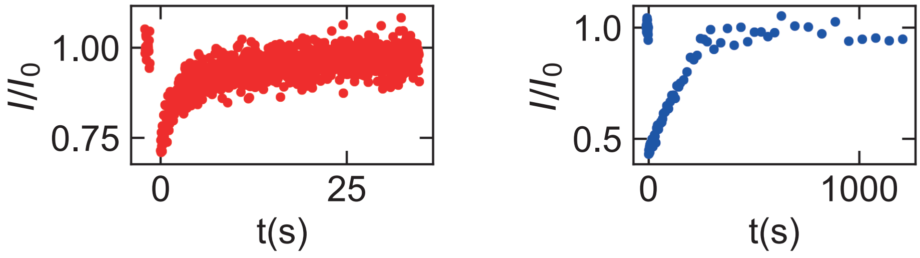

(a) **(b)**

Figure 6.19: Examplary FRAP curves. The intensity of fluorescently labeled crosslinkers normalized by the intensity before bleaching as a function time. The moment of bleaching is defined as t=0. The intensity asymptotically approaches the pre-bleach intensity for both WT (a) and K255E ACNT4 (b), suggesting that all linkers are mobile.

polymerization, a frequency sweep was performed between 0.01 – 10 Hz, using 10 data points per decade. Frequencies above 10 Hz could not be measured as inertial effects from the rheometer dominated the rheological response of the actin network at high frequencies. Then, we perform a fracturing experiment by linearly increasing the stress in time (2 mPa/s), until the network fractures.We define the rupture point as the last data point at which the differential storage modulus exceeds the linear modulus [Fig. 9a].

SINGLE MOLECULE FORCE SPECTROSCOPY

SINGLE-MOLECULE CONSTRUCTS GENERATION

The wild-type crosslinker and the K255E mutant were modified to include a ybbR tag (DSLEFIASKLA) [225] right after the His-tag. Purified proteins were coupled to 20 nucleotide Coenzyme A-modified DNA oligonucleotides using a phosphopantetheinyl transferase (SFP)-mediated reaction [225]. A protein to DNA molar ratio of 10:1 ensured that coupling mostly occurred only on one monomer, as evidenced by SDS-PAGE analysis [Fig. S6]. Next, 2.5 kbp DNA tethers were PCR amplified from the pUC19 plasmid (New England Biolabs) with a biotinylated primer on one side and a phosphoprimer on the other side. Purification was done with the QIAquick PCR purification kit (Qiagen, Hilden, Germany). The phosphorylated strand was digested by Lambda exonuclease (New England Biolabs) for 2 hours at 37 degrees Celsius and purified using a Amicon 30 kDa MWCO filter (Merck, Darmstadt, Germany). Deep Vent exo-DNA polymerase (New England Biolabs) and a 20 nucleotide more upstream primer than the phosphoprimer from the PCR was used to fill up the second DNA strand, creating a 20 nt overhang (details on the single molecule constructs will be published elsewhere). This overhang is complementary to the 20 nt oligonucleotide sequence coupled to the proteins. The generated DNA tether was then ligated to the DNA-protein hybrid using T4 ligase (New England Biolabs) and incubated overnight at room temperature.

Preparation of actin coated beads Actin monomers were mixed with biotinylated actin monomers and actin monomers labeled with AlexaFluor 647 in a molar ratio of 8:1:1 and polymerized into filaments in 1 mL F-buffer at a concentration of 2 μM for 2 hours. Next, these filaments were mixed with 4 μl of 2.4 μM Neutravidin-coated beads (NVP-20-5, diameter 2.1 μm, Spherotech) and incubated for 15 minutes to couple the filaments to the beads. The actin-coated beads were washed from unbound filaments by centrifuging 3x at 1000 rcf for 2 minutes. After every round, 800 μl of supernatant was discarded, whilst carefully avoiding to disturb the pellet, and replaced by 800 μl of fresh F-buffer. Successful coating was verified using confocal fluorescence microscopy by the presence of a fluorescent ring on the edge of the bead upon excitation with a 638 nm laser.

Single molecule data acquisition and analysis Data was collected at 500 Hz using a custom-built dual trap optical tweezers [226] and a commercial C-Trap (Lumicks). Tethers were classified as single if the extension-force characteristics were similar to molecules that showed DNA overstretching and only if they ruptured in a clean single step [Fig. S7]. The theoretical contour length of the construct is 850 nm, however we found an increase in length from the force-extension curve expected for DNA of $50-200$ nm, which we attribute to the actin coating. We shifted the extension so that overstretching curves matched a worm-like chain of 850 nm contour length. Then we considered an additional uncertainty margin of 50 nm and every point falling within this range was assigned as a single tether [SI fig. 7].

COMPUTATIONAL MODEL

To investigate the effect of molecular catch bonding on the strength of transient networks, we harness a computational model we recently developed to predict failure of transient networks [97, 173]. We consider a 1D model of N linkers which share an externally applied load (Fig. 1a). We define σ as the applied load normalized by the system size N and bond force sensitivity $f_{1/e}$. We use a Gillespie algorithm to model stochastic linker binding and unbinding [157]. Bound linkers unbind with a rate that depends on the applied local force $k_{\text{off}}(f)$, as detailed in Eq. 2, and rebind with a rate k_{on}. To take into account the mobility after unbinding of linkers like integrins or actin binding proteins, which diffuse in resp. the membrane or cytosol, we allow for unbound linkers to rebind at a random new location. The stress σ is inhomogeneously distributed over the bonds, $f_i = \alpha_i \cdot \sigma$, where f_i is the force and α_i the stress intensity factor per bond. Previously we found that although microscopic systems (approximately $N < 100$) are relatively insensitive to the distribution of load sharing, macroscopic systems fail via stress localization [97, 173]. We model this stress localization by assuming that α depends on the distance of a bond to its nearest neighbors on both sides, specifically: $\alpha_i = \frac{l_i}{\Sigma_i l_i}$ [Fig. 1a]. We use a periodic boundary condition to prevent edge effects. To simulate catch bonds and their corresponding constitutively active slip bonds, we model the bond force sensitivity as a single exponential for slip bonds [142] and as a sum of two exponents for catch bonds [116] [Fig. 1b] according to Eq. 1. We initialize networks by randomly placing $N \cdot K$ linkers, where K is the bond affinity, $K = \frac{k_{\text{on}}}{k_{\text{on}} + k_{\text{off},0}}$.

7

OUTLOOK - SYNTHESIS AND MECHANICAL CHARACTERIZATION OF A MINIMAL CELL MODEL

In this work we have extensively studied the mechanics and dynamics of actin networks as a model system for cellular mechanics. The advantage of such reconstituted networks over studying living cells is that they allow for quantitative control over the composition. Furthermore, the mechanics of reconstituted networks are readily investigated experimentally by using rheometers. As a result, both historically and in this thesis, reconstituted networks have played a crucial role in understanding the mechanics of biopolymer networks. However, the physical principles governing cellular mechanics are undeniably more complex than that of reconstituted biopolymer networks. For example, actin cortices are confined by the plasma membrane. As actin filaments have a persistence length that is typically on the order of the cell size (approximately 10 μm), this confinement induces internal stresses in the actin cortex [227]. Furthermore, actin filaments interact with the plasma membrane via anchoring proteins such as ezrin, radixin and moesin which transiently bind both actin and the plasma membrane [228]. In this outlook, we develop a model system to study the mechanics of an actin cortex transiently connected to and confined by a spherical, cell-sized lipid membrane. We measure the efficiency of protein encapsulation in these liposomes, and characterize the membrane. Lastly and most importantly, we develop mechanical tools to allow for mechanical investigation of these minimal cells. This outlook provides an important step in bridging the gap between rheology on simplified reconstituted networks and cellular mechanics.

Buffer and lipids - unless otherwise mentioned, all aqueous solutions contain 50 mM KCl, 20 mM imidazole pH 7.4, 2 mM MgCl_2, 1 mM DTT and 0.5 mM MgATP (F-buffer). Furthermore, the solution inside liposomes is enriched with 300 mM sucrose to create a density difference with the outer solution required for centrifugation as explained below. We observed the highest number of liposomes after centrifugation when the osmolarity inside the liposome was 10 mM higher compared to the outer solution. Therefore, the outer solution contained 290 mM glucose

. We used the following lipids: 1,2-dioleoyl-sn-glycero-3-phosphocholine (*DOPC*, zwitter-ionic), 1,2-dioleoyl-sn-glycero-3-phospho-L-serine (*DOPS*, negatively charged), 1-oleoyl-2-{12-[(7-nitro-2-1,3-benzoxadiazol-4-yl)amino]dodecanoyl}-sn-glycero-3-phosphoserine (*NBD-PS*, negatively charged and fluorescent), 1-Oleoyl-2-[12-[(7-nitro-2-1,3-benzoxadiazol-4-yl)amino]dodecanoyl]-sn-Glycero-3-Phosphocholine (*NBD-PC*, negatively charged and zwitter-ionic) and 1,2-dioleoyl-sn-glycero-3-[(N-(5-amino-1-carboxypentyl)iminodiacetic acid)succinyl] (*DGS-NTA*, binds His-tags). Lastly, we used the water-soluble dye pyranine (8-Hydroxypyrene-1,3,6-Trisulfonic Acid, Trisodium Salt) (HPTS). All lipids were ordered from Avanti Polar Lipids and stored in chloroform in glass vials at $-20\,^{o}$C. All chemicals were ordered from Sigma Aldrich.

We create liposomes using the Inverted Emulsion method [229] (IE). First, $500\,\mu$l mineral oil Type A solution containing 0.5 mg/ml DOPC lipids is layered on top of $125\,\mu$l water solution and incubated for 1 h to create a lipid monolayer at the oil water interface. This bottom water solution will become the aqueous phase surrounding the liposomes. Next, $15\,\mu$l of water is mixed with $500\,\mu$l oil containing 0.5 mg/ml lipids by pipetting the emulsion up and down. The water droplets will become the inner solution of the liposomes. Importantly, the inner solution has a density that is 50 mg/ml higher than the outer solution whilst having a similar osmotic pressure. This density mismatch is achieved by encapsulating sucrose. Glucose, which has half the molecular weight of sucrose, is added to the outer aqueous phase to match the osmolarity between the inner and outer solution. Lastly, we centrifuge the inverted emulsion through the incubated water-oil interface to yield a solution of liposomes for 10 minutes at 300 rcf [Fig. 7.1a]. Compared to other methods of protein encapsalution in liposomes [21], IE is experimentally straightforward and allows quantitative control over the encapsulated mixture by tuning the composition of the water used to create the emulsion [Fig. 7.1b].

A downside of the inverted emulsion method is that residual oil from the emulsion might get trapped between the leaflets of the liposomes [230]. Oil defects affect the mechanics of liposomes [230], and therefore complicate interpretation of mechanical experiments on minimal cells. To test whether oil is present in the liposomes, we use several assays. First, we test whether membrane pore proteins can be incorporated in the membrane. As pore proteins have a well-defined transmembrane length of only a few nanometers, the presence of oil is detrimental to pore protein functioning [231]. We find that the addition of pore proteins to the outer solution of the membrane rapidly causes release of encapsulants [Fig. 7.2a], suggesting that at least part of the membrane is thin enough to accommodate for the pore protein. Next, we compare liposomes made by inverted emulsion to liposomes made by electroformation (EF) as explained in Ref. [232]. The downside of electroformation is that, unlike inverted emulsion, it cannot be used to encapsulate proteins at physiological salt conditions, however the advantage is that no oil is required in the formation of liposomes. Therefore, electroformed liposomes serve as an oil-free benchmark. We compare the fluorescence intensity between EF liposomes with IE liposomes, both containing 0.1 % rho-PE fluorescent tracer lipids. Any residual oil in IE membranes should cause an increase of fluorescence, as fluorescent lipids are dissolved at high concentrations. However, we find that the fluorescence intensity of IE and EF liposomes is similar [Fig. 7.2c]. Lastly, we check for the presence of oil by measuring the flip-flop rate of NBD-PC lipids. These lipids exchange between the inner and outer leaflet (flip-flop) due to thermal motion, and this process is likely affected by residual oil. We measure the rate of flip-flop rate by adding dithionite to the outer solution.,

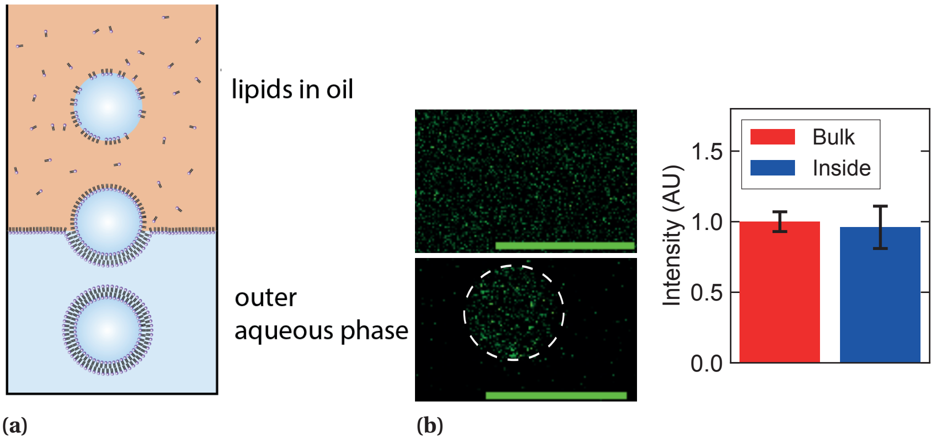

Figure 7.1: Liposomal encapsulation. a) Schematic of the Inverted Emulsion method [229] used to encapsulate actin in liposomes. b) The fluorescence intensity per voxel of 0.05 μM encapsulated GFP-labeled Drosophila septin hexamers [24] (bottom - a white dashed lined shows the location of the liposome, the outer solution does not contain septin) was compared with the same concentration of GFP labeled septin in bulk (top). The scale bar is 20 μm. No statistically significant difference was found, suggesting 100% encapsulation efficiency (error bar on basis of 5 images per condition).

which exclusively bleaches NBD-PC present on the outer leaflet and lipids present on the inner leaflet only bleach after flip-flopping [233]. Using this technique, we find a flip-rate on the order of 30 minutes [Fig. 7.2d], comparable to reports in literature on pure lipid membranes [231, 233, 234]. Taken together, the incorporation of pore proteins, comparison to electroformed liposomes and flip-flop assay suggest that no significant fraction of residual oil is present in the membrane of liposomes created by the inverted emulsion method under our experimental conditions.

Now that we have asserted IE-formed liposomes as a suitable platform for creating minimal cells, we set out to create an actin cortex by encapsulating actin together with moesin, a membrane anchoring protein [235]. When actin and moesin are incorporated in a liposome that only contains neutral lipids, neither protein colocalizes with the membrane. Instead, actin is depleted from the edges - which indicates that actin is filamentous [Fig. 7.3a]. To anchor the actin filaments via His-tagged moesin to the membrane, we include nickel-NTA lipids and observe strong membrane localization of both moesin and actin [Fig. 7.3b]. For future work, this assay can serve as an ideal model system for a minimal cell containing an actin cortex. Furthermore, we demonstrate control over the type of actin structures inside the liposome. By adding Polyethylene glycol-35K as a crowding agent we can obtain actin bundles [Fig. 7.3c] and rings [Fig. 7.3d] which resemble stress fibers of adherent cells [22] and the actin ring of dividing cells [[24]].

We have shown that we can create minimal cells with anchored actin cortices [Fig. 7.3b]. However, whereas mechanical experiments are readily performed on mm-sized reconstituted actin networks, it is significantly more difficult to physically manipulate

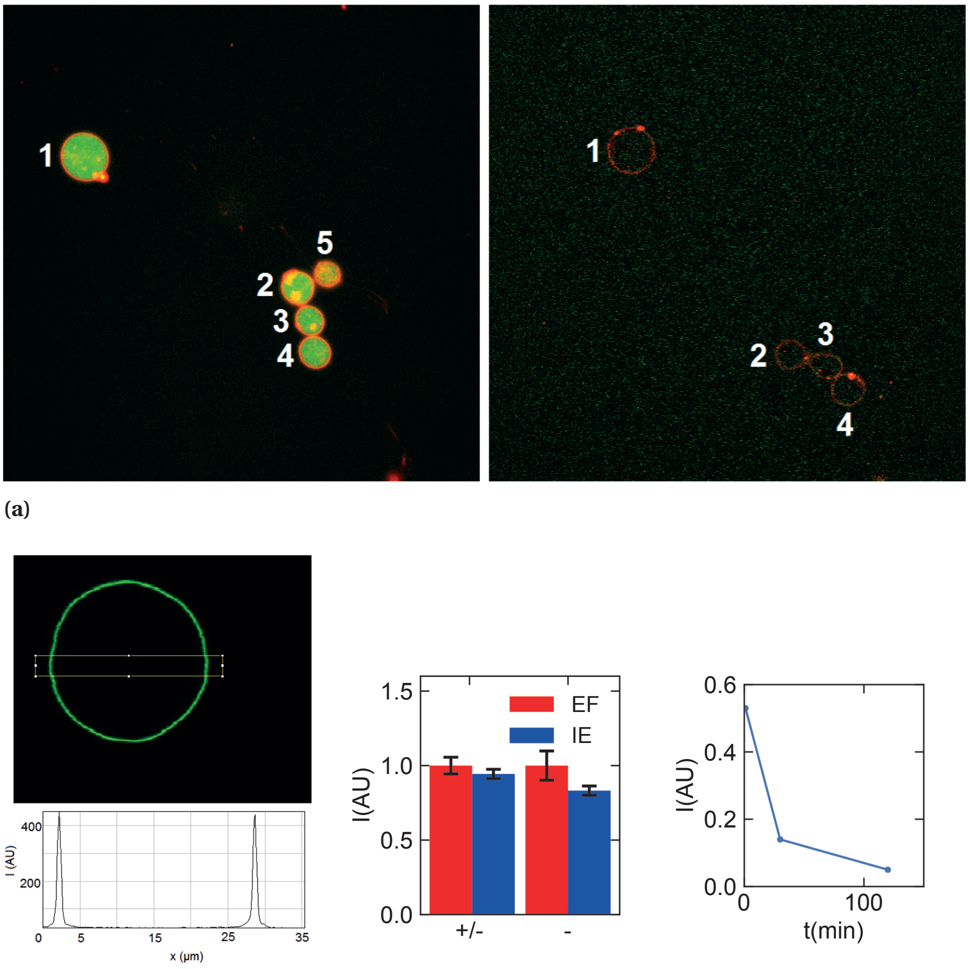

(a)

(b) (c) (d)

Figure 7.2: Membrane characterization. a) Liposomes (red) containing 1 mM of the water-soluble dye HPTS (green) were imaged before (left) and 10 s after the addition of the membrane pore protein melittin (0.05 mg/ml). Note that one liposome drifted away due to the mixing of melittin. The field of view for both images is 128x128μm. b) The membrane fluorescence intensity (0.5 mole-percent NBD-PC) was measured by drawing a box over the liposome and taking the peak fluorescence intensity. c) Comparison of the membrane fluorescence intensity per voxel between liposomes made with electroformation (EF) and inverted emulsion (IE) for both zwitterionic 1-palmitoyl-2-oleoyl-sn-glycero-3-phosphocholine and negatively charged 1-palmitoyl-2-oleoyl-sn-glycero-3-phospho-L-serine lipids (error bars represent the standard error on basis of 5 liposomes per condition). d) The fluorescence membrane intensity normalized by the intensity before addition of dithionite as a function of time after addition of dithionite.

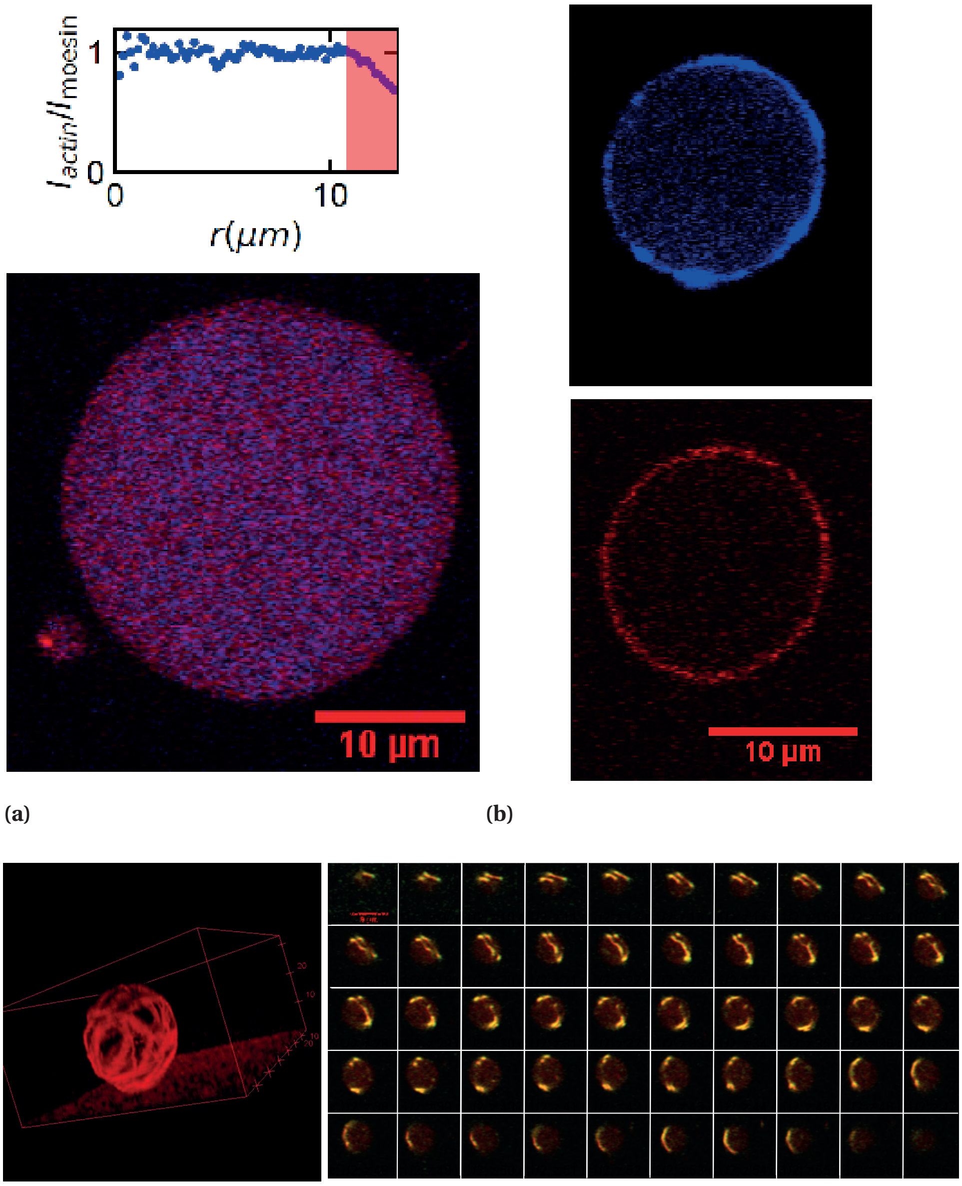

(a) (b)

(c) (d)

Figure 7.3: Minimal cell model with various actin architectures. We encapsulate 24 μM actin and 1 μM moesin in F-buffer inside liposomes. a) In the absence of membrane anchoring, actin (blue) nor moesin (red) colocalizes to the surface of the liposome. Top: radial integration of the actin fluorescence normalized by the moesin intensity as a function of the cell radius shows that actin is depleted from the outer 3 μm. b) In the presence of 1 % Ni-NTA lipids, moesin binds to the membrane via its His tag and subsequently recruits actin. In the presence of 50 mg/ml PEG-35K, crowding causes actin bundling (c - 3D reconstruction, 60 μm x 60 μm x 25 μm) and sometimes rings are observed (d - z-slices). The distance between each z-slice in (d) is 0.2 μm and field of view of 16 μm x 16 μm.

(minimal) cells due to their small size. In order to be able to perform mechanical measurements on these minimal cells, we have developed the 'minicel microscope' which combines optical tweezers with laser ablation and micropipette aspiration [Fig. 7.4]. Here, we present proof-of-principle data that demonstrates how optical tweezers and micropipette aspiration can be used to manipulate and ultimately mechanically characterize minimal cells.

Using micromanipulators, we position a home-forged micropipette in the vicinity of a liposome. We then suck in a liposome using a pressure controller attached to the micropipette. The tongue length can be studied as a function of the applied pressure to probe the mechanical properties of minicells [Fig. 7.5a,b]. Furthermore, using optical tweezers and a polystyrene bead we are able to pull a membrane tube from a liposome [Fig. 7.5c,d]. Next, we can measure the force required to pull the tube as a function of the applied pressure with the micropipette and/or as a function of the tube length. Micropipette aspiration and membrane tube pulling provide complementary information on the mechanics of these minimal cells, so different contributions of the actin cortex to cell mechanics can thereby be dissected. For example, the actin cortex is significantly deformed upon micropipette aspiration [197, 236]. In contrast, membrane tube pulling does not affect the shape of the cortex, and the anchor-mediated friction between the actin and the membrane can be measured by pulling tubes at different rates [237]. For future work, it will be interesting to obtain mechanical data for minimal cells with varying types of actin cortices, for example by including contractile actomyosin activity, to gain deeper insight into how the actin cytoskeleton contributes to cellular mechanics.

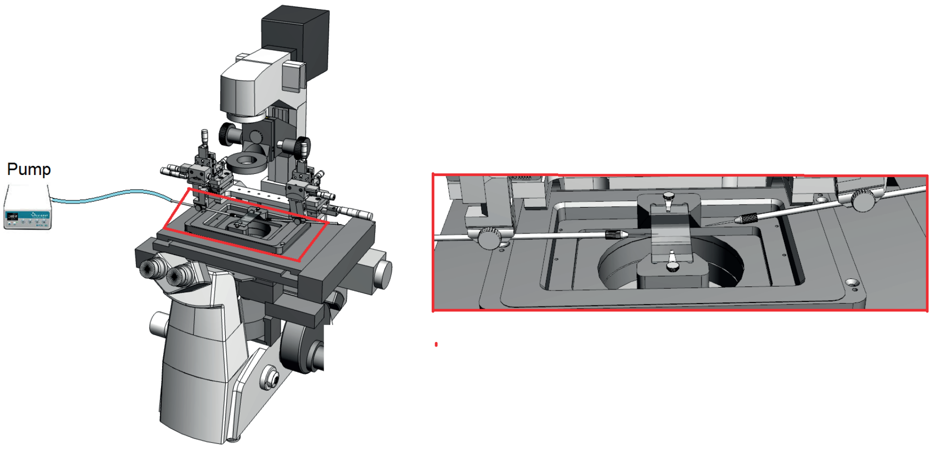

(a)

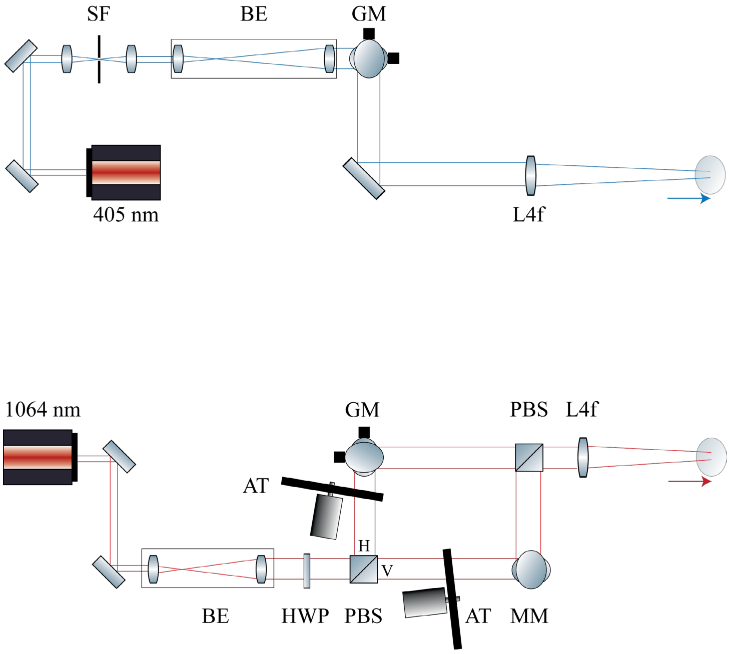

(b)

Figure 7.4: Minicel microscope. a) Drawing of microscope base and the micropipette aspiration pump with a zoom in on the micropipettes and sample holder. Two micropipettes are installed to allow for micropipette aspiration with one pipette, whilst simultaneously injecting compounds into or next to the liposome with the other micropipette. b) Schematic of optics for laser ablation and optical tweezers. SF=spatial filter, BE=beam expander, GM=galvo mirror, L4f=4f lens, HWP=half wave plate, PBS=polarizing beam splitter, AT=motorized attenuator and MM=manually steerable mirror. We acknowledge Alexander Franzen's ComponentLibrary under the Creative Commons license for the schematics of the optical components.

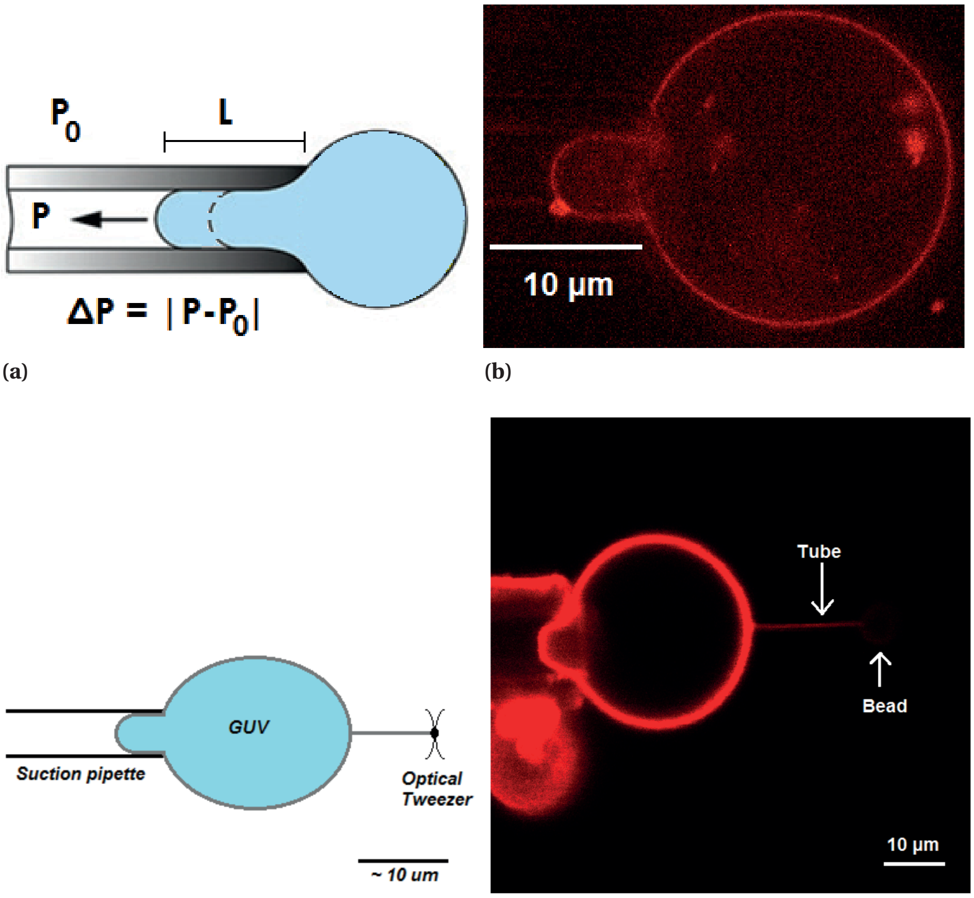

(a) (b) (c) (d)

Figure 7.5: Towards mechanical characterization of minimal cells. a) Schematic of micropipette aspiration experiment. b) Confocal microscopy image of a liposome deformed by micropipette aspiration. d) Schematic of tether pulling experiment e) Confocal microscopy image of a membrane tube pulled by an optical tweezer from a liposome held by micropipette aspiration. The bright spots in the lower left corner are lipids stuck to the micropipette.

We thank Jan Bonne Aans for the design and implementation of the laser ablation and optical tweezers and Marko Kamp for input during discussions, Brahim Ait Said, Marco Konijnenburg and Marco Seynen for the software development, Henk-Jan Boluit for the design and the AMOLF workshop for manufacturing of the micropipette aspiration and Marjolein Kuit-Vinkenoog for protein purification. Furthermore, we thank Patricia Bassereau, Aurelie Bertin, Stephanie Mangenot, Alexandre Beber, Sven Boots and Poul Bendix for their help with the tether pulling experiment. Lastly, we thank Sven Boots and George Jenkinson for their help with the micropipette aspiration.

BIBLIOGRAPHY

[1] B.-C. Chen, W. R. Legant, K. Wang, L. Shao, D. E. Milkie, M. W. Davidson, C. Janetopoulos, X. S. Wu, J. A. Hammer, Z. Liu, B. P. English, Y. Mimori-Kiyosue, D. P. Romero, A. T. Ritter, J. Lippincott-Schwartz, L. Fritz-Laylin, R. D. Mullins, D. M. Mitchell, J. N. Bembenek, A.-C. Reymann, R. Böhme, S. W. Grill, J. T. Wang, G. Seydoux, U. S. Tulu, D. P. Kiehart, and E. Betzig, *Lattice light-sheet microscopy: Imaging molecules to embryos at high spatiotemporal resolution,* Science **346**, 1257998 (2014).

[2] C. Roubinet, P. T. Tran, and M. Piel, *Common mechanisms regulating cell cortex properties during cell division and cell migration.* Cytoskeleton (Hoboken, N.J.) **69**, 957 (2012).

[3] A. Zoumi, A. Yeh, and B. J. Tromberg, *Imaging cells and extracellular matrix in vivo by using second-harmonic generation and two-photon excited fluorescence,* Proceedings of the National Academy of Sciences **99**, 11014 (2002).

[4] G. Salbreux, G. Charras, and E. Paluch, *Actin cortex mechanics and cellular morphogenesis.* Trends in cell biology **22**, 536 (2012).

[5] O. M. Lancaster and B. Baum, *Shaping up to divide: Coordinating actin and microtubule cytoskeletal remodelling during mitosis,* Seminars in Cell and Developmental Biology **34**, 109 (2014).

[6] R. McBeath, D. M. Pirone, C. M. Nelson, K. Bhadriraju, and C. S. Chen, *Cell Shape, Cytoskeletal Tension, and RhoA Regulate Stem Cell Lineage Commitment,* Developmental Cell **6**, 483 (2004).

[7] H. Jiang and S. X. Sun, *Cellular pressure and volume regulation and implications for cell mechanics.* Biophysical journal **105**, 609 (2013).

[8] T. Lecuit, P.-F. Lenne, and E. Munro, *Force generation, transmission, and integration during cell and tissue morphogenesis.* Annual review of cell and developmental biology **27**, 157 (2011).

[9] A. J. Grodzinsky, M. E. Levenston, M. Jin, and E. H. Frank, *Cartilage Tissue Remodeling in Response to Mechanical Forces,* Annual Review of Biomedical Engineering **2**, 691 (2000).

[10] L. Casares, R. Vincent, D. Zalvidea, N. Campillo, D. Navajas, M. Arroyo, and X. Trepat, *Hydraulic fracture during epithelial stretching,* Nature Materials **14**, 343 (2015).

[11] C. M. Denais, R. M. Gilbert, P. Isermann, A. L. McGregor, M. te Lindert, B. Weigelin, P. M. Davidson, P. Friedl, K. Wolf, and J. Lammerding, *Nuclear envelope rupture and repair during cancer cell migration,* Science **352**, 353 (2016).

[12] A. C. Martin, M. Gelbart, R. Fernandez-Gonzalez, M. Kaschube, and E. F. Wieschaus, *Integration of contractile forces during tissue invagination,* Journal of Cell Biology **188**, 735 (2010).

[13] J. M. Henderson, M. P. Alexander, and M. R. Pollak, *Patients with ACTN4 mutations demonstrate distinctive features of glomerular injury.* Journal of the American Society of Nephrology : JASN **20**, 961 (2009).

[14] E. Paluch, M. Piel, J. Prost, M. Bornens, and C. Sykes, *Cortical actomyosin breakage triggers shape oscillations in cells and cell fragments,* Biophysical Journal **89**, 724 (2005).

[15] K. Carvalho, F.-C. Tsai, L. Edouard, V. Raphael, G. H. Koenderink, F. Zhang, S. J. Morley, and C. Sykes, *Cell-sized liposomes reveal how actomyosin cortical tension drives shape change,* Proceedings of the National Academy of Sciences **110**, 19968 (2013).

[16] E. Abu Shah and K. Keren, *Symmetry breaking in reconstituted actin cortices,* eLife **3**, e01433 (2014).

[17] J. Sedzinski, M. Biro, A. Oswald, J. Y. Tinevez, G. Salbreux, and E. Paluch, *Polar actomyosin contractility destabilizes the position of the cytokinetic furrow,* Nature **476**, 462 (2011).

[18] E. K. Paluch and E. Raz, *The role and regulation of blebs in cell migration,* Current Opinion in Cell Biology **25**, 582 (2013).

[19] U. G. K. Wegst and M. F. Ashby, *The mechanical efficiency of natural materials,* Philosophical Magazine **21**, 2167 (2004).

[20] F. Huber, A. Boire, M. P. López, and G. H. Koenderink, *Cytoskeletal crosstalk: when three different personalities team up,* Current Opinion in Cell Biology **32**, 39 (2015).

[21] Y. Mulla, A. Aufderhorst-Roberts, and G. Koenderink, *Shaping up synthetic cells,* Physical Biology , aab923 (2018).

[22] U. S. Schwarz and S. a. Safran, *Physics of adherent cells,* Reviews of Modern Physics **85**, 1327 (2013).

[23] J.-Y. Tinevez, U. Schulze, G. Salbreux, J. Roensch, J.-F. Joanny, and E. Paluch, *Role of cortical tension in bleb growth,* Proceedings of the National Academy of Sciences **106**, 18581 (2009).

[24] M. Mavrakis, Y. Azou-Gros, F.-C. Tsai, J. Alvarado, A. Bertin, F. Iv, A. Kress, S. Brasselet, G. H. Koenderink, and T. Lecuit, *Septins promote F-actin ring formation by crosslinking actin filaments into curved bundles.* Nature cell biology **16** (2014), 10.1038/ncb2921.

[25] A. J. Ridley, M. a. Schwartz, K. Burridge, R. a. Firtel, M. H. Ginsberg, G. Borisy, J. T. Parsons, and A. R. Horwitz, *Cell migration: integrating signals from front to back.* Science (New York, N.Y.) **302**, 1704 (2003).

[26] R. Milo, P. Jorgensen, U. Moran, G. Weber, and M. Springer, *BioNumbers—the database of key numbers in molecular and cell biology,* Nucleic Acids Research **38**, D750 (2010).

[27] I. Hanukoglu, N. Tanese, and E. Fuchs, *Complementary DNA Sequence of a Human Cytoplasmic Actin,* Journal of Molecular Biology **163**, 673 (1983).

[28] A. F. Niddam, R. Ebady, A. Bansal, A. Koehler, B. Hinz, and T. J. Moriarty, *Plasma fibronectin stabilizes Borrelia burgdorferi –endothelial interactions under vascular shear stress by a catch-bond mechanism,* Proceedings of the National Academy of Sciences **114**, E3490 (2017).

[29] L. R. Otterbein, P. Graceffa, and R. Dominguez, *The Crystal Structure of Uncomplexed Actin in the ADP State,* Science **293**, 708 (2001).

[30] L. Blanchoin, R. Boujemaa-Paterski, C. Sykes, and J. Plastino, *Actin Dynamics, Architecture, and Mechanics in Cell Motility,* Physiological Reviews **94**, 235 (2014).

[31] M.-F. Carlier and S. Shekhar, *Global treadmilling coordinates actin turnover and controls the size of actin networks,* Nature Reviews Molecular Cell Biology , 389 (2017).

[32] T. D. Pollard, *Actin and Actin-Binding Proteins,* Cold Spring Harbor Perspectives in Biology **8**, a018226 (2016).

[33] K. Kasza, F. Nakamura, S. Hu, P. Kollmannsberger, N. Bonakdar, B. Fabry, T. Stossel, N. Wang, and D. Weitz, *Filamin A Is Essential for Active Cell Stiffening but not Passive Stiffening under External Force,* Biophysical Journal **96**, 4326 (2009).

[34] F. Eghiaian, A. Rigato, and S. Scheuring, *Structural, Mechanical, and Dynamical Variability of the Actin Cortex in Living Cells,* Biophysical Journal **108**, 1330 (2015).

[35] G. H. Koenderink, Z. Dogic, F. Nakamura, P. M. Bendix, F. C. MacKintosh, J. H. Hartwig, T. P. Stossel, and D. A. Weitz, *An active biopolymer network controlled by molecular motors.* Proceedings of the National Academy of Sciences of the United States of America **106**, 15192 (2009).

[36] M. Murrell, P. W. Oakes, M. Lenz, and M. L. Gardel, *Forcing cells into shape: the mechanics of actomyosin contractility,* Nature Reviews Molecular Cell Biology **16**, 486 (2015).

[37] C. P. Broedersz, M. Depken, N. Y. Yao, M. R. Pollak, D. A. Weitz, and F. C. MacKintosh, *Cross-Link-Governed Dynamics of Biopolymer Networks,* Physical Review Letters **105**, 238101 (2010).

[38] E. S. Schiffhauer, T. Luo, K. Mohan, V. Srivastava, X. Qian, E. R. Griffis, P. A. Iglesias, and D. N. Robinson, *Mechanoaccumulative Elements of the Mammalian Actin Cytoskeleton,* Current Biology **26**, 1473 (2016).

[39] C. P. Broedersz and F. C. MacKintosh, *Modeling semiflexible polymer networks,* Reviews of Modern Physics **86**, 995 (2014).

[40] L. Laan, N. Pavin, J. Husson, G. Romet-Lemonne, M. Van Duijn, M. P. López, R. D. Vale, F. Jülicher, S. L. Reck-Peterson, and M. Dogterom, *Cortical dynein controls microtubule dynamics to generate pulling forces that position microtubule asters,* Cell **148**, 502 (2012).

[41] M. P. Koonce, J. Tong, U. Euteneuer, and M. Schliwa, *Active sliding between cytoplasmic microtubules.* Nature **328**, 737 (1987).

[42] G. Çolakoğlu and A. Brown, *Intermediate filaments exchange subunits along their length and elongate by end-to-end annealing,* The Journal of Cell Biology **185**, 769 (2009).

[43] L. Kreplak, H. Herrmann, and U. Aebi, *Tensile Properties of Single Desmin Intermediate Filaments,* Biophysical Journal **94**, 2790 (2008).

[44] J. Block, H. Witt, A. Candelli, E. J. Peterman, G. J. Wuite, A. Janshoff, and S. Köster, *Nonlinear Loading-Rate-Dependent Force Response of Individual Vimentin Intermediate Filaments to Applied Strain,* Physical Review Letters **118**, 1 (2017).

[45] M. Biro, Y. Romeo, S. Kroschwald, M. Bovellan, A. Boden, J. Tcherkezian, P. P. Roux, G. Charras, and E. K. Paluch, *Cell cortex composition and homeostasis resolved by integrating proteomics and quantitative imaging.* Cytoskeleton (Hoboken, N.J.) **754**, 741 (2013).

[46] M. Bezanilla, A. S. Gladfelter, D. R. Kovar, and W.-L. Lee, *Cytoskeletal dynamics: A view from the membrane,* The Journal of Cell Biology **209**, 329 (2015).

[47] J. van der Gucht, E. Paluch, J. Plastino, and C. Sykes, *Stress release drives symmetry breaking for actin-based movement,* Proceedings of the National Academy of Sciences **102**, 7847 (2005).

[48] F. C. MacKintosh, J. Käs, and P. A. Janmey, *Elasticity of Semiflexible Biopolymer Networks,* Physical Review Letters **75**, 4425 (1995).

[49] C. Semmrich, R. J. Larsen, and A. R. Bausch, *Nonlinear mechanics of entangled F-actin solutions,* Soft Matter **4**, 1675 (2008).

[50] C. Storm, J. J. Pastore, F. C. MacKintosh, T. C. Lubensky, and P. A. Janmey, *Nonlinear elasticity in biological gels,* Nature **435**, 191 (2005).

[51] M. L. Gardel, J. H. Shin, F. C. MacKintosh, L. Mahadevan, P. Matsudaira, and D. A. Weitz, *Elastic behavior of cross-linked and bundled actin networks.* Science (New York, N.Y.) **304**, 1301 (2004).

[52] O. Lieleg, M. M. a. E. Claessens, Y. Luan, and a. R. Bausch, *Transient binding and dissipation in cross-linked actin networks,* Physical Review Letters **101**, 1 (2008).

[53] L. Wolff, P. Fernandez, and K. Kroy, *Inelastic mechanics of sticky biopolymer networks,* New Journal of Physics **12** (2010), 10.1088/1367-2630/12/5/053024.

[54] M. Gralka and K. Kroy, *Inelastic mechanics: A unifying principle in biomechanics,* Biochimica et Biophysica Acta (BBA) - Molecular Cell Research **1853**, 3025 (2015).

[55] M. Maier, K. W. Müller, C. Heussinger, S. Köhler, W. a. Wall, a. R. Bausch, and O. Lieleg, *A single charge in the actin binding domain of fascin can independently tune the linear and non-linear response of an actin bundle network,* The European Physical Journal E **38**, 50 (2015).

[56] O. Lieleg, K. M. Schmoller, M. M. A. E. Claessens, and A. R. Bausch, *Cytoskeletal polymer networks: Viscoelastic properties are determined by the microscopic interaction potential of cross-links,* Biophysical Journal **96**, 4725 (2009).

[57] N. Y. Yao, C. P. Broedersz, M. Depken, D. J. Becker, M. R. Pollak, F. C. MacKintosh, and D. a. Weitz, *Stress-Enhanced Gelation: A Dynamic Nonlinearity of Elasticity,* Physical Review Letters **110**, 018103 (2013).

[58] B. Guo and W. H. Guilford, *Mechanics of actomyosin bonds in different nucleotide states are tuned to muscle contraction,* Proceedings of the National Academy of Sciences **103**, 9844 (2006).

[59] D. L. Huang, N. A. Bax, C. D. Buckley, W. I. Weis, and A. R. Dunn, *Vinculin forms a directionally asymmetric catch bond with F-actin,* Science **357**, 1 (2017).

[60] T. T. Falzone, M. Lenz, D. R. Kovar, and M. L. Gardel, *Assembly kinetics determine the architecture of α-actinin crosslinked F-actin networks,* Nature Communications **3**, 861 (2012).

[61] J. Schnauß, T. Golde, C. Schuldt, B. U. S. Schmidt, M. Glaser, D. Strehle, T. Händler, C. Heussinger, and J. A. Käs, *Transition from a Linear to a Harmonic Potential in Collective Dynamics of a Multifilament Actin Bundle,* Physical Review Letters **116**, 108102 (2016).

[62] K. M. Schmoller, P. Fernández, R. C. Arevalo, D. L. Blair, and a. R. Bausch, *Cyclic hardening in bundled actin networks,* Nature Communications **1**, 134 (2010).

[63] K. M. Schmoller, O. Lieleg, and A. R. Bausch, *Internal stress in kinetically trapped actin bundle networks,* Soft Matter **4**, 2365 (2008).

[64] P. M. McCall, F. C. MacKintosh, D. R. Kovar, and M. L. Gardel, *Cofilin Drives Rapid Turnover and Fluidization of Entangled F-actin,* bioRxiv , 1 (2017).

[65] D. Humphrey, C. Duggan, D. Saha, D. Smith, and J. Käs, *Active fluidization of polymer networks through molecular motors.* Nature **416**, 413 (2002).

[66] M. P. Murrell and M. L. Gardel, *F-actin buckling coordinates contractility and severing in a biomimetic actomyosin cortex,* Proceedings of the National Academy of Sciences **109**, 20820 (2012).

[67] N. L. Dasanayake, P. J. Michalski, and A. E. Carlsson, *General Mechanism of Actomyosin Contractility,* Physical Review Letters **107**, 118101 (2011).

[68] J. M. Belmonte, M. Leptin, and F. Nédélec, *A theory that predicts behaviors of disordered cytoskeletal networks,* Molecular Systems Biology **13**, 941 (2017).

[69] V. Wollrab, J. M. Belmonte, M. Leptin, F. Nedelec, and G. H. Koenderink, *Polarity sorting drives remodeling of actin-myosin networks,* bioRxiv (2018), 10.1101/314484.

[70] J. R. Blundell and E. M. Terentjev, *Stretching Semiflexible Filaments and Their Networks,* Macromolecules **42**, 5388 (2009).

[71] Y. C. Lin, N. Y. Yao, C. P. Broedersz, H. Herrmann, F. C. MacKintosh, and D. A. Weitz, *Origins of elasticity in intermediate filament networks,* Physical Review Letters **104**, 1 (2010).

[72] S. C. Grindy, M. Lenz, and N. Holten-Andersen, *Engineering Elasticity and Relaxation Time in Metal-Coordinate Cross-Linked Hydrogels,* Macromolecules **49**, 8306 (2016).

[73] B. Fabry, G. N. Maksym, J. P. Butler, M. Glogauer, D. Navajas, and J. J. Fredberg, *Scaling the Microrheology of Living Cells,* Physical Review Letters **87**, 148102 (2001).

[74] P. Bursac, G. Lenormand, B. Fabry, M. Oliver, D. A. Weitz, V. Viasnoff, J. P. Butler, and J. J. Fredberg, *Cytoskeletal remodelling and slow dynamics in the living cell,* Nature Materials **4**, 557 (2005).

[75] C. Semmrich, T. Storz, J. Glaser, R. Merkel, A. R. Bausch, and K. Kroy, *Glass transition and rheological redundancy in F-actin solutions,* Proceedings of the National Academy of Sciences **104**, 20199 (2007).

[76] K. Kroy and J. Glaser, *The glassy wormlike chain,* New Journal of Physics **9**, 416 (2007).

[77] X. Trepat, L. Deng, S. S. An, D. Navajas, D. J. Tschumperlin, W. T. Gerthoffer, J. P. Butler, and J. J. Fredberg, *Universal physical responses to stretch in the living cell,* Nature **447**, 592 (2007).

[78] O. Lieleg, J. Kayser, G. Brambilla, L. Cipelletti, and A. R. Bausch, *Slow dynamics and internal stress relaxation in bundled cytoskeletal networks.* Nature materials **10**, 236 (2011).

[79] F. Meng and E. M. Terentjev, *Fluidization of Transient Filament Networks,* Macromolecules **51**, 4660 (2018).

[80] P. Sollich, F. Lequeux, P. Hébraud, and M. E. Cates, *Rheology of Soft Glassy Materials,* Physical Review Letters **78**, 2020 (1997).

[81] N. Y. Yao, D. J. Becker, C. P. Broedersz, M. Depken, F. C. MacKintosh, M. R. Pollak, and D. a. Weitz, *Nonlinear Viscoelasticity of Actin Transiently Cross-linked with Mutant α-Actinin-4,* Journal of Molecular Biology **411**, 1062 (2011).

[82] P. Hotulainen and P. Lappalainen, *Stress fibers are generated by two distinct actin assembly mechanisms in motile cells,* The Journal of Cell Biology **173**, 383 (2006).

[83] J.-L. R. Michaud, M. Hosseini-Abardeh, K. Farah, and C. R. J. Kennedy, *Modulating α-actinin-4 dynamics in podocytes,* Cell Motility and the Cytoskeleton **66**, 166 (2009).

[84] A. J. Ehrlicher, R. Krishnan, M. Guo, C. M. Bidan, D. a. Weitz, and M. R. Pollak, *Alpha-actinin binding kinetics modulate cellular dynamics and force generation,* Proceedings of the National Academy of Sciences **112**, 201505652 (2015).

[85] K. W. Müller, R. F. Bruinsma, O. Lieleg, A. R. Bausch, W. A. Wall, and A. J. Levine, *Rheology of semiflexible bundle networks with transient linkers,* Physical Review Letters **112**, 1 (2014).

[86] K. E. Kasza, C. P. Broedersz, G. H. Koenderink, Y. C. Lin, W. Messner, E. A. Millman, F. Nakamura, T. P. Stossel, F. C. MacKintosh, and D. A. Weitz, *Actin filament length tunes elasticity of flexibly cross-linked actin networks,* Biophysical Journal **99**, 1091 (2010).

[87] B. Wagner, R. Tharmann, I. Haase, M. Fischer, and a. R. Bausch, *Cytoskeletal polymer networks: the molecular structure of cross-linkers determines macroscopic properties.* Proceedings of the National Academy of Sciences of the United States of America **103**, 13974 (2006).

[88] M. L. Gardel, F. Nakamura, J. H. Hartwig, J. C. Crocker, T. P. Stossel, and D. a. Weitz, *Prestressed F-actin networks cross-linked by hinged filamins replicate mechanical properties of cells.* Proceedings of the National Academy of Sciences of the United States of America **103**, 1762 (2006).

[89] D. Wachsstock, W. Schwarz, and T. Pollard, *Cross-linker dynamics determine the mechanical properties of actin gels,* Biophysical Journal **66**, 801 (1994).

[90] J. Xu, D. Wirtz, and T. D. Pollard, *Dynamic Cross-linking by α-Actinin Determines the Mechanical Properties of Actin Filament Networks,* Journal of Biological Chemistry **273**, 9570 (1998).

[91] R. Tharmann, M. M. a. E. Claessens, and a. R. Bausch, *Viscoelasticity of isotropically cross-linked actin networks,* Physical Review Letters **98**, 8 (2007).

[92] A. Weins, J. S. Schlondorff, F. Nakamura, B. M. Denker, J. H. Hartwig, T. P. Stossel, and M. R. Pollak, *Disease-associated mutant alpha-actinin-4 reveals a mechanism for regulating its F-actin-binding affinity.* Proceedings of the National Academy of Sciences of the United States of America **104**, 16080 (2007).

[93] F. Gittes, B. Mickey, J. Nettleton, and J. Howard, *Flexural rigidity of microtubules and actin filaments measured from thermal fluctuations in shape.* The Journal of cell biology **120**, 923 (1993).

[94] X. Trepat, G. Lenormand, and J. J. Fredberg, *Universality in cell mechanics,* Soft Matter **4**, 1750 (2008).

[95] E. Fischer-Friedrich, Y. Toyoda, C. J. Cattin, D. J. Müller, A. A. Hyman, and F. Jülicher, *Rheology of the Active Cell Cortex in Mitosis,* Biophysical Journal **111**, 589 (2016).

[96] Y. Mulla, F. C. MacKintosh, and G. H. Koenderink, *Origin of soft glassy rheology in the cytoskeleton,* Arxiv , 1 (2018).

[97] Y. Mulla and G. H. Koenderink, *Crosslinker mobility weakens transient polymer networks,* Arxiv (2018).

[98] V. W. Tang and W. M. Brieher, *alpha-Actinin-4/FSGS1 is required for Arp2/3-dependent actin assembly at the adherens junction,* Journal of Cell Biology **196**, 115 (2012).

[99] J. Alvarado, M. Sheinman, A. Sharma, F. C. MacKintosh, and G. H. Koenderink, *Molecular motors robustly drive active gels to a critically connected state,* Nature Physics **9**, 591 (2013).

[100] E. D. A. Ribeiro, N. Pinotsis, A. Ghisleni, A. Salmazo, P. V. Konarev, J. Kostan, B. Sjöblom, C. Schreiner, A. A. Polyansky, E. A. Gkougkoulia, M. R. Holt, F. L. Aachmann, B. Žagrović, E. Bordignon, K. F. Pirker, D. I. Svergun, M. Gautel, and K. Djinović-Carugo, *The structure and regulation of human muscle α-Actinin,* Cell **159**, 1447 (2014).

[101] H. C. G. de Cagny, B. E. Vos, M. Vahabi, N. A. Kurniawan, M. Doi, G. H. Koenderink, F. C. MacKintosh, and D. Bonn, *Porosity Governs Normal Stresses in Polymer Gels,* Physical Review Letters **117**, 217802 (2016).

[102] G. H. Koenderink, M. Atakhorrami, F. C. MacKintosh, and C. F. Schmidt, *High-frequency stress relaxation in semiflexible polymer solutions and networks,* Physical Review Letters **96**, 1 (2006).

[103] H. Shin, K. R. P. Drew, J. R. Bartles, G. C. L. Wong, and G. M. Grason, *Cooperativity and Frustration in Protein-Mediated Parallel Actin Bundles,* Physical Review Letters **103**, 238102 (2009).

[104] C. Heussinger, M. Bathe, and E. Frey, *Statistical Mechanics of Semiflexible Bundles of Wormlike Polymer Chains,* Physical Review Letters **99**, 048101 (2007).

[105] M. M. A. E. Claessens, C. Semmrich, L. Ramos, and A. R. Bausch, *Helical twist controls the thickness of F-actin bundles,* Proceedings of the National Academy of Sciences **105**, 8819 (2008).

[106] J. Golji, R. Collins, and M. R. K. Mofrad, *Molecular Mechanics of the α-Actinin Rod Domain: Bending, Torsional, and Extensional Behavior,* PLoS Computational Biology **5**, e1000389 (2009).

[107] D. S. Courson and R. S. Rock, *Actin cross-link assembly and disassembly mechanics for alpha-Actinin and fascin.* The Journal of biological chemistry **285**, 26350 (2010).

[108] F. Meng and E. Terentjev, *Theory of Semiflexible Filaments and Networks,* Polymers **9**, 52 (2017).

[109] I. K. Piechocka, K. A. Jansen, C. P. Broedersz, N. A. Kurniawan, F. C. MacKintosh, and G. H. Koenderink, *Multi-scale strain-stiffening of semiflexible bundle networks,* Soft Matter **12**, 2145 (2016).

[110] M. Mayer, M. Depken, J. S. Bois, F. Jülicher, and S. W. Grill, *Anisotropies in cortical tension reveal the physical basis of polarizing cortical flows,* Nature **467**, 617 (2010).

[111] N. Desprat, A. Richert, J. Simeon, and A. Asnacios, *Creep Function of a Single Living Cell,* Biophysical Journal **88**, 2224 (2005).

[112] L. Deng, X. Trepat, J. P. Butler, E. Millet, K. G. Morgan, D. A. Weitz, and J. J. Fredberg, *Fast and slow dynamics of the cytoskeleton,* Nature Materials **5**, 636 (2006).

[113] P. Kollmannsberger, C. T. Mierke, and B. Fabry, *Nonlinear viscoelasticity of adherent cells is controlled by cytoskeletal tension,* Soft Matter **7**, 3127 (2011).

[114] D. G. Thomas and D. N. Robinson, *The fifth sense: Mechanosensory regulation of alpha-actinin-4 and its relevance for cancer metastasis,* Seminars in Cell and Developmental Biology (2017), 10.1016/j.semcdb.2017.05.024.

[115] D. Feng, J. Notbohm, A. Benjamin, S. He, M. Wang, L.-H. Ang, M. Bantawa, M. Bouzid, E. Del Gado, R. Krishnan, and M. R. Pollak, *Disease-causing mutation in α-actinin-4 promotes podocyte detachment through maladaptation to periodic stretch,* Proceedings of the National Academy of Sciences **115**, 1517 (2018).

[116] S. Chakrabarti, M. Hinczewski, and D. Thirumalai, *Phenomenological and microscopic theories for catch bonds,* Journal of Structural Biology **197**, 50 (2017).

[117] S. McLaughlin and D. Murray, *Plasma membrane phosphoinositide organization by protein electrostatics.* Nature **438**, 605 (2005).

[118] F. Gittes, B. Schnurr, P. D. Olmsted, F. C. MacKintosh, and C. F. Schmidt, *Microscopic Viscoelasticity: Shear Moduli of Soft Materials Determined from Thermal Fluctuations,* Physical Review Letters **79**, 3286 (1997).

[119] D. C. Morse, *Viscoelasticity of Concentrated Isotropic Solutions of Semiflexible Polymers. 1. Model and Stress Tensor,* Macromolecules **31**, 7030 (1998).

[120] F. Gittes and F. C. MacKintosh, *Dynamic shear modulus of a semiflexible polymer network,* Physical Review E **58**, R1241 (1998).

[121] C. Heussinger, *Stress relaxation through crosslink unbinding in cytoskeletal networks,* New Journal of Physics **14**, 095029 (2012).

[122] L. Wolff, P. Fernández, and K. Kroy, *Resolving the Stiffening-Softening Paradox in Cell Mechanics,* PLoS ONE **7**, e40063 (2012).

[123] J. Plagge, A. Fischer, and C. Heussinger, *Viscoelasticity of reversibly crosslinked networks of semiflexible polymers,* Physical Review E **93**, 062502 (2016).

[124] S. Majumdar, L. C. Foucard, A. J. Levine, and M. L. Gardel, *Mechanical hysteresis in actin networks,* Soft Matter **14**, 2052 (2018).

[125] T. S. Majmudar and R. P. Behringer, *Contact force measurements and stress-induced anisotropy in granular materials,* Nature **435**, 1079 (2005).

[126] D. Mizuno, C. Tardin, C. F. Schmidt, and F. C. Mackintosh, *Nonequilibrium mechanics of active cytoskeletal networks.* Science (New York, N.Y.) **315**, 370 (2007).

[127] T. B. Liverpool, A. C. Maggs, and A. Ajdari, *Viscoelasticity of Solutions of Motile Polymers,* Physical Review Letters **86**, 4171 (2001).

[128] E. S. Dragan, *Design and applications of interpenetrating polymer network hydrogels. A review,* Chemical Engineering Journal **243**, 572 (2014).

[129] P. J. Skrzeszewska, J. Sprakel, F. A. de Wolf, R. Fokkink, M. A. Cohen Stuart, and J. van der Gucht, *Fracture and Self-Healing in a Well-Defined Self-Assembled Polymer Network,* Macromolecules **43**, 3542 (2010).

[130] K. D. Danov, P. A. Kralchevsky, B. N. Naydenov, and G. Brenn, *Interactions between particles with an undulated contact line at a fluid interface: capillary multipoles of arbitrary order.* Journal of colloid and interface science **287**, 121 (2005).

[131] F. Meng, R. H. Pritchard, and E. M. Terentjev, *Stress Relaxation, Dynamics, and Plasticity of Transient Polymer Networks,* Macromolecules **49**, 2843 (2016).

[132] H. J. Kong, E. Wong, and D. J. Mooney, *Independent Control of Rigidity and Toughness of Polymeric Hydrogels,* Macromolecules **36**, 4582 (2003).

[133] T. Gibaud, D. Frelat, and S. Manneville, *Heterogeneous yielding dynamics in a colloidal gel,* Soft Matter **6**, 3482 (2010).

[134] J. Sprakel, S. B. Lindström, T. E. Kodger, and D. A. Weitz, *Stress Enhancement in the Delayed Yielding of Colloidal Gels,* Physical Review Letters **106**, 248303 (2011).

[135] J.-F. Berret and Y. Séréro, *Evidence of Shear-Induced Fluid Fracture in Telechelic Polymer Networks,* Physical Review Letters **87**, 048303 (2001).

[136] H. Tabuteau, S. Mora, G. Porte, M. Abkarian, and C. Ligoure, *Microscopic Mechanisms of the Brittleness of Viscoelastic Fluids,* Physical Review Letters **102**, 155501 (2009).

[137] J. Sprakel, E. Spruijt, J. van der Gucht, J. T. Padding, and W. J. Briels, *Failure-mode transition in transient polymer networks with particle-based simulations,* Soft Matter **5**, 4748 (2009).

[138] A. Lucantonio, G. Noselli, X. Trepat, A. DeSimone, and M. Arroyo, *Hydraulic Fracture and Toughening of a Brittle Layer Bonded to a Hydrogel,* Physical Review Letters **115**, 188105 (2015).

[139] A. A. Griffith, *The Phenomena of Rupture and Flow in Solids,* Philosophical Transactions of the Royal Society A: Mathematical, Physical and Engineering Sciences **221**, 163 (1921).

[140] Y. Gan, *Comment on Delayed Fracture in Porous Media,* Physical Review Letters **96**, 259601 (2006).

[141] G. Nava, M. Rossi, S. Biffi, F. Sciortino, and T. Bellini, *Fluctuating Elasticity Mode in Transient Molecular Networks,* Physical Review Letters **119**, 078002 (2017).

[142] G. Bell, *Models for the specific adhesion of cells to cells,* Science **200**, 618 (1978).

[143] U. Seifert, *Rupture of Multiple Parallel Molecular Bonds under Dynamic Loading,* Physical Review Letters **84**, 2750 (2000).

[144] T. Erdmann and U. S. Schwarz, *Stability of Adhesion Clusters under Constant Force,* Physical Review Letters **92**, 108102 (2004).

[145] H. Dietz and M. Rief, *Elastic Bond Network Model for Protein Unfolding Mechanics,* Physical Review Letters **100**, 098101 (2008).

[146] D. A. Head, A. J. Levine, and F. C. MacKintosh, *Distinct regimes of elastic response and deformation modes of cross-linked cytoskeletal and semiflexible polymer networks,* Physical Review E **68**, 061907 (2003).

[147] J. Colombo, A. Widmer-Cooper, and E. Del Gado, *Microscopic Picture of Cooperative Processes in Restructuring Gel Networks,* Physical Review Letters **110**, 198301 (2013).

[148] A. Basu, Q. Wen, X. Mao, T. C. Lubensky, P. A. Janmey, and A. G. Yodh, *Nonaffine Displacements in Flexible Polymer Networks,* Macromolecules **44**, 1671 (2011).

[149] J. Liu, G. H. Koenderink, K. E. Kasza, F. C. MacKintosh, and D. A. Weitz, *Visualizing the Strain Field in Semiflexible Polymer Networks: Strain Fluctuations and Nonlinear Rheology of <math display="inline"> <mi>F</mi> </math> -Actin Gels,* Physical Review Letters **98**, 198304 (2007).

[150] Q. Wen, A. Basu, P. a. Janmey, and A. G. Yodh, *Non-affine deformations in polymer hydrogels,* Soft Matter **8**, 8039 (2012).

[151] J. Guo, Y. Wang, F. Sachs, and F. Meng, *Actin stress in cell reprogramming,* Proceedings of the National Academy of Sciences **111**, E5252 (2014).

[152] R. C. Arevalo, P. Kumar, J. S. Urbach, and D. L. Blair, *Stress Heterogeneities in Sheared Type-I Collagen Networks Revealed by Boundary Stress Microscopy,* PLOS ONE **10**, e0118021 (2015).

[153] C. Vaca, R. Shlomovitz, Y. Yang, M. T. Valentine, and A. J. Levine, *Bond breaking dynamics in semiflexible networks under load,* Soft Matter **11**, 4899 (2015).

[154] J. R. Gladden and A. Belmonte, *Motion of a Viscoelastic Micellar Fluid around a Cylinder: Flow and Fracture,* Physical Review Letters **98**, 224501 (2007).

[155] G. Foyart, C. Ligoure, S. Mora, and L. Ramos, *Rearrangement Zone around a Crack Tip in a Double Self-Assembled Transient Network,* ACS Macro Letters **5**, 1080 (2016).

[156] E. A. Novikova and C. Storm, *Contractile Fibers and Catch-Bond Clusters: a Biological Force Sensor?* Biophysical Journal **105**, 1336 (2013).

[157] D. T. Gillespie, *A general method for numerically simulating the stochastic time evolution of coupled chemical reactions,* Journal of Computational Physics **22**, 403 (1976).

[158] *See Supplemental Material at [URL will be inserted by publisher].* .

[159] C. Ligoure and S. Mora, *Fractures in complex fluids: the case of transient networks,* Rheologica Acta **52**, 91 (2013).

[160] T. Baumberger, C. Caroli, and D. Martina, *Solvent control of crack dynamics in a reversible hydrogel,* Nature Materials **5**, 552 (2006).

[161] T. Baumberger, C. Caroli, and D. Martina, *Fracture of a biopolymer gel as a viscoplastic disentanglement process,* The European Physical Journal E **21**, 81 (2006).

[162] J. Lambert, *Observationes variae in mathesin puram,* Acta Helvetica (1758).

[163] R. D. Cook, D. S. Malkus, M. E. Plesha, and R. J. Witt, *Concepts and applications of finite element analysis*, Vol. 4 (Wiley New York, 1974).

[164] S. M. V. Ward, A. Weins, M. R. Pollak, and D. A. Weitz, *Dynamic viscoelasticity of actin cross-linked with wild-type and disease-causing mutant alpha-actinin-4.* Biophysical journal **95**, 4915 (2008).

[165] E. Spruijt, J. Sprakel, M. Lemmers, M. A. C. Stuart, and J. van der Gucht, *Relaxation dynamics at different time scales in electrostatic complexes: time-salt superposition.* Physical review letters **105**, 208301 (2010).

[166] S. Mora, *The kinetic approach to fracture in transient networks,* Soft Matter **7**, 4908 (2011).

[167] G. Linga, P. Ballone, and A. Hansen, *Creep rupture of fiber bundles: A molecular dynamics investigation,* Physical Review E **92**, 022405 (2015).

[168] B. L. Mbanga, B. V. S. Iyer, V. V. Yashin, and A. C. Balazs, *Tuning the Mechanical Properties of Polymer-Grafted Nanoparticle Networks through the Use of Biomimetic Catch Bonds,* Macromolecules **49**, 1353 (2016).

[169] D. Bonn, *Delayed Fracture of an Inhomogeneous Soft Solid,* Science **280**, 265 (1998).

[170] Y. Lin and L. B. Freund, *Optimum size of a molecular bond cluster in adhesion,* Physical Review E **78**, 021909 (2008).

[171] J. Qian, J. Wang, and H. Gao, *Lifetime and Strength of Adhesive Molecular Bond Clusters between Elastic Media,* Langmuir **24**, 1262 (2008).

[172] Y. Yang and M. W. Urban, *Self-healing polymeric materials,* Chemical Society Reviews **42**, 7446 (2013).

[173] Y. Mulla, G. Oliveri, J. T. B. Overvelde, and G. H. Koenderink, *Crack Initiation in Viscoelastic Materials,* Physical Review Letters **120**, 268002 (2018).

[174] T. A. Tsunoyama, Y. Watanabe, J. Goto, K. Naito, R. S. Kasai, K. G. N. Suzuki, T. K. Fujiwara, and A. Kusumi, *Super-long single-molecule tracking reveals dynamic-anchorage-induced integrin function,* Nature Chemical Biology **14**, 497 (2018).

[175] B.-A. Truong Quang, M. Mani, O. Markova, T. Lecuit, and P.-F. Lenne, *Principles of E-Cadherin Supramolecular Organization In Vivo,* Current Biology **23**, 2197 (2013).

[176] K. E. Mueggenburg, X.-M. Lin, R. H. Goldsmith, and H. M. Jaeger, *Elastic membranes of close-packed nanoparticle arrays,* Nature Materials **6**, 656 (2007).

[177] Z. Zhang, Q. Chen, and R. H. Colby, *Dynamics of associative polymers,* Soft Matter **14**, 2961 (2018).

[178] H. Münstedt, *Rheological properties and molecular structure of polymer melts,* Soft Matter **7**, 2273 (2011).

[179] T. L. Sun, T. Kurokawa, S. Kuroda, A. B. Ihsan, T. Akasaki, K. Sato, M. A. Haque, T. Nakajima, and J. P. Gong, *Physical hydrogels composed of polyampholytes demonstrate high toughness and viscoelasticity,* Nature Materials **12**, 932 (2013).

[180] N. A. Kurniawan, B. E. Vos, A. Biebricher, G. J. Wuite, E. J. Peterman, and G. H. Koenderink, *Fibrin Networks Support Recurring Mechanical Loads by Adapting their Structure across Multiple Scales,* Biophysical Journal **111**, 1026 (2016).

[181] D. Cohen, P. Lehmann, and D. Or, *Fiber bundle model for multiscale modeling of hydromechanical triggering of shallow landslides,* Water Resources Research **45**, 1 (2009).

[182] S. A. Sell, P. S. Wolfe, K. Garg, J. M. McCool, I. A. Rodriguez, and G. L. Bowlin, *The Use of Natural Polymers in Tissue Engineering: A Focus on Electrospun Extracellular Matrix Analogues,* Polymers **2**, 522 (2010).

[183] L. Sun, Y. Kosugi, E. Kawakami, Y.-S. Piao, T. Hashimoto, and K. Oyanagi, *Magnesium concentration in the cerebrospinal fluid of mice and its response to changes in serum magnesium concentration.* Magnesium research **22**, 266 (2009).

[184] Y.-K. Lai, W.-C. Lee, and K.-D. Chen, *Vimentin serves as a phosphate sink during the apparent activation of protein kinases by okadaic acid in mammalian cells,* Journal of Cellular Biochemistry **53**, 161 (1993).

[185] I. Schwaiger, A. Kardinal, M. Schleicher, A. A. Noegel, and M. Rief, *A mechanical unfolding intermediate in an actin-crosslinking protein,* Nature Structural & Molecular Biology **11**, 81 (2004).

[186] J. M. Ferrer, H. Lee, J. Chen, B. Pelz, F. Nakamura, R. D. Kamm, and M. J. Lang, *Measuring molecular rupture forces between single actin filaments and actin-binding proteins.* Proceedings of the National Academy of Sciences of the United States of America **105**, 9221 (2008).

[187] B. a. Didonna and A. J. Levine, *Filamin cross-linked semiflexible networks: Fragility under strain,* Physical Review Letters **97**, 1 (2006).

[188] M. Bouzid, J. Colombo, L. V. Barbosa, and E. Del Gado, *Elastically driven intermittent microscopic dynamics in soft solids,* Nature Communications **8**, 15846 (2017).

[189] L. B. Case and C. M. Waterman, *Integration of actin dynamics and cell adhesion by a three-dimensional, mechanosensitive molecular clutch,* Nature Cell Biology **17**, 955 (2015).

[190] F. Meng and E. M. Terentjev, *Nonlinear elasticity of semiflexible filament networks,* Soft Matter **12**, 6749 (2016).

[191] S. Aime, L. Ramos, and L. Cipelletti, *Microscopic dynamics and failure precursors of a gel under mechanical load,* Proceedings of the National Academy of Sciences **115**, 3587 (2018).

[192] W. Liu, *Fibrin Fibers Have Extraordinary Extensibility and Elasticity,* Science **313**, 634 (2006).

[193] U. G. K. Wegst, H. Bai, E. Saiz, A. P. Tomsia, R. O. Ritchie, C. Ortiz, M. Boyce, U. G. K. Wegst, H. Bai, E. Saiz, A. P. Tomsia, and R. O. Ritchie, *Bioinspired structural materials,* Nature materials **14**, 23 (2014).

[194] J. C. Friedland, M. H. Lee, and D. Boettiger, *Mechanically Activated Integrin Switch Controls 5 1 Function,* Science **323**, 642 (2009).

[195] S. Chakrabarti, M. Hinczewski, and D. Thirumalai, *Plasticity of hydrogen bond networks regulates mechanochemistry of cell adhesion complexes.* Proceedings of the National Academy of Sciences of the United States of America **111**, 9048 (2014).

[196] C. D. Buckley, J. Tan, K. L. Anderson, D. Hanein, N. Volkmann, W. I. Weis, W. J. Nelson, and A. R. Dunn, *Cell adhesion. The minimal cadherin-catenin complex binds to actin filaments under force.* Science **346**, 1254211 (2014).

[197] T. Luo, K. Mohan, P. a. Iglesias, and D. N. Robinson, *Molecular mechanisms of cellular mechanosensing.* Nature materials **12**, 1064 (2013).

[198] B. T. Marshall, M. Long, J. W. Piper, T. Yago, R. P. McEver, and C. Zhu, *Direct observation of catch bonds involving cell-adhesion molecules.* Nature **423**, 190 (2003).

[199] U. T. Phan, T. T. Waldron, and T. A. Springer, *Remodeling of the lectin–EGF-like domain interface in P- and L- selectin increases adhesiveness and shear resistance under hydrodynamic force,* Nature Immunology (2006), 10.1109/TMI.2012.2196707.Separate.

[200] J. Kim, C.-Z. Zhang, X. Zhang, and T. A. Springer, *A mechanically stabilized receptor-ligand flex-bond important in the vasculature.* Nature **466**, 992 (2010).

[201] C. Christophis, I. Taubert, G. R. Meseck, M. Schubert, M. Grunze, A. D. Ho, and A. Rosenhahn, *Shear stress regulates adhesion and rolling of cd44+ leukemic and hematopoietic progenitor cells on hyaluronan,* Biophysical Journal **101**, 585 (2011).

[202] K. Manibog, H. Li, S. Rakshit, and S. Sivasankar, *Resolving the molecular mechanism of cadherin catch bond formation,* Nature Communications **5**, 1 (2014).

[203] V. C. Luca, B. C. Kim, C. Ge, S. Kakuda, D. Wu, M. Roein-Peikar, R. S. Haltiwanger, C. Zhu, T. Ha, and K. C. Garcia, *Notch-Jagged complex structure implicates a catch bond in tuning ligand sensitivity,* Science **355**, 1320 (2017).

[204] M. Yao, B. T. Goult, B. Klapholz, X. Hu, C. P. Toseland, Y. Guo, P. Cong, M. P. Sheetz, and J. Yan, *The mechanical response of talin,* Nature Communications **7**, 1 (2016).

[205] M. M. Sauer, R. P. Jakob, J. Eras, S. Baday, D. Eriş, G. Navarra, S. Bernèche, B. Ernst, T. Maier, and R. Glockshuber, *Catch-bond mechanism of the bacterial adhesin FimH,* Nature Communications **7**, 10738 (2016).

[206] J. M. Laakso, J. H. Lewis, H. E. Shuman, and M. E. Ostap, *Myosin I Can Act As a Molecular Force Sensor,* Science **321**, 133 (2008).

[207] B. Akiyoshi, K. K. Sarangapani, A. F. Powers, C. R. Nelson, S. L. Reichow, H. Arellano-Santoyo, T. Gonen, J. A. Ranish, C. L. Asbury, and S. Biggins, *Tension directly stabilizes reconstituted kinetochore-microtubule attachments,* Nature **468**, 576 (2010).

[208] C.-y. Lee, J. Lou, K.-k. Wen, M. McKane, S. G. Eskin, S. Ono, S. Chien, P. A. Rubenstein, C. Zhu, and L. V. McIntire, *Actin depolymerization under force is governed by lysine 113:glutamic acid 195-mediated catch-slip bonds,* Proceedings of the National Academy of Sciences **110**, 5022 (2013).

[209] R. I. Litvinov, O. Kononova, A. Zhmurov, K. A. Marx, V. Barsegov, D. Thirumalai, and J. W. Weisel, *Regulatory element in fibrin triggers tension-activated transition from catch to slip bonds,* Proceedings of the National Academy of Sciences **115**, 8575 (2018).

[210] T. Travers, H. Shao, A. Wells, and C. J. Camacho, *Modeling the assembly of the multiple domains of ??-actinin-4 and its role in actin cross-linking,* Biophysical Journal **104**, 705 (2013).

[211] D. Feng, C. DuMontier, and M. R. Pollak, *Mechanical challenges and cytoskeletal impairments in focal segmental glomerulosclerosis,* American Journal of Physiology-Renal Physiology **314**, F921 (2018).

[212] V. E. Galkin, A. Orlova, A. Salmazo, K. Djinovic-Carugo, and H. Edward Egelman, *Opening of tandem calponin homology domains regulates their affinity for F-actin,* nat struct mol biol. **17**, 614 (2010).

[213] S. A. J. van der Meulen and M. E. Leunissen, *Solid Colloids with Surface-Mobile DNA Linkers,* Journal of the American Chemical Society **135**, 15129 (2013).

[214] D. Yang, A. Ward, K. Halvorsen, and W. P. Wong, *Multiplexed single-molecule force spectroscopy using a centrifuge,* Nature Communications **7**, 11026 (2016).

[215] C. Grashoff, B. D. Hoffman, M. D. Brenner, R. Zhou, M. Parsons, M. T. Yang, M. A. McLean, S. G. Sligar, C. S. Chen, T. Ha, and M. A. Schwartz, *Measuring mechanical tension across vinculin reveals regulation of focal adhesion dynamics,* Nature **466**, 263 (2010).

[216] J. Hohlbein, T. D. Craggs, and T. Cordes, *Alternating-laser excitation: Single-molecule FRET and beyond,* Chemical Society Reviews **43**, 1156 (2014).

[217] S. W. Schneider, S. Nuschele, A. Wixforth, C. Gorzelanny, A. Alexander-Katz, R. R. Netz, and M. F. Schneider, *Shear-induced unfolding triggers adhesion of von Willebrand factor fibers,* Proceedings of the National Academy of Sciences **104**, 7899 (2007).

[218] T. Yago, J. Lou, T. Wu, J. Yang, J. J. Miner, L. Coburn, J. a. López, M. a. Cruz, J.-F. Dong, L. V. McIntire, R. P. McEver, and C. Zhu, *Platelet glycoprotein Ibα forms catch bonds with human WT vWF but not with type 2B von Willebrand disease vWF,* Journal of Clinical Investigation **118**, 3195 (2008).

[219] J. Rayes, M. J. Hollestelle, P. Legendre, I. Marx, P. G. de Groot, O. D. Christophe, P. J. Lenting, and C. V. Denis, *Mutation and ADAMTS13-dependent modulation of disease severity in a mouse model for von Willebrand disease type 2B,* Blood **115**, 4870 (2010).

[220] A. M. Rosales and K. S. Anseth, *The design of reversible hydrogels to capture extracellular matrix dynamics,* Nature Reviews Materials **1**, 15012 (2016).

[221] J.-Y. Sun, X. Zhao, W. R. K. Illeperuma, O. Chaudhuri, K. H. Oh, D. J. Mooney, J. J. Vlassak, and Z. Suo, *Highly stretchable and tough hydrogels,* Nature **489**, 133 (2012).

[222] B. Yeom, T. Sain, N. Lacevic, D. Bukharina, S.-H. Cha, A. M. Waas, E. M. Arruda, and N. A. Kotov, *Abiotic tooth enamel,* Nature **543**, 95 (2017).

[223] S. Garcia-Manyes, J. Liang, R. Szoszkiewicz, T.-L. Kuo, and J. M. Fernández, *Force-activated reactivity switch in a bimolecular chemical reaction.* Nature chemistry **1**, 236 (2009).

[224] S. B. Smith, Y. Cui, and C. Bustamante, *Overstretching B-DNA: The Elastic Response of Individual Double-Stranded and Single-Stranded DNA Molecules,* Science **271**, 795 (1996).

[225] J. Yin, P. D. Straight, S. M. McLoughlin, Z. Zhou, A. J. Lin, D. E. Golan, N. L. Kelleher, R. Kolter, and C. T. Walsh, *Genetically encoded short peptide tag for versatile protein labeling by Sfp phosphopantetheinyl transferase,* Proceedings of the National Academy of Sciences **102**, 15815 (2005).

[226] S. V. Bezrukavnikov, *Disseration* (2015).

[227] M. M. A. E. Claessens, R. Tharmann, K. Kroy, and A. R. Bausch, *Microstructure and viscoelasticity of confined semiflexible polymer networks,* Nature Physics **2**, 186 (2006).

[228] R. G. Fehon, A. I. McClatchey, and A. Bretscher, *Organizing the cell cortex: the role of ERM proteins,* Nature Reviews Molecular Cell Biology **11**, 276 (2010).

[229] S. Pautot, B. J. Frisken, and D. A. Weitz, *Production of Unilamellar Vesicles Using an Inverted Emulsion,* Langmuir **19**, 2870 (2003).

[230] C. Campillo, P. Sens, D. Köster, L.-L. Pontani, D. Lévy, P. Bassereau, P. Nassoy, and C. Sykes, *Unexpected membrane dynamics unveiled by membrane nanotube extrusion.* Biophysical journal **104**, 1248 (2013).

[231] K. Kamiya, R. Kawano, T. Osaki, K. Akiyoshi, and S. Takeuchi, *Cell-sized asymmetric lipid vesicles facilitate the investigation of asymmetric membranes,* Nature Chemistry **8**, 881 (2016).

[232] M. Angelova and D. Dimitrov, *A mechanism of liposome electroformation,* Trends in Colloid and Interface Science II **67**, 59 (1988).

[233] R. Watanabe, N. Soga, T. Yamanaka, and H. Noji, *High-throughput formation of lipid bilayer membrane arrays with an asymmetric lipid composition.* Scientific reports **4**, 7076 (2014).

[234] J. M. Crane, V. Kiessling, and L. K. Tamm, *Measuring lipid asymmetry in planar supported bilayers by fluorescence interference contrast microscopy,* Langmuir **21**, 1377 (2005).

[235] P. Kunda, N. T. Rodrigues, E. Moeendarbary, T. Liu, A. Ivetic, G. Charras, and B. Baum, *PP1-Mediated Moesin Dephosphorylation Couples Polar Relaxation to Mitotic Exit,* Current Biology **22**, 231 (2012).

[236] T. Luo, V. Srivastava, Y. Ren, and D. N. Robinson, *Mimicking the mechanical properties of the cell cortex by the self-assembly of an actin cortex in vesicles.* Applied physics letters **104**, 153701 (2014).

[237] M. Simunovic, J.-B. Manneville, H.-F. Renard, E. Evergren, K. Raghunathan, D. Bhatia, A. K. Kenworthy, G. A. Voth, J. Prost, H. T. McMahon, L. Johannes, P. Bassereau, and A. Callan-Jones, *Friction Mediates Scission of Tubular Membranes Scaffolded by BAR Proteins,* Cell **170**, 172 (2017).

SUMMARY

In your body, cells are continuously squeezing themselves through holes of different shapes and sizes. For example, immune cells migrate through the polymer matrix of your tissues, hunting for intruders. This extracellular matrix is highly non-uniform, and cellular migration requires continuous shape adaptation. Similarly, cells change their shape dramatically during cell division and differentiation. Clearly, the cell needs to be highly deformable.

The same cell has a very stressful life mechanically. For example, the cell is under continuous risk of being blown up by osmotic pressure created by the large concentration of biomolecules inside. Furthermore, large forces are exerted on cells and their surrounding tissues, for example during embryonic development or in cartilage during the movement of joints. Therefore, apart from being highly deformable, a cell also needs to be very strong.

Typically, materials are either soft or strong. For example, a pudding is readily deformable but can easily be broken by hand, whereas the opposite holds true for a brick, which has a high rupture force, but still breaks at small deformations due to its high stiffness. In contrast to these synthetic materials, a cell combines strength with deformability. *Which material design principles allow the cell to meet these seemingly contradictory demands?* Answering this question will not only increase our understanding of biology, but can also inspire the design of new synthetic materials and possibly give insight into diseases where the mechanical properties of a cell are compromised.

The mechanics of a cell are controlled by the cytoskeleton, which consists of biopolymer filaments and accessory proteins like linkers and motors. We focus on actin, the most abundant cytoskelal subunit. Actin filaments form the cell cortex, which is the main cytoskeletal player in controlling cell shape and mechanics. In the cortex, actin filaments are transiently connected by linker proteins, with a bond lifetime of a few seconds. This design principle of transient linkers causes elastic rigidity on short-timescales, whilst allowing for viscoelastic flows on timescales longer than the crosslinker unbinding timescale.

The overarching goal of this thesis is to understand how the actin cortex allows cells to be soft yet strong. To be able to directly examine the mechanical properties of actin networks, we purify and reconstitute actin together with actin binding proteins. We combine experiments with theoretical modeling to unravel the governing principles which allow for both deformability and strength of actin networks.

In chapter 2 we investigate in detail the linker dynamics through a combination of theoretical modeling and several experimental techniques. We find that stress relaxation in an actin network occurs on a faster timescale than crosslinker redistribution. We rationalize this discrepancy, using a three-state model where crosslinkers are either bound to 0, 1 or 2 filaments. In this model, stress relaxation occurs as soon as a a doubly bound crosslinker unbinds one of two filament, whereas crosslinker redistribution requires unbinding from both filaments. Surprisingly, we find that the unbinding rate of a singly bound crosslinker is more than an order of magnitude slower than when two filaments are attached. We attribute the increased unbinding rate of doubly bound crosslinkers to the stiff nature of biopolymers, which frustrates crosslinkers bound to two filaments. This chapter provides quantitative insight into the crosslinker dynamics in biopolymer networks.

In chapter 3 we examine how the linker dynamics affect the nonlinear mechanical properties of dynamically crosslinked actin networks. We find unexpectedly slow stress relaxation, similar to disordered systems close to the glass transition. We explain our experimental results using a theoretical model that accounts for the transient nature of the crosslinkers combined with the nonlinear force-extension behavior of the actin filaments. This chapter offers a microscopic mechanism for the universal glassy dynamics frequently observed in cellular mechanics.

In chapters 4 & 5 we propose a theoretical model that describes how fracturing occurs in transient networks such as the actin network. In chapter 4, we use stochastic modeling to investigate a collection of reversible bonds under load, and find a microscopic mechanism by which cracks emerge from the nonlinear local bond dynamics. We provide and numerically verify analytical equations for the dependence of the critical crack length on the bond kinetics and applied stress. In chapter 5, we extend the stochastic model to consider the effect of bond mobility after unbinding on the strength of a transient network. We find that bond mobility weakens transient networks. This is remarkable as bond mobility is common in biological transient networks such as the actin cortex, and in systems responsible for cellular adhesion. We speculate that cells trade fracture strength for the modularity and tight dynamic control offered by mobile linkers. These chapters reveal governing principles of the fracturing of transient networks such as the actin cortex.

In chapter 6 we study the effect of catch bonding on network strength. Catch bonds are proteins whose bond lifetime increases when moderate forces are applied via exposure of hidden binding sites. After full exposure at high force, catch bonds behave like normal (slip) bonds whose bond lifetime monotonically decreases with force. Using the stochastic model developed in chapter 4 & 5, we show that catch bonds provide vastly more long-lived networks than slip bonds. Surprisingly, we find that catch bond networks are stronger than slip bond networks even when the individual bonds are weaker. We verify our conclusion experimentally by combining single molecule and network experiments on actin crosslinked by either wild type α-actinin 4 (which forms catch bonds) or its slip bond counterpart, a mutant with a single point mutation referred to as K255E. We attribute the increased strength of catch bond networks to a self-assembly mechanism against force inhomogeneity. This chapter reveals the importance of catch bonds in preventing fracturing in highly deformable transient networks such as the actin cortex.

The work in this thesis gives novel insight into how cells manage to be highly deformable yet strong. The design principle of transient networks allows for substantial deformability over timescales longer than the typical crosslinker unbinding time. However, due to fluctuations in local linker density, transient networks are also prone to crack initiation and subsequent fracturing. Importantly, catch bond linkers self-assemble against force inhomogeneity, and thereby prevent crack initiation despite their faster unbinding kinetics compared to slip bond linkers. These catch bond linkers therefore simultaneously increase both deformability and strength of transient networks. We have revealed this principle for actin networks, but expect the mechanism to occur for any transient network connected by catch bond linkers. Our finding of increased strength and deformability therefore suggests a novel evolutionary driving force behind catch bonds, and indeed we have found many biological examples of catch bonds connecting transient networks.

Strikingly, our work on the catch bond crosslinker and the constitutively active mutant is interesting from a biomedical perspective as well. The catch bond we considered, α-actinin 4, is the actin crosslinker in podocytes. These cells are under continuous pressure as they filter the blood in our kidneys. Whereas the catch bond crosslinker is the wild type version, the constitutively active mutant is known to cause the kidney failure disease focal segmental glomerulosclerosis 1 (FSGS1). Strikingly, FSGS1 cells expressing the constitutively active mutant linker are significantly more brittle than cells expressing the wild type catch bond linker. It will be interesting to study the importance of catch bonding in preventing failure of cells and tissues in the context of FSGS1 and other diseases.

Lastly, our work can provide inspiration for new design strategies of synthetic materials. Transient networks are not only common in biology, but are also often used to create synthetic viscoelastic materials such as colloidal gels and polyelectrolytes in food and cosmetics. These materials suffer from limited deformability due to crack initiation. For future work, it would be interesting to create synthetic analogues of catch bonds to create bio-inspired materials which are highly deformable yet durable under stress. Such materials would be ideal for applications in regenerative medicine.

SAMENVATTING

In je lichaam persen cellen zichzelf continu door gaten van verschillende vormen en grootten. Immuuncellen migreren bijvoorbeeld door de polymeermatrix van je bindweefsel, op jacht naar indringers. Deze extracellulaire matrix is sterk heterogeen en cellulaire migratie vereist voortdurende vormveranderingen. De cel vervormt ook drastisch tijdens celdeling en -differentiatie. Een cel dient overduidelijk vervormbaar te zijn.

Tegelijkertijd heeft een cel mechanisch gezien een stressvol leven. De cel loopt bijvoorbeeld permanent het risico om opgeblazen te worden door de osmotische druk die het gevolg is van de grote concentratie biomoleculen aan de binnenkant van de cel. Verder worden er grote krachten op cellen en hun omringend weefsel uitgeoefend, bijvoorbeeld tijdens de embryonale ontwikkeling of tijdens beweging van je spieren en van kraakbeen in je gewrichten. Daarom moet een cel, behalve vervormbaar, ook sterk zijn.

Materialen zijn normaliter vervormbaar of sterk. Pudding is bijvoorbeeld zo te vervormen, maar je kan het makkelijk met je handen breken en is dus niet sterk. Het tegenovergestelde is waar voor een baksteen, die veel kracht kan weerstaan, maar al bij kleine vervormingen breekt. In tegenstelling tot deze niet-biologische materialen, is een cel zowel vervormbaar als sterk. *Welke materiaalontwerpprincipes stellen een cel in staat om deze schijnbaar tegengestelde eisen te vervullen?* Het beantwoorden van deze vraag zal ons begrip van biologie doen toenemen, bijvoorbeeld van ziektebeelden waarbij de mechanische eigenschappen van de cel zijn aangetast. Verder kunnen de biologische materiaalontwerpprincipes inspiratie geven voor het ontwerp van nieuwe synthetische materialen, zodat we sterke, zachte materialen kunnen maken.

De mechanische eigenschappen van een cel worden bepaald door het cytoskelet, dat bestaat uit biopolymeren en bijbehorende eiwitten, zoals linkers die polymeren verbinden en moleculaire motoren. Wij richten ons op aktine, de meest voorkomende deeleenheid van het cytoskelet. Aktine filamenten vormen de celschors. Deze celschors speelt een belangrijke rol in het dirigeren van celvorm en -mechanica. In de celschors zijn aktinefilamenten gebonden door linkereiwitten, die doorgaans slechts een paar seconden gebonden zijn, waarna ze loslaten en ergens anders binden. Dit ontwerpprincipe van 'vergankelijke linkers' zorgt voor stijfheid op korte tijdschalen, terwijl het viscoelastisch stromen toelaat op tijdschalen langer dan de bindingstijd van de linkers.

Het overkoepelende doel van deze dissertatie is om te begrijpen hoe de aktineschors ervoor zorgt dat cellen zacht doch sterk kunnen zijn. Om de mechanische eigenschappen van aktinenetwerken direct te kunnen bestuderen, zuiveren we aktine samen met aktine-bindende eiwitten op en reconstrueren we de netwerken. We combineren experimenten met theoretisch modeleren, om de leidende principes te ontrafelen die aktine netwerken in staat stellen zowel vervormbaar als sterk te zijn.

In hoofdstuk 2 bekijken we de linkerdynamica in detail door een combinatie van theoretisch modeleren en verschillende experimentele technieken. We ontdekken dat de stressrelaxatie in aktine netwerken op snellere tijdschalen optreedt dan de linker dynamica. We onthullen de oorzaak van deze discrepantie middels een drie-staten model, waarbij linkers gebonden zijn aan 0, 1 of 2 filamenten. In dit model treedt stressrelaxatie op zodra een dubbelgebonden linker een van de twee filamenten loslaat, terwijl linkerredistributie pas optreedt als beide filamenten zijn losgelaten. Verrassend genoeg vinden we dat de snelheid waarmee een enkel gebonden linker een filament loslaat, meer dan tien keer langzamer is dan wanneer twee filamenten gebonden zijn. We schrijven het versnelde loslaten van een dubbelgebonden linker toe aan de stijfheid van biopolymeren. Deze stijfheid belemmert linkers die gebonden zijn aan twee filamenten, waardoor er spanning ontstaat en linkers sneller loslaten. Dit hoofdstuk geeft kwantitatief inzicht over de linkerdynamica in biopolymeernetwerken.

In hoofdstuk 3 onderzoeken we hoe de linkerdynamica de niet-lineare mechanische eigenschappen van dynamisch verbonden aktine netwerken beinvloedt. We vinden onverwacht langzame stressrelaxatie, die vergelijkbaar is met ongeordende systemen dichtbij de glastransitie. We verklaren onze experimentele waarnemingen middels een theoretisch model dat rekening houdt met de vergankelijke aard van de linkers in combinatie met het niet-lineaire kracht-uitrek gedrag van aktine filamenten. Dit hoofdstuk biedt microscopisch mechanisme dat kan verklaren waarom celmechanica de universele dynamica van glazige systemen volgt.

In hoofdstukken 4 & 5 stellen we een theoretisch model voor dat beschrijft hoe vergankelijke netwerken, waaronder aktine netwerken, breken. In hoofdstuk 4 maken we gebruik van een stochastisch model om een verzameling van reversibele bindingen onder druk te bestuderen. We ontdekken een microscopisch mechanisme waarmee scheuren oprijzen uit de niet-lineare, plaatselijke bonddynamica. We stellen analytische vergelijkingen voor die we numeriek verifieren, en beschrijven hoe de kritische kraaklengte afhangt van de bonddynamica en de uitgeoefende kracht. In hoofdstuk 5 breiden we dit stochastische model uit en beschouwen we het effect van bondmobiliteit na ontbinden op de kracht van vergankelijke netwerken. We ontdekken dat mobiliteit vergankelijke netwerken verzwakt. Dit is merkwaardig omdat bondmobiliteit vaak voorkomt in biologische, vergankelijke netwerken zoals de aktine schors en in systemen die verantwoordelijk zijn voor celadhesie. We speculeren dat cellen een compromis maken tussen netwerkkracht en de modulariteit en nauwe dynamische controle die mobiele linkers biedt. Deze hoofdstukken onthullen de leidende principes achter de breekbaarheid van vergankelijke netwerken zoals de aktineschors.

In hoofdstuk 6 bestuderen we het effect van ’vangstbindingen’ op netwerkkracht. ’Vangstbindingen’ zijn bindingen tussen eiwitten waarbij de bindingsduur toeneemt als er een gematigde kracht op uitgeoefend wordt. De bindingsduur neemt toe door middel van verborgen bindingsdomeinen die worden blootgesteld bij kracht. Na volledige blootlegging bij hoge kracht, gedragen vangstbindingen zich zoals normale (slip)bindingen waarbij de bindingsduur monotoon afneemt met kracht. Middels het stochastische model ontwikkeld in hoofdstuk 4 & 5 laten we zien hoe vangstbindingen netwerken opleveren die veel duurzamer zijn dan netwerken verbonden door slipbindingen. Verrassend genoeg ontdekken we dat vangstbindingsnetwerken sterker zijn dan slipbindingsnetwerken zelfs waneer de individuele bindingen zwakker zijn. We verifieren onze conclusies experimenteel door een combinatie van experimenten op netwerk- en enkel molecuulniveau.

In deze experimenten vergelijken we aktine gebonden door veldstam α-actinin 4 (die vangstbindingen vormt) of zijn slipbinding tegenhanger, een mutant met een enkele K255E puntmutatie. We schrijven de verbeterde kracht van vangstbindingsnetwerken toe aan een zelf-assemblage mechanisme tegen krachtinhomogeniteit. Dit hoofdstuk toont het belang van vangstbindingen aan in het voorkomen van scheuren in vergankelijke netwerken zoals de aktineschors.

Deze dissertatie geeft nieuwe inzichten over hoe de cel het voor elkaar krijgt sterk en toch vervormbaar te zijn. Het ontwerpprincipe van vergankelijke netwerken staat substantiele vervorming toe op tijdschalen langer dan de typische bindingsduur van linkers. Door fluctuaties in de lokale linkerdichtheid zijn vergankelijke netwerken echter ook gevoelig voor het ontstaan van scheuren waarna het materiaal breekt. Vangstbindingen zelf-assembleren tegen krachtinhomogeniteit en voorkomen daardoor het ontstaan van scheuren. Zelfs als vangstbindingen sneller loslaten dan slipbindingen, zorgen ze voor sterkere netwerken. Deze vangstbindingen vergroten daarmee tegelijkertijd de vervormbaarheid en kracht van vergankelijke netwerken. Wij hebben dit principe ontdekt in aktine netwerken, maar verwachten dat het mechanisme optreedt in elk vergankelijke netwerk dat verbonden is door vangstbindingen. Onze ontdekking van toegenomen kracht en vervormbaarheid suggereert een evolutionaire drijvende kracht achter vangstbindingen. Deze evolutionaire drijvende kracht verklaart mogelijk waarom vangstbindigen wijdverspreid zijn in vergankelijke netwerken in de biologie.

Ons werk is ook relevant vanuit een biomedische invalshoek. De vangstbinding die we bestudeerd hebben, α-actinin 4, is een aktine linker in podocyten. Deze cellen staan onder permanente druk door het bloed dat ze filteren in onze nieren. Waar de vangstbindingen te vinden zijn in gezonde nieren, is bekend dat de K255E mutatie zorgt voor nierfalen (Focale Segmentale Glomerulosclerose 1, afgekort met FSGS1). Opvallend is dat FSGS1 cellen die de slipbindingsmutant tot expressie brengen significant brozer zijn dan gezonden cellen met de vangstbindingen. Het zou interessant zijn om het belang van vangstbindingen te onderzoeken in het voorkomen van breken van cellen en weefsel in de context van FSGS1 en andere ziektes.

Tenslotte biedt deze dissertatie een inspiratiebron voor nieuwe ontwerpprincipes van synthetische materialen. Vergankelijke netwerken zijn niet alleen veelvoorkomend in de biologie, maar worden ook vaak gebruikt om synthetische viscoelastische materialen te maken zoals kolloidale gelen en polyelectrolyten in voedsel en cosmetica. Het nut van deze materialen is echter beperkt doordat er na geringe vervormbaarheid al scheuren ontstaan. In de toekomst zou het interessant zijn om synthetische analogen van vangstbindingen te gebruiken om materialen te maken die, geinspireerd door de biologie, sterk vervormbaar en toch sterk zijn. Zulke materialen zouden ideaal zijn voor toepassingen in bijvoorbeeld regeneratieve geneeskunde.

ABOUT THE AUTHOR

Yuval Mulla was born in Kfar Saba, Israel, in 1990. During his high school, Yuval enjoyed the challenges presented in his Physics courses, but was more intrigued by the questions raised during Biology. To combine both aspects, he started a bachelor studies at the University of Wageningen in Molecular Life Sciences in 2008, and wrote a thesis in the laboratory of Physical Chemistry and Soft Matter led by (now emeritus) Prof. Martien Cohen Stuart. Yuval enjoyed how macroscopic structure and functionality could arise in soft matter thanks to, rather than despite of, weak interactions and thermal noise. Wanting to apply this knowledge in a more biological context, he continued studying the Master Molecular Life Sciences in the track Physical Biology, in 2011 at Wageningen University. He wrote a thesis in the laboratory of Biophysics led by Prof. Dr. Herbert van Amerongen. During his Master, he also performed an internship in the laboratory of Biomineralization led by Prof. Steve Weiner at the Weizmann Institute, studying the mechanics of hard biological matter - namely bones. Afterwards, Yuval found a PhD-project where he could strengthen his knowledge on biology, mechanics and soft matter in the Biological Soft Matter lab led by Prof. Gijsje Koenderink at AMOLF. This project has led to the PhD-thesis you are reading now.

Recently, Yuval joined the Bollenbach lab at the University of Cologne, to use experimental evolution to study how bacteria become antibiotic resistant. He plans to develop high-throughput robotized techniques to study evolution of *E. Coli* under well-controlled environmental dynamics. In essence, he continues studying the macroscopic dynamics of microscopically noisy, biological systems.

PUBLICATIONS COVERED IN THIS THESIS

1. F. Burla*, **Y. Mulla***, B.E. Vos, A. Aufderhorst-Roberts, G.H. Koenderink, *Biopolymers: the mechanical scaffolds of Living Matter*, Nat. Rev. Phys., under review. (parts of chapter 1)
2. **Y. Mulla***, A. Aufderhorst-Roberts*, and G.H. Koenderink. Shaping up synthetic cells. Phys. Biol., 2018. (parts of chapter 1)
3. **Y. Mulla**, H. Wieringa, C. Alkemade, P.R. Ten Wolde, G.H. Koenderink, *Cooperative binding of biopolymer crosslinkers*, Soft Matter, under review. (chapter 2)
4. **Y. Mulla**, F.C. Mackintosh, G.H. Koenderink, *Origin of soft glassy rheology in biopolymer networks*, Phys. Rev. Lett., under review. (chapter 3)
5. **Y. Mulla**, G. Oliveri, J.T.B. Overvelde, G.H. Koenderink, *Crack initiation in Viscoelastic Materials*, Phys. Rev. Lett., 2018. (chapter 4)
6. **Y. Mulla**, G.H. Koenderink, *Crosslinker mobility weakens transient polymer networks*, Phys. Rev. E., accepted. (chapter 5)
7. **Y. Mulla**, M. J. Avellaneda, S. J. Tans, G.H. Koenderink, *Catch bonds form dynamic yet strong materials*, Manuscript in preparation. (chapter 7)

*Shared first author

Other publication(s) by the same author

8. D. Perrier, A. Vahid, V. Kathavi, L. Stam, Lea Rems, **Y. Mulla**, G.H. Koenderink, Pouyan Boukany, M. Kreutzer, *Unravelling the response of the actin cortex to electric pulses in vesicles*, Sci. Rep., under review.

ACKNOWLEDGEMENTS

I greatly enjoyed my PhD and I am proud to now be an alumnus of Gijsjes lab.The way you lead your lab and supervise students is extraordinary. Despite your continuously crammed agenda ("yeah, the last months were a bit hectic"), you were always ready and eager to discuss ideas, give feedback and share enthusiasm. Especially during my final year you have played an invaluable role - I'll never forget the amount of time, attention and care you have dedicated to the lab, to the project and to me. I hope you are aware of how much this has meant to me and how much it means to everyone in the lab. Thank you.

I believe AMOLF is a fantastic place and this institute would not have been the same without Dick van Gameren. You might not know him, and neither do I, but he's the guy who designed the building that hosts our beloved institute. This building excels at providing unscheduled contact via its open structure, koffieruimte, kantine and receptiehuisje. Indirectly, Dick van Gameren probably played an important role in initiating collaborations. For similar reasons, I want to thank all past and current members of the PV. This institute has got some really cool traditions and most of them are thanks to you. Thanks for organising the Christmas parties, Ice skating events, easter egg hunts, outings and what-not. Apart from the festive traditions, I also hope we stick to some of the village-vibe traditions such as the presentielijst, open day, donderdagmiddagmededelingen and institute-wide koffiepauze.

All these AMOLF traditions enable the right spirit for science, but do not yet provide the means. Throughout my PhD, I felt blessed with the excellent support. This fancy microscope presented in the outlook chapter would not have been here without Jan Bonne, Brahim, Henk-Jan, Marko and the Marco's. you guys have put a lot of effort in it, and I'm sure it's gonna produce great science. On top of that, I want to thank Jan Bonne and Marko for the help on the I-don't-know-how-many times you've rescued my microscopy experiments with on the fly troubleshooting. Furthermore, I want to thank everybody from the werkplaats, inkoop, reception, ICT department, Niels, Hinco and the design department, especially Ricardo for designing the awesome thesis cover. I also want to thank the communications department, in particular for the organisation of the yearly open day. Even without the outreach, this event is already worthwhile for the amount of fun and social interactions it provides to us.

Next up, I want to thank everyone with whom I've shared some time in the biological soft matter group: Florian, Adeline, Nicholas, Jeanette, Feng, Corianne, Maga, Stef, Aditya (let's pretend you were a group member), Viktoria, Galja, Bart, Cristina, Anders, Tatjana, Karin, Stijn, Mick, Ilva, Agata, Celine, Federica, Lennard, Lucia, Marjolein, Jeffrey, Tjado, Shayla, Cees, Liza, Sven, Jasmijn, Faisal, Philippine, Faranaaz, Rouqaya, Ruben, Alexandra, Merel, George, Sophie and Rosalie. My apologies if I forgot someone, but in my defense, I copied this list from Bart's thesis. During my PhD, I enjoyed supervising some exceptionally motivated students: George, Philippine, Sven and Celine

(I nearly forgot you actually started out as an intern). Viktoria and Agata, even though we drifted off to different research themes a bit, it was fun to be together in this minicel project. Viktoria, I am happy that we still see eachother in Cologne. Agata, I hope we will also stay in touch, as long as there is no swimming in Marseille involved. Lennard, Lucia and Cees, all the best with continuing on the pathway towards synthetic life - regardless of whether you'll get there, I'm sure you'll run into interesting things along the way. Anders, thanks for the endless social events you've organized (Burn's nights, brunches etc.). Federica, thanks for all your jokes, according to the fortune teller you are a really funny person. Florian, I think I cried when you left academia, but it was inspiring to see you build Kandi and I hope you'll find as much fulfillment at the eScience center. Stef, I am happy to have met you during the tail of your PhD. Aditya, you're the true social scientist, blurring lines between collaboration and friendship. In any case you're a lot better in academics than on skis.

It is generally known that 0.16 is the most fun office at AMOLF, thanks to Bart, Lennard, Marjolein, Jeff and Jacopo. Marjolein, you've always been the goof-factor that made everyone laugh. Also it was amazing to see you shrink so much in such a short time - you might really have super powers. Lennard and Jeff, thanks for bringing in some fresh enthuisiasm into the office to distract everyone else from writing the thesis. Jacopo, it was fun to see you pick up any random object and make proper music out of it. Bart, my non-biological twin brother, I will miss seeing the upper half of your face several hours per day more than I care to admit. Oh, and thanks for the fruit basket.

One cool thing about AMOLF is the collaborative atmosphere between groups. Mario, Vanda, Sander, Giorgio, Bas, Harmen and Pieter Rein, it was a joy to work together on the various projects. There is also a large range of people with whom I did not formallly collaborate, but the numerous informal scientific and non-scientific discussions have definitely enriched my PhD, thanks Eline, Steffen, Florian, Marco, Ramon, Konrad, and Melle. Johannes, the conservative voice of AMOLF. Noreen, with your remarkable fondness of Phillips. Joris, the most well-mannered person I have ever met. Plus, you are an impressive 'burler'. Martijn, I will never forget your re-enactment of Pieter Rein. Olga, I wish you many hours of 'bonen'. Adithya, keep up the flip-flops. Tornado Matthijs, please deflate the skippy ball before disaster strikes.

Gijsje has taught me the value and joy of scientific collaborations. In this spirit I want to the team Eindhoven (Nicholas Tito and Wouter Ellenbroek), 'team' Houston (Fred Mackintosh) and team Munich (Chase, Mareike and David). Also, Mareike, enjoy AMOLF! Although Septin and I never really got along too well, I did enjoy the Septin collaborations with Manos, Aurelie, Alexandre Beber, Stephanie Mangenot and Patricia Bassereau.

There's also a range of people outside of academics whom I want to thank for making me keep up spirits. First of all of course my familiy. It is safe to say that without my parents I would not be here. Second, everyone who feels affiliated to any of the following groups of friends: Bonzai, Azotobacter and homeboys. Thirdly, I want to thank Hannah for the family-in-law and for everything during and since Dudzele.

Lastly, I want to thank you, the reader, for reading my entire thesis down to the very last sentence.